University of Reading

The Impact of Lipidation on the Self-Assembly and Bioactivity of the Gastrointestinal Peptide Hormone PYY_{3-36}

A Thesis Submitted for the Degree of Doctor of Philosophy

Department of Chemistry

Jessica Hutchinson

March 2019

Declaration

I can confirm that this is my own work and the use of material from other sources has been properly and fully acknowledged.

Jessica Hutchinson

Acknowledgements

To begin with I would like to hugely thank Professor Ian Hamley for giving me the opportunity to study for this PhD. He has been a great supervisor throughout, providing guidance, and allowing me to travel all over the world, as well as being extremely efficient at responding to any query I had. It truly has been the best thing I've done in my life, and thanks to Ian I have gained invaluable skills from it as well as studying for the degree. I would also like to thank Dr Valeria Castelletto for having the time and patience to help me the entire time, and for all of the bigger picture conversations we had about the future.

Thank you to Dr Anna-Karin Lundback, Dr Ana Santos, Dr Shahid Uddin, and everyone at MedImmune for their help and support, in particular Anna-Karin who is one of the nicest people I have ever met. I would also like to thank Nick Spencer for helping with X-ray techniques; nothing was ever too much trouble for him. Thank you to all of the collaborators I have worked with over the past three years.

I would also like to thank Sam Burholt for his support, especially when I moved down to Reading from up north; he really welcomed me and made my time at Reading much less lonely. A massive thank you to Charlotte Edwards-Gayle, she has made my PhD extremely enjoyable and has become a friend for life. Thank you to my boyfriend, Ste for his continued support and encouragement over the past few years. Finally, thank you to my parents and grandparents for always supporting me no matter what; I really wouldn't be where I am today without them.

Abstract

Peptide YY (PYY) is a gut hormone belonging to the pancreatic polypeptide (PP) family, and is released by the L-cells of the gastrointestinal tract following food intake. There are two main endogenous forms: PYY_{1-36} and PYY_{3-36}, with the latter having a high selectivity for the Y2-receptor which is associated with reduced food intake. The use of PYY_{3-36} as an anti-obesity and type II diabetes drug is therefore of great interest.

Peptide hormones have short circulating half-lives; therefore it is of high importance to develop a strategy to overcome this for the development of peptide drugs. The use of lipidation is a promising method as it allows the peptide to bind to serum albumin, increasing molecular weight and thus reducing renal filtration.

In this thesis the impact of lipidation, and the position of lipidation on the self-assembly of PYY_{3-36} and various truncated derivatives are investigated. A wide range of physical characterisation techniques are employed to understand self-assembly and aggregation. Some cytotocompatibility studies using MTT assays on human colorectal cancer cells are also carried out in order to understand cytotoxicity.

It was apparent throughout the project that lipidation significantly impacted the self-assembly, by helping to drive aggregation as a result of the increased amphiphilicity caused by the addition of the lipid chain, which in this case was a palmitoyl chain. The full PYY_{3-36} peptide and the lipidated derivatives had predominantly α-helical secondary structures. They differed largely when they aggregated however, with the native peptide being mostly monomers with some nanotapes, and the lipidated peptides having micelle and fibril conformations depending on pH. In addition to this the lipidated peptides formed gels under specific conditions whereas the native peptide did not.

Investigations into the truncated peptide fragments further enhanced the impact of lipidation, where the lipidated fragments had micelle and fibril conformation, whereas the native fragments did not aggregate at all. Cytocompatibility studies found the lipidated peptides to be cytotoxic at concentrations above the cmc, suggesting that aggregation causes the peptides to become cytotoxic.

Contents

Chapter 1 – Introduction

1.1 Peptides

Peptides are small assemblies of amino acid monomers linked by covalent peptide bonds. There are 20 natural amino acids which make up the building blocks for various peptides and proteins. Most amino acids with the exception of proline consist of an alpha carbon atom to which a hydrogen atom, an amino group, a carboxyl group, and a side chain R group are attached.[1] The only variable group on an amino acid is the R group, and it is this that is responsible for the different properties of the various amino acids.

The peptide bond is formed by the linking of two amino acids, with the elimination of water via a condensation reaction between the neighbouring $–NH_2$ and –COOH groups, resulting in a dipeptide (figure 1.1).[1]

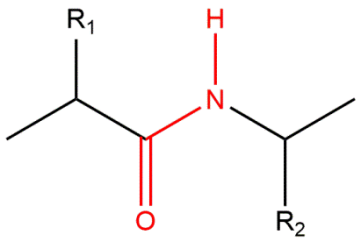

Figure 1.1. Structure of a peptide bond.

The peptide bond has a double bond character due to delocalisation of the lone pair of electrons on the nitrogen atom, which means that no rotation is possible around the bond. This allows the peptide to have either a cis or trans conformation. The

delocalisation of electrons results in the peptide bond having resonance, meaning it is relatively unreactive under physiological conditions which is important in biological systems (figure 1.2).[2]

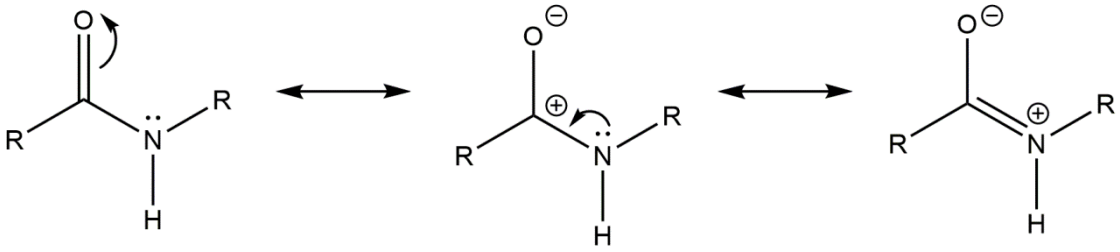

Figure 1.2. Resonance structures of a peptide bond.

Multiple amino acid residues bound by peptide bonds are known as polypeptides, and these are what make up the backbone structures of proteins. Proteins are classified as having around 50 or more amino acid monomers in the polypeptide chain. There are 20 different types of amino acid that can be combined to form a protein, and it is the sequence of amino acids that determines the structure and function of a protein.

There are four categories of peptide structure; primary, secondary, tertiary and quaternary. The primary structure of a peptide refers to the amino acid sequence from the N-terminus to the C-terminus. The secondary structure is when the peptide is held into a structure, such as an alpha helix or a beta sheet. The secondary structures are held together by hydrogen bonds. Tertiary structure is the final three dimensional shape, and it is held together by interactions between the R groups. These interactions can be ionic, hydrogen bonding, van der Waals forces and also sulphur bridges.

1.1.2 Peptide self-assembly

Supramolecular self-assembly is the ability of molecules to spontaneously form ordered nanostructures via non-covalent interactions such as van der Waals, electrostatic, hydrogen bonding, and stacking interactions.[3] Self-assembly is important in many biological systems such as the self-assembly of lipid membranes, the DNA double helix, and folded proteins.[3-4] Peptides can self-assemble into a wide range of different nanostructures depending on the hydrophile/lipophile balance of molecules, the number and sequence of amino acids, as well as the interactions between the peptide units.[5] Hydrogen bonding between backbones of peptides plays an important role in self-assembly and can cause the peptide monomers to pack longitudinally into β-sheets, a common secondary structure arising from peptide self-assembly, and they either have anti-parallel or parallel conformations (Figure 1.3). Peptides with a β-sheet secondary structure often form fibril structures that can subsequently cross-link to form hydrogels, allowing them to act as slow releasing systems in drug delivery.[6] On the other hand they can also be detrimental by forming amyloid fibrils, heavily associated with neurodegenerative diseases, such as Alzheimer's disease. Another common secondary structure formed by self-assembly is the α-helix (Figure 1.4), characterised by a single spiral chain of amino acids stabilised by hydrogen bonding between N-H and C=0 groups. An example of an α-helical compound is the iron and oxygen binding protein, myoglobin, found in most mammals.[7] Peptides that typically form α-helices exhibit amino acids of similar properties every 3-4 residues, giving rise to the structural repeat of 3.6 residues per α-helical turn.

As a result of self-assembly being so important in nature, the use of self-assembling peptides for use in therapeutics has gained increasing attention. This is due to them being versatile molecules with tuneable functionality, and high biocompatibility and biodegradability.[3] A polypeptide for example can consist of a targeting sequence, a self-assembly domain, and a biologically active peptide.[8] This is extremely attractive from an industrial point of view as it prevents the need for complex synthetic chemical reactions. Consequently, peptides provide a unique platform for the design of nanomaterials with controllable structural features.

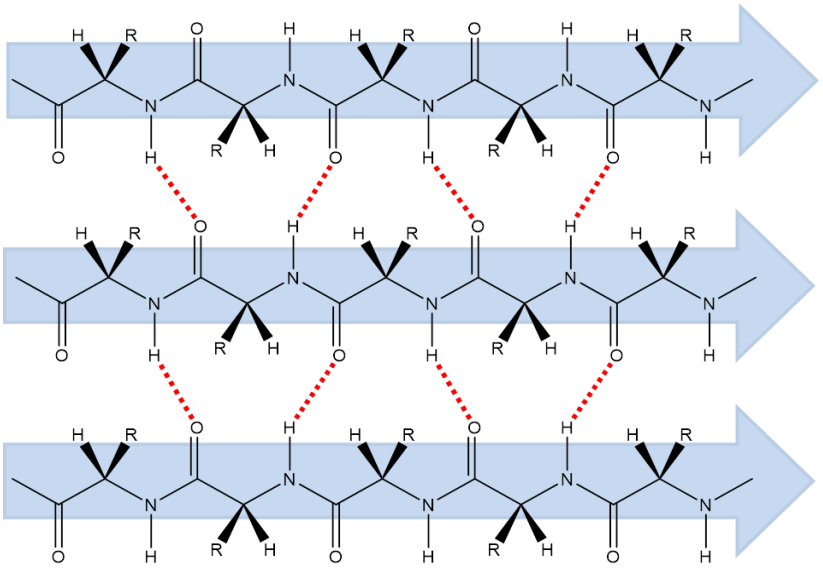

Parallel β-sheet

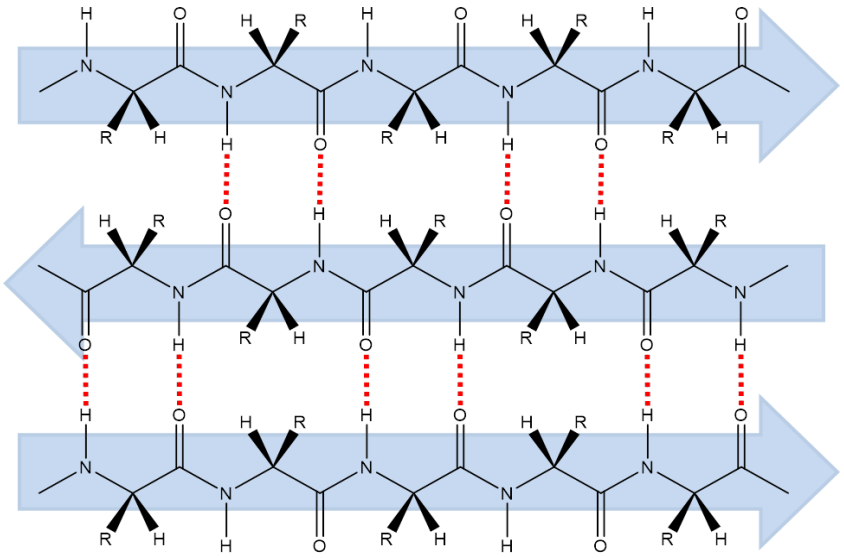

Antiparallel β-sheet

Figure 1.3. Parallel and anti-parallel β-sheet orientations.

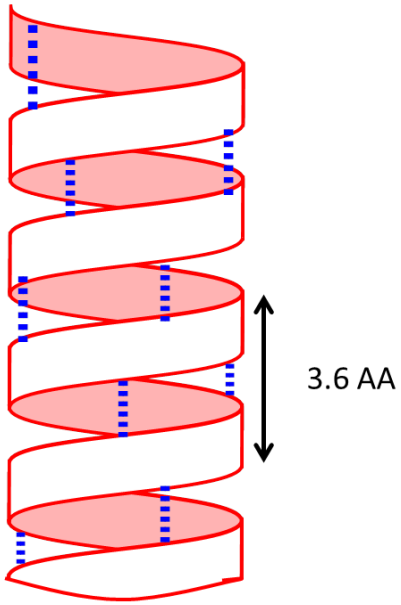

Figure 1.4. Illustration of an α-helix showing hydrogen bonding between C=O and N-H groups (dashed lines). Each helical turn contains 3.6 amino acid residues.

Environmental factors such as pH and temperature play a key role in peptide self-assembly. A simple change of environment allows for fine tuning of peptide self-assembly for a variety of applications. A study by Stevens et al discovered that is was possible to control the assembly of coiled-coil based gold nanoparticles using a leucine zipper-like peptide, with changes in pH and temperature. It was found that the nanoparticles aggregated when the pH was lowered to 4.5, and disassembly occurred as the temperature was increased due to thermal unfolding of the α-helices.[9] In another study by Thanh et al. the aggregation of an endogenous opioid peptide neurotransmitter derivative, with the sequence YVIFL, as a function of pH was investigated. Aggregates were obtained throughout the pH range 2-11, but with different morphologies ranging from amorphous structures at low pH to fibrils at increased pH.[10] The prevailing driving forces behind aggregation are salt bridges, hydrogen-bonds, hydrophobicity, and net

charge contributions from ionizable side chains, with charged residues causing interruptions in contiguous stretches of hydrophobic sequences, as well as causing electrostatic repulsion between units.[10] With this is mind, the propensity of the YVIFL peptide to aggregate into amorphous structures at low pH is more clearly understood.

1.2 Peptide amphiphiles

Most self-assembling molecules are amphiphilic, meaning they have both hydrophobic and hydrophilic character. Peptide amphiphiles are a class of molecules comprised of either hydrophobic and hydrophilic peptide sequences, or a hydrophilic peptide with an attached hydrophobic group, which is usually an alkyl chain. The structure of a peptide amphiphiles has four key domains (Figure 1.5). Firstly there is a hydrophobic section, typically an alkyl chain. Secondly there is the peptide sequence which forms intermolecular hydrogen bonding. Thirdly there is a section of charged amino acid residues to enhance the solubility of the peptide in water. The final structural feature allows the peptide to interact with biomolecules, cells, or proteins, and this is often through epitopes (part of antigens recognised by the immune system).[6]

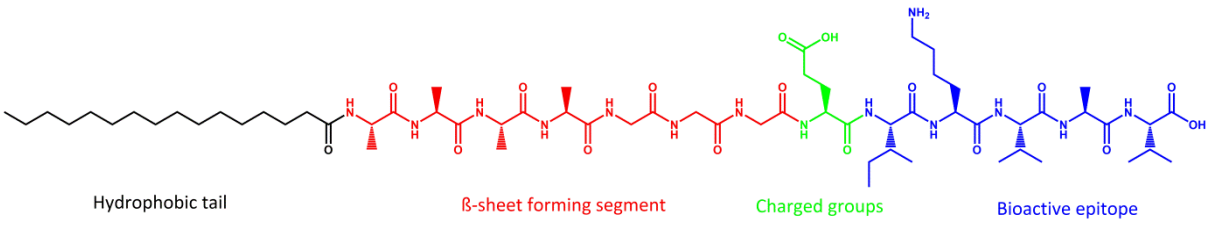

Figure 1.5. Structure of a peptide amphiphile showing the four different domains: a hydrophobic domain, a β-sheet section, a charged group, and a bioactive head group.[6]

As with other amphiphilic molecules, above a critical aggregation concentration peptide amphiphiles associate through non-covalent interactions to form ordered assemblies of different sizes, from nanometres to microns.[11] Molecules that contain both polar and non-polar elements minimise unfavourable interactions with the aqueous environment via aggregation, which allows the hydrophilic moieties to be exposed to the aqueous environment, and the hydrophobic moieties to be protected. When aggregation occurs, a variety of assemblies can be formed depending on many parameters such as concentration, pH, temperature and geometry. The assemblies formed range from micelles to bilayer structures, such as vesicles, as well as fibrils and gels as mentioned already (Figure 1.3).[12]

Micelles consist of a hydrophobic inner core surrounded by a hydrophilic outer shell that is exposed to a solvent, and their structures can be spheres, disks or wormlike assemblies.[13] Micelles form spontaneously when the concentration is above a critical micelle concentration and temperature.[14] Amphiphiles with an intermediate level of hydrophobicity prefer to assemble into bilayer vesicles. Vesicles are spherical, hollow, lamellar structures that surround an aqueous core. The hydrophobic moiety faces inwards and forms the inner section of the bilayer, and the hydrophilic moiety is exposed to the aqueous environment on the inner and outer surface. Micelle structures have a hydrophobic interior and hydrophilic exterior.[15]

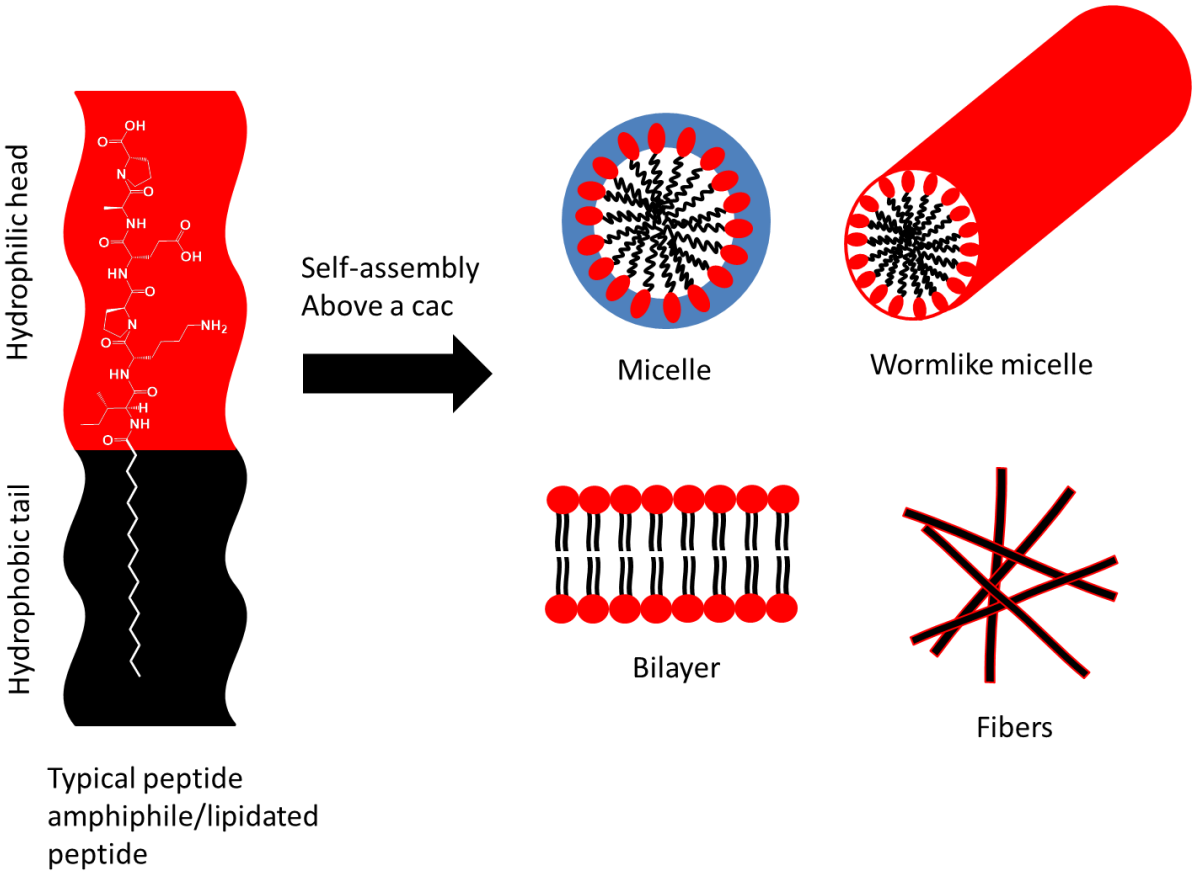

Figure 1.6. Scheme to show the possible self-assembled structures of typical peptide amphiphiles. Each amino acid is 3.5 Å long, meaning that a peptide containing 10 amino acids will be 3.5 nm approximately.[16]

There is normally a distinct relationship between the amphiphilic character of a peptide and its function in that the amphiphilic character determines the self-assembly properties, and in turn this is what gives the peptide its functionality. The level of amphiphilicity can vary significantly in peptides and proteins; as such they can display regions that are either hydrophobic or hydrophilic in nature. An example of this is the cylindrical structure of an α-helix, as it could contain a section of hydrophobic residues along one face of the cylinder and a hydrophilic section of residues on the opposite face of the cylinder. For β-sheet structures, the peptide chain can be composed of alternating hydrophilic and hydrophobic residues, so that the side chains of the residues are

displayed on opposite faces of the sheet (figure 1.3).[17] In the cell membrane peptides fold into helices and sheets to allow the non-polar residues to interact with the membrane interior, and to allow the polar residues to be exposed to the aqueous environment. This self-assembly allows the peptides to further optimise their interaction with the surroundings.

Peptide amphiphiles are very useful in biomedical applications, and can be utilised to act as therapeutic agents to treat diseases by transporting drugs across membranes to specific sites. They can then be metabolised into lipids and amino acids, which are then easily removed in the kidneys.[18] This occurs by the hydrophobic tail being able to cross the cell membrane, allowing the peptide epitope to target a specific cell by a ligand-receptor complex.[19] Other applications of peptide amphiphiles are use in antimicrobials, skincare and cosmetics, and also gene delivery to name a few.[20]

1.3 Lipidated Peptides

Lipidated peptides are a type of peptide amphiphile that incorporate one or more alkyl/lipid chains, attached to a peptide head group. As with peptide amphiphiles, they self-assemble depending on the hydrophilic/hydrophobic balance, as well interactions between the peptide units, which is dependent on the charge of the amino acid residues.[21] Lipidated peptides combine the structural features of amphiphilic surfactants with the functions of bioactive peptides, and they are known to assemble into a variety of nanostructures, similar to those mentioned for peptide amphiphiles.[6, 12]

Peptide lipidation occurs naturally and is a posttranslational modification carried out in order to maintain cellular functions, of which there are many different types. Examples include ghrelin (a peptide hormone associated with feeding), and bacterial antibiotics that aren't synthesised in the ribosome.[22] Further examples include those produced by the *Bacillus subtilis* family which are composed of a cyclic structure made up of 7-10 amino acids, and a β-hydroxy fatty acid chain of varying length ranging from 13-19 carbon atoms.[23] These can be divided into three families depending on the structure of the cyclic peptide sequence: surfactins, iturins, and fengycins.[24-26] Lipidated peptides produced by *Bacillus* strains have many useful bio-activities such as anti-bacterial, anti-viral, anti-fungal, and anti-tumour properties,[23-24] making them very attractive for use in a wide range of industries. As the name implies, surfactins are potent biosurfactants (surfactants produced by bacteria, yeast, or fungi), and they have been shown to reduce the surface tension of water from 72 to 27 mN/m at very low concentrations.[27] Furthermore, surfactins are also able to permeabilize lipid membranes, allowing them to have specific antimicrobial and antiviral activities.[24, 28-29] Since surfactins are biosurfactants, they have diverse functional properties. These include low toxicity, biodegradability and a higher tolerance towards variation of temperature and pH,[24] making them very interesting for use in a wide range of applications. Iturins are pore-forming lipopeptides with antifungal activity, and this is dependent on the interaction with the cytoplasmic membrane of the target cells.[24-25, 30] Mycosubtilin is an iturin isoform that can interact with membranes via its sterol alcohol group, to target ergosterol (a compound found in fungi) to give it antifungal properties.[23, 31] Finally, fengycins are another class of biosurfactant produced by *Bacillus subtilis*, with antifungal activity against filamentous fungi.[26, 30, 32] There are two classes of Fengycins, Fengycin A

and Fengycin B, with the two only differing by one amino acid at position 6 in the peptide sequence, with the former having an alanine residue, and the latter having valine.[33]

Daptomycin is another naturally occurring lipidated peptide, produced by the Gram positive bacterium *Streptomyces roseoporous.* The structure of Daptomycin consists of a decanoyl lipid chain attached to a partially cyclised peptide head group.[21] It has very potent antimicrobial properties and is used as an antibiotic to treat life-threatening conditions caused by Gram positive bacteria including MRSA (methicillin-resistant *Staphylococcus aureus*) and vancomycin resistant *Enterococci*.[21, 34-35] As with the *Bacillus subtillis* lipidated peptides, the permeation of the cell membrane is what gives it its properties, and the mechanism of action with daptomycin is thought to involve the insertion of the decanoyl chain into the bacterial membrane to cause disruption. This then causes a serious depolarization resulting in the inhibition of various synthesis processes including those of DNA, protein and RNA, leading to apoptosis.[36-38]

Due to the desirable properties of peptides such as high receptor affinity and bioactivity, and low toxicity, their use in therapeutics has great potential; shown by a fast growing market with over 100 approved peptide-based drugs.[39] The disadvantages are that they have low oral bioavailability and stability. Lipidation as a chemical modification tool in the development of therapeutic agents has proven to be useful in overcoming these issues, with four lipidized peptide drugs currently approved for use in humans, and various others in clinical trials.[22] Two of the approved drugs are long-acting anti-diabetic GLP-1 analogues liraglutide (Victoza®), and insulin detemir (Levemir®). The other two are the antiobiotics daptomycin, that has been discussed, and polymyxin B.

Lipidated peptides also have applications in other areas, such as use in the cosmetic industry.[21] A commercially available lipidated peptide, Matrixyl, is used in anti-wrinkle creams. Matrixyl is a pentapeptide and has the sequence KTTKS, with an attached palmitoyl lipid chain, that is able to stimulate collagen and fibronectin production in fibroblasts.[40] Several studies have shown promising results of palmitoyl-KTTKS, and topical formulations have been found to significantly reduce fine lines and wrinkles, helping to delay the aging process in the skin.[41] The Hamley group have also carried out investigations of C_{16}KTTKS, and found it so self-assemble into nanotapes in the pH range 3-7, in addition to stimulating human dermal and corneal fibroblasts in a concentration dependant manner, suggesting that stimulation occurs above the critical aggregation concentration.[42]

1.4 Peptide modification to increase stability

Many strategies have been employed to increase the stability of peptide drugs, because although they have so many desirable characteristics, they are short lived in the body as a result of rapid degradation and clearance. With half-lives of some peptides and proteins only being a few minutes, they are very ineffective in drug delivery.[43] Mechanisms involved in their clearance include peripheral blood mediated elimination by proteolysis, real and hepatic elimination, and also receptor-mediated endocytosis.[44] One of the main reasons for such rapid clearance is molecular weight. Molecules that have a low molecular weight (40-50 kDa) are rapidly cleared by renal filtration via the glomerular filtration barrier (GBM) into the urine. As a result of this, increasing the size of a peptide drug is a good starting point to improve half-life.[45]

Peptide modifications to extend half-life include PEGylation, glycosylation, cyclization, serum albumin binding, and lipidation. PEGylation is the attachment of polyethylene glycol (PEG) chains to the peptide via covalent bonds, helping to increase molecular weight, and limit enzymatic degradation as a result of steric hindrance caused by adding the PEG.[46] PEGylation offers a number of benefits for pharmaceutical applications such as improved water solubility, high mobility in solution, as well as low toxicity and immunogenicity. This does however depend on the molecular weight of the attached PEG.[43, 47] PEGylation as a method to improve half-life has been successfully demonstrated many times; in one example it was shown that site specific mono-PEGylation of GLP-1 led to a 16-fold increase in plasma half life time in rats.[48] On the other hand, covalently attaching PEG can often lead to loss of biological activity.[49]

Another chemical modification is the attachment of glycosyl (carbohydrate) units to the peptide to help with peptide delivery to target sights. The introduction of carboydrates to peptides can alter the physiological properties, to improve bioavailability. Advantages of this technique include increased metabolic stability, and facilitated transport across cell membranes, although of the most favourable aspects is their ability to promote oral absorption.[50] Peptides have a very low oral availability (less than 1-2%),[3, 51-52] as a result of insufficient absorption and rapid degradation and clearance, thus making this method an attractive one. N- and O- glycosylation in which carbohydrates are attached to the peptide are naturally occurring, where N- glycosylation occurs through the amine group of an asparagine residue to form an amide bond. O- glycosylation occurs via serine or threonine residues, where the oxygen atom on the side chain binds to the carbohydrate through an ether bond. There is also non-natural glycosylation, known as chemical

glycosylation, which involves the attachment of carbohydrate units to different amino acid residues at the N-terminus of the peptide's sequence. A further way of carrying out glycosylation is by using enzymes, known as chemo-enzymatic glycosylation. This method is used for complex chemical synthesis.[53-54] Chemical and chemo-enzymatic methods can be used for the synthesis of glycopeptides and glycoproteins.[50]

Cyclization can also be used as a method to decrease proteolytic degradation and prolong half-life, to make the peptide conformation more rigid to hinder enzymatic cleavage. This method can however lead to loss of biological function due to the reduced flexibility making the peptide inactive.[55] For example, side chain to side chain cyclization between asparagine (position 8) and lysine (position 12), of a growth regulating factor (GRF) analogue was found to increase the half-life from 17 minutes to more than 2 hours.[43]

Another way to extend half-life do is to bind serum albumin to the peptide. Human serum albumin is the most abundant plasma protein with a molecular weight of 66.4 kDa[56], and it is involved in many essential bodily functions to maintain homeostasis. As a result, albumin binding would significantly increase the molecular weight of the peptide, restricting it from being filtered into the urine by the GBM. Serum albumin has an extraordinary long half-life of 2-4 weeks which is much longer than other plasma proteins,[57] due to it binding to the neonatal Fc receptor (FcRn). Fc receptors are proteins found on the surface of certain cells that help to protect the functions of the immune system, by binding to the Fc region of antibodies, which attach to pathogens and destroy them. This mechanism of the neonatal FcRn involves albumin binding to the FcRn in an acidic pH environment to divert it from degradation in the lysosomal compartment of

the cell, and redirecting it to the plasma membrane, where it is released back into the blood plasma due to neutral pH.[58]

As mentioned above, lipidation is a further technique to use when improving peptide stability and half-life. Attaching a lipid chain to the peptide head group has been found to inhibit proteolytic attack due to the lipid chain non-covalently interacting with serum albumin to increase the molecular weight, thus reducing renal filtration. Studies on a lipidated analogue of insulin, detemir, revealed a prolonged action as a result of its affinity for human serum albumin.[59] As well as this, lipidation has been shown to enhance the interaction of peptides with cell membranes, allowing them to be up taken into the cell more readily compared to the peptide lacking the lipid moiety.[60-61] There are three types of lipidation, and they differ based on the bond formation methods between the lipid and the peptide: amidation, esterification (S- or O-) and S-bond (ether or disulphide) formation. Amidation and O-esterification form strong covalent bonds that are irreversible, whereas the other two methods are weak and reversible covalent bonds. The method used, as well as the alkyl/lipid chain, position of lipidation, and the spacer used, all have significant impacts on physiochemical properties and bioactivity.[22] The level of lipophilicity can be significantly modulated by lipidation, and since lipophilicity is detrimental for the absorption, distribution, metabolism, and excretion of drugs, it provides a way of fine tuning peptides for use in therapeutics.

A study on lipidation and PEGylation on the GLP-1 peptide was carried out and the results showed that lipidation had no significant effect on peptide activity *in vitro*,[62] whereas PEGylation did, especially when the PEG is attached to internal amino acids of the peptide e.g. positions 20 and 21. The reduction in activity from PEGylation compared

to lipidation is due to the loss of receptor affinity, and it is suggested that this is because of its increased molecular weight which causes steric hindrance.[63-64]

1.5 Hydrogels

Hydrogels are three dimensional supramolecular assemblies formed by cross-linking of polymer networks, that are able to absorb large amounts of water.[65] Peptides can form hydrogels by non-covalent interactions of self-assembled structures to establish well-ordered scaffolds, and these can be very useful in biotechnological and medical applications, in particular for use as slow drug delivery systems. Lipidated peptides can also form hydrogels, since the increased hydrophobic interactions from the addition of the hydrophobic chain facilitates its self-assembling ability.[66] Hydrogels can be classified as either chemical or physical gels, with the former having covalent cross-linking bonds, and the latter having non-covalent bonds, as in the case of peptide hydrogels.[67] Chemical hydrogels result in strong irreversible gels due to the covalent bonding, and they may also possess harmful properties which makes them unfavourable for medical applications. Physical hydrogels on the other hand have high biocompatibility, aren't toxic, and are also easily reversible, by simply changing an external stimulus such as pH or temperature; thus they are favourable for use in medical applications.

There are two suggested mechanisms behind physical hydrogel formation, the first one being the gelation of nanofibrous peptide assemblies, usually observed for oligopeptide precursors. The precursors self-assemble into fibers, tapes, tubes, or ribbons that entangle to form non-covalent cross-links. The second mechanism involves non-covalent interactions of cross-linked domains that are separated by water-soluble linkers, and this is usually observed in longer multi-domain structures.[68] Tuning of the

supramolecular interactions to produce a self-supporting network that does not precipitate, and is also able to immobilize water which is vital for to gel formation. Most oligopeptide hydrogels have a β-sheet structure, and assemble to form fibers, although α-helical peptides have also been reported.[69-70] Figure 1.7 shows the typical mechanism of gelation where the oligopeptide precursors self-assemble into fibers that become elongated, and entangle to form cross-linked gels.

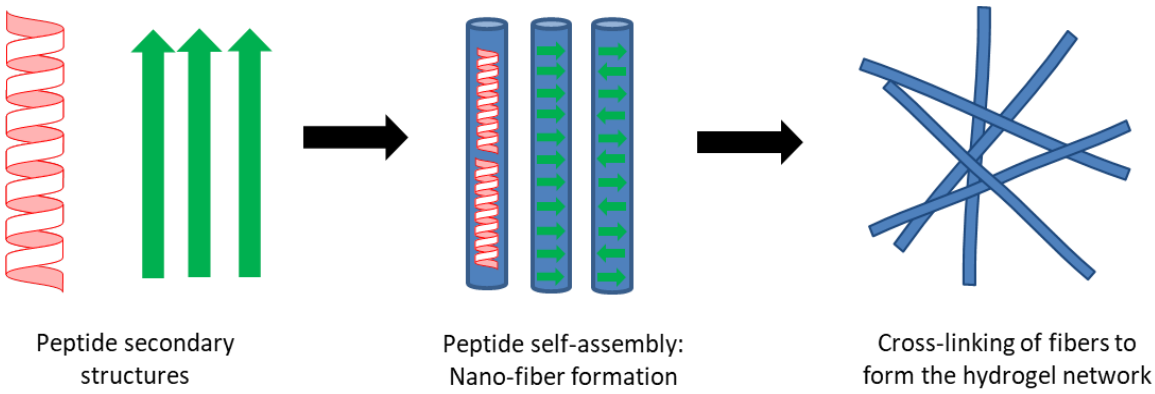

Figure 1.7. Simplified scheme to show the self-assembly process involved in hydrogel formation.

Peptides based hydrogels possess exceptional biocompatibility and biodegradability qualities, giving rise to their wide use of applications, particularly in biomedicine; as such, their physical properties can be fine-tuned in order to maximise their use. Methods to do this are: modulation of the amino acid sequence, pH, chirality, and increasing the number of aromatic residues.[71] The order of amino acids within the sequence is crucial for gelation, as has been shown many times. In one example, a short peptide sequence Fmoc-Phe-Gly readily formed a hydrogel, whereas Fmoc-Gly-Phe failed to do so as a result of the two adjacent aromatic moieties being moved, hindering

the aromatic interactions.[72-73] Altering the pH can also have similar effects, an example involved the use of the naphthalene (Nap) modified dipeptides Nap-Gly-Ala, and Nap-Ala-Gly, where a drop in pH induced gelation of the former, but led to crystallisation of the latter.[74] A controlled pH decrease method using glucono-δ-lactone (GdL), where the GdL is hydrolysed to gluconic acid in water is a recent strategy that has been developed as a way to form homogeneous and reproducible hydrogels.[75-76] The hydrolysis is slow, which allows for a uniform pH change, and thus resulting in reproducible homogenous gels. In addition to this, the desired pH can be achieved by altering the amount of GdL added. The use of GdL has been used various times for the hydrogelation of Fmoc and Nap-dipeptides.[75-76] In another direction, Morris et al reported the use of GdL as a 'molecular trigger' to predict and control the order of gelation.[77] Chirality also plays an essential role in gel formation, and even changing the chirality of a single amino acid from its natural L-amino acid to its unnatural D-amino acid can significantly impact the gelation properties, with the natural forms not forming gels.[78] Furthermore, aromatic interactions play a key role in hydrogel formation as a result of π- π stacking driving gelation, shown by many studies.[79-80]

1.6 Peptide hormones

Peptide hormones are hormones made up of amino acid chains that primarily have an effect on the endocrine system. Based on the building units, the hormones can be classified as either amino-acid based, or steroid based systems. The former are water soluble due to their composition comprising of amino acids, allowing them to act on the surface of target cells via secondary messengers. This differs from steroid hormones

which are lipid soluble, and so can move through the plasma membranes of target cells and act within the nuclei.[81]

The endocrine system is composed of many different glands and it can be divided into two categories: classical and non-classical. In the endocrine system, hormones are secreted into the circulatory system where they are distributed throughout the body, regulating bodily functions. The classical endocrine glands include the, pituitary gland, pancreas, thyroid gland, adrenal cortex and medulla. The primary function of these glands is to manufacture specific hormones. Non-classical endocrine glands include the heart, hypothalamus, kidneys, liver, and the gastrointestinal tract. Many of the classical hormones are controlled by the hypothalamus and pituitary which can also be classified as being an extension of the nervous system.[82]

An imbalance of hormones or an inappropriate bodily response to them indicates a disorder of the endocrine system, with the most common one being diabetes. There are two types of diabetes: type I and type II; the former is due to the pancreas failing to produce enough insulin, and the latter is where cells fail to respond to insulin. Type II diabetes is associated with obesity, and is therefore controllable with lifestyle choices such as diet and exercise.

1.7 Gut-brain interactions

The gut-brain axis allows the two-way communication between the gastrointestinal tract (GI) and both the central (CNS) and enteric nervous system (ENS), allowing the

body to link emotional and cognitive processes of the brain with peripheral intestinal functions.[83-84]

Gut-brain interactions are increasingly recognised as playing an important role in determining overall food intake.[85] Many peptides are synthesised and released from the gastrointestinal tract, and it has been shown that they physiologically influence eating behaviour via gut-brain signalling.[86] Ghrelin is an orexigenic (appetite stimulating) peptide produced in the stomach which acts as a meal initiator. This differs from peptide YY, Pancreatic polypeptide, glucagon-like peptide 1 (GLP-1), oxyntomodulin, and cholecystokinin which are all derived from the intestine and pancreas, and have been shown to produce satiety signals. From this it has been suggested that gut hormones can be manipulated to regulate energy balance, and as a result gut hormone based therapies could be a possible treatment for obesity.[86-87]

Although the full mechanism of gut-brain interactions are extremely complex, a vital component of the hypothalamic metabolic regulatory circuit is the arcuate nucleus and the vagus nerve.[86] Vagal afferent neurons express two different neurochemical phenotypes that either inhibit or stimulate food intake.[88] These are: neuropeptide Y (NPY) and agouti-related neuropeptide (AgRP), which act to stimulate food intake and pro-opiomelanocortin (POMC) that inhibits feeding. The balance in activity of these neuronal circuits is critical to body weight regulation.[86] As shown in Figure 1.7, many gut hormones have direct access to the hypothalamus, brainstem and vagus nerve. They also have a significant impact on feeding in reaction to calorific intake, which is the case for $PYY_{3-36,}$ via Y2 receptors.[89] Further discussion of PYY_{3-36} and Y2 receptors is presented in chapter 2.

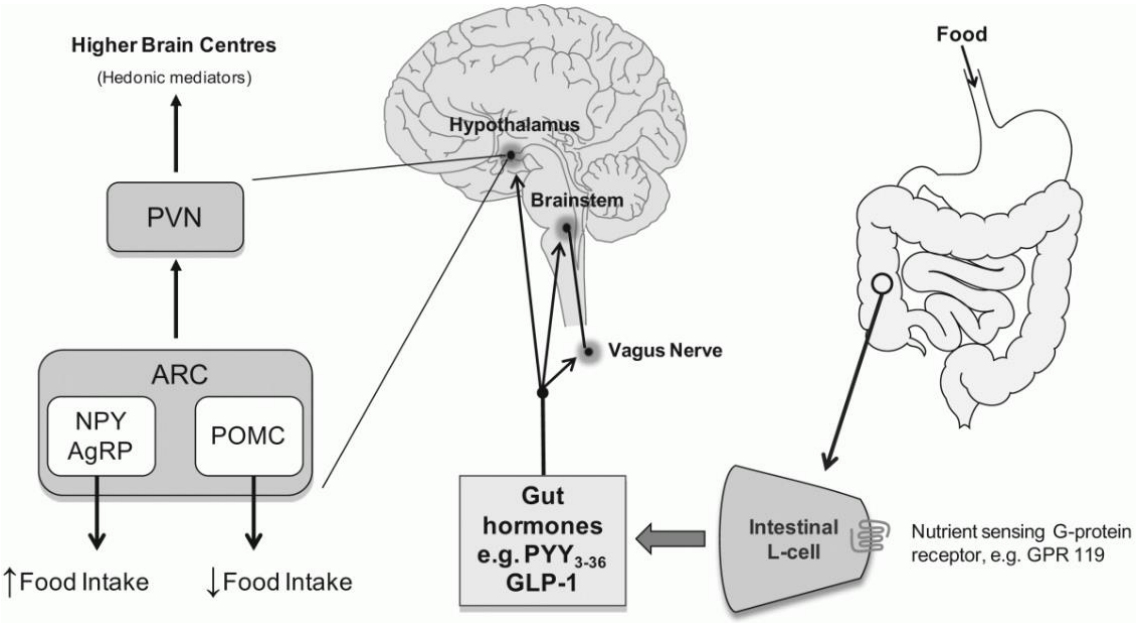

Figure 1.8. Gut-brain axis to show the regulation of food intake. Food is digested and G-protein coupled receptors are activated, causing gut hormones to be released in the L-cells of the GI tract. The gut hormones are able to influence food intake via the vagus nerve, the brainstem, and the hypothalamus. Within the arcuate nucleus (ARC) of the hypothalamus , peripheral signals are given off via neurons (NPY, AgRP, and POMC) to stimulate or inhibit food intake.[90]

1.8 Gastrointestinal peptide hormones

1.8.1 Leptin

Leptin is a hormone made by adipose cells that affects many biological mechanisms including: reproduction, the immune and inflammatory response, haematopoiesis, angiogenesis, bone formation, and wound healing. More interestingly however, Leptin helps to regulate energy balance by inhibiting hunger. This happens via a feedback mechanism where signals are sent to key regulatory centres in the brain to inhibit food intake.[91]

After Leptin is released by adipose tissue into the bloodstream, it crosses the blood brain barrier (BBB) and binds to the hypothalamic leptin receptors. This affects the activity of many hypothalamic neurones, and the expression of various orexigenic (appetite stimulating) and anorexigenic (appetite inhibiting) neuropeptides. Orexigenic peptides include neuropeptide Y (NPY), and anorexigenic peptides include pro-opiomelanocortin (POMC) as mentioned above. It has been suggested that the interaction of both types of these neuropeptides is what provides leptin with its mechanism of action in the hypothalamus to inhibit hunger.[91]

1.8.2 Ghrelin

Ghrelin is a 28 amino acid peptide with an octanoylated serine residue at position 3,[92] and is produced and secreted by cells within the oxyntic glands (acid secreting glands) of the stomach.[87] Peripheral administration of ghrelin has been shown to stimulate food intake and decrease fat utilization. This means it is involved in energy homeostasis, with the serine residue appearing to give ghrelin these effects.[92] Ghrelin's function is unique compared to other gut hormones, where it acts to increase food intake rather than decrease it, making it a very important component of weight control. A study on mice that were lacking ghrelin showed evidence of this and were found to be resistant to diet-induced obesity when fed a high-fat diet. This was due to them eating less, and therefore utilizing more stored fat as an energy source.[87]

1.8.3 Cholecystokinin (CCK)

Cholecystokinin (CCK) is an endogenous gut hormone mainly found in the duodenum and jejunum, that exists in several molecular forms with differing numbers of amino acids. Examples include CCK-8 and CCK-54 (the number indicates the number of amino

acid residues). CCK is known to act as a postprandial satiety signal and it acts via two receptors: CCK_1 and CCK_2. The CCK_1 receptor is more important in appetite control.[92] The receptors are located on the peripheral vagal afferent terminals, which transmit signals to part of the brain stem that is associated with appetite, such as the nucleus of the solitary tract.[87]

1.8.4 Oxyntomodulin (OXM)

Oxyntomodulin (OXM) is a 37 amino acid peptide expressed in the central nervous system and the L cells of the intestine and pancreas.[93] OXM seems to mediate its effects via the glucagon-like peptide 1 (GLP-1) receptor as shown in experiments carried out on rat parietal cells.[94] This has been proven by its anorectic actions being blocked when administration of the GLP-1 antagonist was carried out.[95] Intravenous administration of OXM in humans inhibits gastric emptying and gastric acid secretion, which leads to a feeling of satiety.[96] This feeling of satiety can cause a reduction in both food intake and overall body weight, and this is brought about by the suppression of ghrelin.

1.8.5 Glucagon-like peptide 1 (GLP-1)

Glucagon-like peptide 1 (GLP-1) is a 30-amino acid gut derived incretin (decreases blood glucose levels) peptide hormone,[97] meaning that it stimulates insulin secretion in response to eating, resulting in suppressed glucagon secretion. In addition to this, GLP-1 inhibits gastric emptying, and reduces appetite and food intake.[98] GLP-1 is produced in the intestinal epithelial endocrine L-cells in the distal small bowel and colon by differential processing of proglucagon.[97-98] Proglucagon is a gene expressed in the L-cells and is regulated in the gut and brain.[97] Within minutes of food intake, the plasma levels of GLP-1 rise rapidly. GLP-1 exists in two circulating molecular forms: GLP-1(7-37) and

GLP-1(7-36) amide, with GLP-1(7-36) amide representing the majority of circulating active GLP-1 in human plasma. Both forms of GLP-1 are rapidly metabolised and inactivated by the enzyme dipeptidyl peptidase-4 (DPP-4) to GLP-1(9-37), or GLP-1(9-36)amide following the release from gut L cells.[99] DPP-4 is a widely expressed enzyme that cleaves both forms of GLP-1 at the position 2 alanine of the N-terminal to make them inactive. The expression of DPP-4 in the gut and vascular endothelium explains the short half-life of GLP-1 of just several minutes, because the majority of immunoreactive GLP-1 entering the portal venous circulation has already been inactivated by N-terminal cleavage.[100]

1.8.6 Pancreatic Polypeptide (PP)

Pancreatic polypeptide (PP) is a 36-amino acid peptide belonging to the family containing neuropeptide Y (NPY) and peptide YY (PYY). All of these peptides are members of the PP fold peptide family and they consist of a signal peptide, followed by a 36 amino acid active peptide and a carboxyl-terminal.[101] The PP fold family bind to receptors Y1-Y6, but PP in particular has the highest affinity for the Y4 and Y5 receptors.[92] The Y-receptors belong to the G protein- coupled receptor family, and they mediate a wide variety of physiological effects such as regulation of blood pressure, anxiety, memory retention, hormone release, and food intake.[102]

PP is similar to GLP-1, where it is released into circulation after the ingestion of food, except it is produced in the endocrine F cells, located in the periphery of pancreatic islets, whereas GLP-1 is produced in the L-cells of the GI tract.[103-104] PP is responsible for a number of regulatory actions, such as the inhibition of pancreatic exocrine secretion, and the modulation of gastric acid secretion, and gastric emptying.[105-106] The amount of

PP released is affected by the digestive state, i.e. release is very low in the fasted state, but is significantly increased throughout all phases of digestion. In addition to this, a decrease in blood glucose levels and insulin induced hypoglycaemia are stimuli for PP secretion in the brain. As a result, it is thought that PP could potentially play a significant role in the regulation of feeding behaviour to control energy homeostasis.[103]

1.8.7 Peptide YY

Peptide YY (PYY) is a gut hormone belonging to the pancreatic polypeptide (PP) fold family, along with PP and neuropeptide Y (NPY) as mentioned above. The PP-fold motif is found throughout this family and relates to the 3D structure. The PP-fold is formed through the incorporation of certain residues which are predominately Pro2, Pro5, Pro8, Gly9, Tyr20 and Tyr27. This PP-fold has been found to protect the peptide against enzymatic attack as well as producing a hydrophobic pocket which is inherently overall energy reducing. In addition to containing the PP-fold motif, PYY and its derivative PYY_{3-36} also have a high C-terminal α-helix proportion, suggested to be extremely important for the structural integrity of PYY. The sequence of the 36-amino acid peptide, PYY, is: Tyr-Pro-Ala-Lys-Pro-Glu-Ala-Pro-Gly-Glu-Asp-AlaSer-Pro-Glu-Glu-Leu-Ser-Arg-Tyr-Tyr-Ala-Ser-Leu-Arg-His-TyrLeu-Asn-Leu-Val-Thr-Arg-Gln-Arg-Tyr-NH_2.[107]

PYY is released by the L-cells of the gastrointestinal tract following food intake, and there are two main endogenous forms: PYY_{1-36} and PYY_{3-36}. PYY_{1-36} is rapidly processed by the enzyme DPP4 to the 34-amino acid peptide PYY_{3-36}.[108] DPP4 hydrolyses PYY and removes the first two amino acids, tyrosine and proline, at the N-terminal, which changes the receptor selectivity. As a result of this, PYY_{3-36} has a high selectivity for the Y2-receptor, compared to PYY_{1-36} which has selectivity for the Y1, Y2, and Y5 receptors. It is thought

that the Y_1 receptor requires both the C-terminus and N-terminus for recognition, binding and then subsequent activation. The Y_2 receptor is thought to have a smaller receptor site and also only requires the C-terminus for recognition (figure 1.8).

This could explain the reduced affinity for PYY_{3-36} on any other Y receptor other than Y_2.[109] Other studies replacing the amide bonds with ester bonds also confirm that the end section is important in binding and activation.[110] The Y_2 receptors are located in the hippocampus, sympathetic and parasympathetic nerve fibres, intestines, and certain blood vessels, and have been implicated in regulating food intake and gastric emptying.[111] As a result of this, the Y_2 receptor is considered a target for the treatment of obesity and type II diabetes.

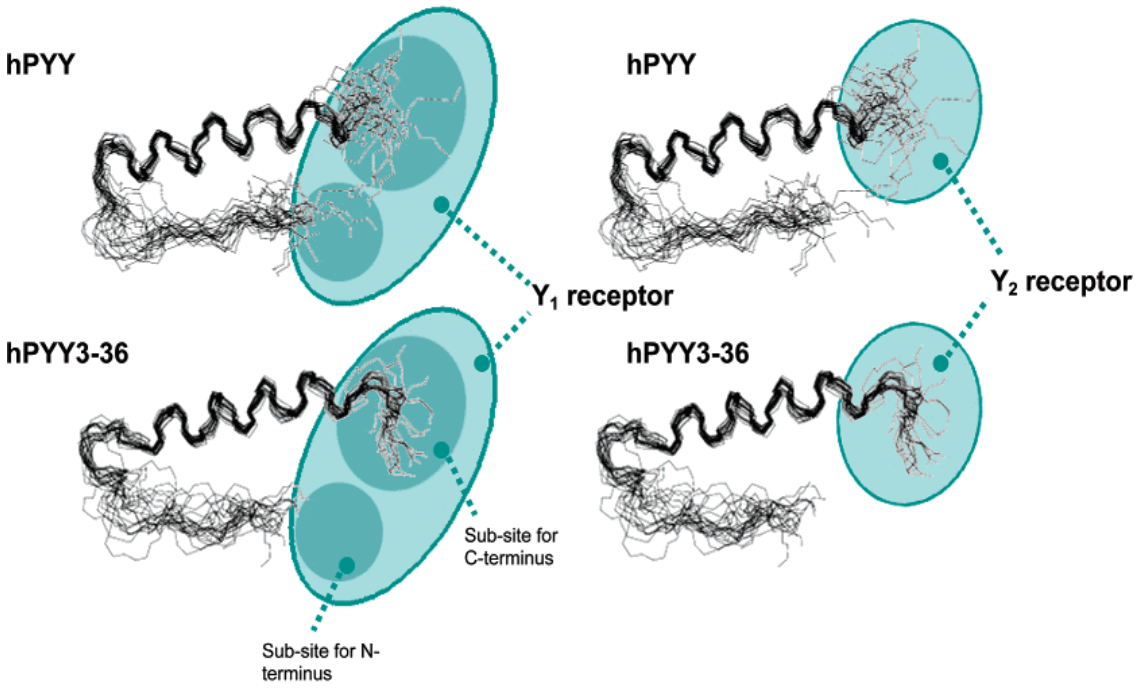

Figure 1.9. Illustrations of binding sites for Y1 and Y2 with hPYY + $hPYY_{3-36}$.[109]

1.8.8 Neuropeptide Y (NPY)

Neuropeptide Y (NPY) is also a 36 amino acid peptide that has a very similar sequence homology to peptide YY (PYY) and PP. NPY differs from the other two peptides however, by acting as a neurotransmitter rather than a hormone.[112] NPY is one of the most abundant peptides found in the brain [113] and it is synthesised and released by neurons, which in the peripheral nervous system are mostly sympathetic neurons.[112] NPY is associated with various biological responses including increased food intake, enhanced cognitive function associated with learning and memory, and also reduction in anxiety.[114] Furthermore NPY has been shown to induce vasoconstriction in peripheral blood vessels.[115] Studies of NPY and its receptors suggest that it could be directly related to various pathological disorders such as obesity, depression and epilepsy.[116]

1.9 Peptide therapeutics

There are many peptide therapeutics on the market at present. Due to their high specificity, potency, and low toxicity, the number is only going to increase.[117-119] Table 1.1 shows some of the leading peptide therapeutics. Not all of these peptide therapeutics self-assemble or are formulated as solutions, but the table shows the extent and importance of the use of peptides as drugs.

The current highest selling marketed diabetic drug Liraglutide, incorporates a lipid chain to extent plasma circulation and ensures prolonged bioavailability.[120-121] Liraglutide is a GLP-1 agonist drug that self-assembles into an alpha-helical structure, and it requires once a day administration.[122] Lipid conjugation of a palmitoyl chain to a lysine residue

at position 26 of Liraglutide results in an extended half-life (around 13-14 hours) in the blood. This is due to the palmitoyl chain allowing non covalent binding to albumin, which delays proteolytic attack by DPP IV and also rapid renal clearance. Furthermore, the addition of the lipid chain could further prolong half-life by sterically hindering the DPP IV enzyme from degradation.[123]

Another peptide known to self-assemble is the octapeptide, Lanreotide. This compound is a synthetic analogue of the peptide hormone somatostatin and it is used to treat acromegaly [124] (a condition where the body produced too much growth hormone). In water, Lanreotide self-assembles into monodisperse liquid crystalline nanotubes. The nanotubes are made up of dimers that self-assemble into a 2D crystal, which is held together by lateral chain interactions, and also by antiparallel ß-sheets.[124] [125]

Further insight into how self-assembly and peptide hormones are related has been provided by studies on self-assembling amyloid structures formed by peptide hormones and neuropeptides. Peptide hormones and neuropeptides form dense-cored aggregates that pack into dense-core vesicles (DCVs), which are used to temporarily store peptide messengers in secretory cells.[126] When DCVs are triggered, they release the stored information into the blood or extracellular space,[127] resulting in amyloid disassembly, in order for action.[126] Therefore for these types of peptides, reversibility of peptide aggregation is essential for their function.

Table 1.1. Peptide Therapeutics on the Market.

Trade Name	Peptide	Company	Molecular Properties	Related Reference
Copaxone	Glatiramer	Teva	Four amino acids (L-glutamic acid, L-alanine, L-lysine, and L-tyrosine) in a defined molar ratio	128-129
Lupron	Leuprolide	Abbott	Synthetic nonapeptide analogue of naturally occurring gonadotropin-releasing hormone (GnRH or LH-RH)	130-131
Vicoza	Liraglutide	Novo	97% homologous to native human GLP-1 (7-37) by substituting arginine for lysine at position 34 & addition of a fatty acid chain	132
Zoladex	Goserelin	AZ	Natural LHRH/GnRH decapeptide with two substitutions to inhibit rapid degradation.	133-134
Sandostation	Octreotide	Novartis	Longer acting synthetic octapeptide analogue of naturally occurring somatostatin	135-136
Forteo	Teriparatide	Lilly/Amylin	Recombinant form of parathyroid hormone consisting of the first (N-terminus) 34 amino acids, which is the bioactive portion of the hormone	137-138
Byetta	Exenatide	Lilly/Amylin	Synthetic version of exendin-4, a hormone found in the saliva of the Gila monster	139-140
Cubicin	Daptomycin	Cubist	Cyclic lipopeptide, consists of 13 amino acids, 10 of which are arranged in a cyclic fashion, and three on an exocyclic tail	141-142
Integrilin	Eptifibatide	Merck	Cyclic heptapeptide composed with S-S bridge, 2 unnatural building blocks and amide	143-144
Angiomax/Angiox	Bivalirudin	Medicines	20-amino acid polypeptide	145-146
Fortical	Calcitonin	Upsher-Smith	32 amino-acid polypeptide similar to calcitonin	147-149
Somatuline	Lanreotide	Ipsen	Cyclic peptide that is a long acting analogue of somatostatin.	150-151

1.10 Physical characterisation techniques

1.10.1 Circular dichroism (CD)

Circular dichroism is a spectroscopic technique used to study biological molecules, in particular the secondary structure of peptides and proteins. Since secondary structure is sensitive to its environment, CD is a good way of observing how secondary structure changes with environmental conditions such as temperature and pH. This can then give an estimation of its conformation.

CD is a result of the interaction of polarised light with chiral molecules, and it is defined as the unequal absorption of left and right handed circularly polarised light (Equation 1.1). This occurs because when chiral molecules interact with light, one circularly polarised light state is absorbed to a great extent than the other, to produce a CD signal that is non-zero.[152] Depending on which circularly polarised light (left or right) is absorbed more, determines if the CD plot is positive or negative. If the left hand circularly polarised light is absorbed to a greater extent, then the signal will be positive and vice versa. The absorbance change is written as

$\Delta A(\lambda) = A(\lambda)_{LCPL} - A(\lambda)_{RCPL}$ (Equation 1.1)

LCPL = left handed circularly polarised light
RCPL = right handed circularly polarised light
λ = wavelength

CD spectra in the far UV region (below 260 nm), can be used to measure secondary structure, and also predict the percentages of each one present in the molecule. Each

secondary structure has distinctive peaks in the spectrum, for example peptides or proteins containing α-helices have negative bands at 222 nm and 208 nm, and a positive band at 193 nm. Antiparallel β-pleated sheets have negative bands near 216 nm and positive bands at 195 nm. Disordered structures have very low ellipticity above 210 nm and negative bands at around 195 nm.[152]

1.10.2 Fluorescence spectroscopy

Fluorescence occurs when an electron relaxes back to its ground state from an excited singlet state, where it releases a photon in the process. In most cases, the emitted photon has a longer wavelength than the excitation wavelength, and therefore a lower energy than the absorbed radiation; this is known as the Stokes shift. The Jablonski diagram is used to describe the fluorescence mechanism of most molecules by illustrating the electronic states of molecules and the transitions between them (Figure 1.10). When a molecule becomes excited, it transitions from its ground state, S_0, to either a singlet first electronic excited state, S_1 or to a second electronic excited state, S_2. At each excited energy level, fluorophores have multiple vibrational levels, represented by the multiple lines in each electronic state (Figure 1.10). As the molecule loses energy and returns to its ground state, S_0, a fluorescent photon is released.

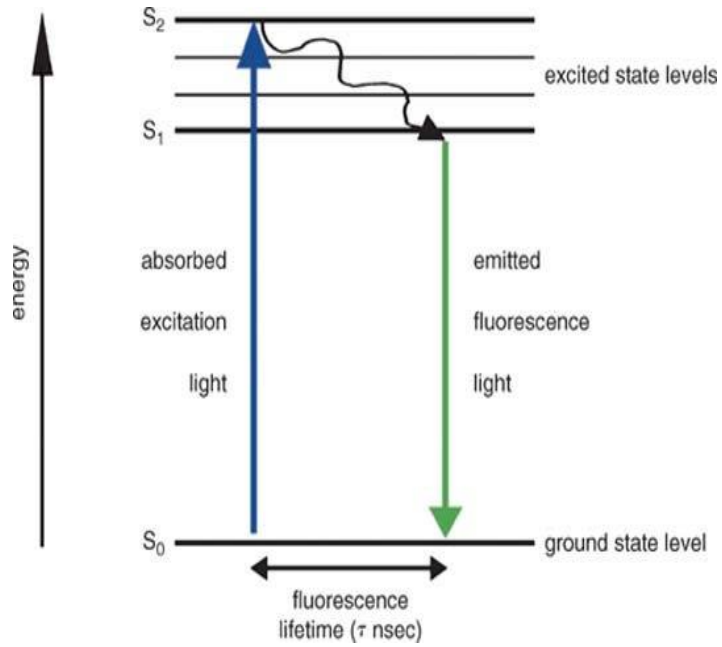

Figure 1.10. Illustration of the Jablonski diagram to show the mechanism of fluorescence.[153]

Compounds that fluoresce are known as fluorophores and generally they have one or more aromatic groups in the structure; although non-fluorescent compounds can also fluoresce by the addition of a fluorescent probe containing aromatic structures.

Fluorescence instruments contain three basic components: a light source, a sample holder, and a detector. In fluorescence spectroscopy, a beam is passed through the sample in solution at a wavelength ranging from 180-800 nm, and the light emitted by the sample is measured by the detector. The light can be measured either by the excitation spectrum (light absorbed) or the emission spectrum (light emitted). Fluorescence spectroscopy is used to determine the concentration of a compound in solution based on its fluorescence properties, and the concentration is directly proportional to absorbance, shown by the Beer-Lambert law: $A = \varepsilon\ l\ c$, where A is

absorbance, ε is the molar extinction coefficient ($M^{-1}.cm^{-1}$), l is pathlength (cm), and c is concentration (M).

There are several factors that affect the intensity of the fluorescence spectrum, and it depends on the excitation wavelength, the concentration of the sample, the pathlength of the cuvette, and the self-absorption of the sample.

1.10.3 Cryo-TEM and TEM

Transmission electron microscopy (TEM) is a high resolution microscopy technique where a beam of electrons is transmitted through a thin sample specimen (<100 nm thick), to form an image, as a result of the transmission of electrons through regions of the sample with different density. Electrons have a much shorter wavelength than visible light, resulting in a resolution limit of a TEM being around a thousand times smaller than a light microscope.[154] The increased resolution allows structures at the nanoscale to be studied, such as bacteria and viruses.

Electrons are emitted by a negatively charged electron gun (cathode), which may be a tungsten filament needle, or a lanthanum hexaboride source. The electrons are accelerated by a series of anodes at a high voltage and under vacuum to reduce the amount of electrons colliding with the air. Typical voltages used range from 60-200 kV depending on the type of sample, but for biological samples a range of 60-100 kV is used to reduce the amount of sample damage.

TEM instruments use a range of electromagnetic lenses which consist of copper coil wires inside iron pole pieces, to create an electric field, and they help to focus the electron beam and magnify the image. There are three main lenses: the condenser lens,

the objective lens, and the projector lens. The condenser lens is used to focus the electron beam onto the specimen, the objective lens is used primarily to focus and initially magnify the image. Finally the projector lens is used to further magnify the image and project it onto the imaging device such as a CCD camera.

Apertures are also used in TEM to decrease the beam intensity, and to remove electrons that are scattered to high angles, as a result of spherical or chromatic aberration, or from diffraction.[155] The condenser aperture is used to control the fraction of the beam that is allowed to hit the sample, and the objective aperture is used to select which beams in the diffraction pattern contribute to the image, thus producing a diffraction contrast.

The electrons that pass through the sample can be diffracted by crystalline samples, resulting in diffraction patterns that give information about the crystal structure of the sample. Using a TEM in diffraction mode can be used in conjunction with X-ray diffraction to determine crystal structures.

Sample preparation can be quite complex in TEM, especially for biological samples as they often require negative staining to increase the contrast (electron density difference), and reveal the structure. Negative staining involves the surrounding of biomolecules with a thin layer of a heavy metal salt such as uranyl acetate.

Cryogenic transmission electron microscopy (cryo-TEM) uses the same technique as TEM but at cryogenic temperatures. Aqueous samples are plunge frozen in liquid ethane, allowing the structure of biomolecules in solution to be determined without the need for crystallisation.

1.10.4 Small angle X-ray scattering

Small angle X-ray scattering (SAXS) is a small angle scattering technique used to investigate the shape and size of nanostructures from 1-100 nm in a typical set up, with a scattering angle ranging from 0.1-10 ^{o}. In a SAXS instrument a monochromatic beam of X-rays is sent through a sample, where some interact and are scattered by the sample to produce a scattering pattern containing information on the structure. By measuring the angle-dependant distribution of the scattered intensity, the average particle structure can be determined.[156]

There are five main basic components of a SAXS instrument: an X-ray source, a collimation system, a sample holder, a beam stop, and a detection system. The X-ray source irradiates the sample and in lab based systems this is usually a sealed X-ray tube, a microfocus X-ray tube, or a rotating anode. Synchrotron facilities are often favoured though as they can provide a higher flux and can provide X-rays of all wavelengths as a result of the production of Bremsstrahlung, therefore producing a continuous wavelength spectrum. The collimation system is used to narrow the beam, reducing its intensity. There are two types of collimation: point collimation, where the beam is shaped to a small circular or elliptical spot, and line collimation where the beam is confined only in one dimension to give a long but narrow beam. This results in a larger illuminated sample volume and a bigger scattered intensity. The sample holders vary significantly depending on the type and state of sample being measured, and usually they are handmade. The function of the beam stop is to protect the detector from being damaged by the X-ray beam, and the detection system can be wire detectors, CCD detectors, imaging plates, and solid-state detectors.

Scattered radiation can have the same wavelength or a different wavelength than the incident radiation, as a result of scattering being able to occur with or without the loss of energy. Scattered radiation that has a different wavelength is known as inelastic scattering, such as Compton scattering, and scattered radiation with the same wavelength as the incident radiation is known as elastic scattering, such as Rayleigh or Thomson.[157] SAXS analyses elastic scattering at small angles.

The interaction of X-rays with the structure produces an interference pattern at the detector, which are either constructive (in phase), or destructive (out of phase), depending on the observational angle 2θ, the orientation, and the distance r of the atoms from each other. In constructive interference, a bright spot is produced at the detector, whereas for destructive interference the radiation waves extinguish each other, producing a dark spot at the detector. The result is a 2D interference pattern, characteristic to the internal structure of the sample to give information on the orientation and distances of atoms relative to one another. The scattering angle (2θ) depends to the wavelength of the applied radiation through Bragg's Law. To overcome this and become independent from the wavelength the scattering pattern is presented as a function of q (length of the scattering vector), where $q = \frac{4\pi \sin\theta}{\lambda}$ with units of nm^{-1}. Form factors give information about the shape of particles, but require the particles to be in a dilute system where they can be considered as independent scatters without any interactions. The form factor also assumes that particles are monodisperse, but if they are polydisperse, then an average scattering pattern of all of the different sizes are obtained.[158]

In more concentrated systems where the particles are densely packed, the distances between the particles become similar to the distances inside the particles. This results in the interference pattern containing contributions from the neighbouring particles. The addition of this interference is multiplied with the form factor of a single particle to become the structure factor. The structure factor therefore contains information about the positions of particles with respect to each other and is calculated using the equation: $I(q) = P(q)S(q)$, where $I(q)$ is the intensity as a function of q, $P(q)$ is the form factor, and $S(q)$ is the structure factor.[159] An increase in intensity generally indicates an attractive interaction, suggesting aggregation of particles. When particles aggregate they can align into an ordered arrangement to create a crystalline structure, creating distinct peaks in the scattering intensity profile. These are known as Bragg peaks, and using Bragg's law it is possible to determine the distance, d, between aligned particles: $d = 2\pi/q$.[160]

1.10.5 Fibre X-ray diffraction

Fiber X-ray diffraction (XRD) is a form of X-ray scattering used to determine the structural information of a molecule, by the production of a fibre pattern from the scattered X-rays. The technique is suitable for investigation of samples that form fibres or stalks, and as such is used to investigate amyloid and related peptides.[161-162] This technique is similar to SAXS, except the sample-detector distance is shorter, thus giving diffraction patterns at wider angles. Similar to SAXS, the distance between the regularly spaced atoms in a crystalline structure can be measured by determining the d-spacing using Bragg's law. In fibre diffraction the sample has cylindrical symmetry around an axis (the fibre axis) and the ideal fibre pattern contains 4-quadrant symmetry, where the fibre axis is called the meridian and the perpendicular direction is called the equator. An

example of an orientated and un-orientated fibre diffraction pattern is shown in Figure 1.11 by the Serpell group.[163]

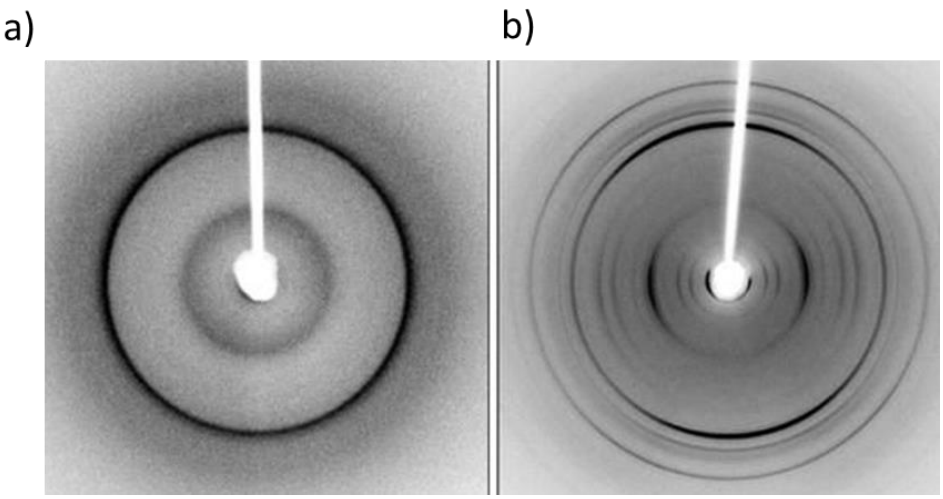

Figure 1.11. Fibre diffraction pattern of amyloid fibrils. a) orientated sample, b) un-orientated sample.[163]

1.11 Aims

The overall aim of the research conducted in this thesis is to investigate the self-assembly of lipidated derivatives of the gastrointestinal peptide hormone, PYY_{3-36}, and truncated fragments of it, with changes in temperature, pH, and concentration. The results are then compared with the native peptides, to understand the impact of lipidation on self-assembly. The idea is to develop a further understanding of lipidation as a potential chemical modification tool, to increase the stability of peptide based drugs, which in this case is for use in obesity and type II diabetes treatment.

More specifically, the aims are:

- To investigate the self-assembly of PYY_{3-36}, and three lipidated derivatives, with palmitoyl chains attached via a γ-glutamic acid spacer, to a lysine residue on the peptide at positions 11, 17, and 23.
- To investigate the possibility of hydrogel formation of PYY_{3-36}, and the three lipidated derivatives.
- To investigate the self-assembly of various N-terminal truncated fragments of PYY_{3-36}, and understand the impact of lipidation with palmitoyl chains on the self-assembly.
- To study the possibility of hydrogel formation of the truncated fragments and their lipidated derivates.
- To understand the use of a PYY_{3-36} truncated lipidated fragment with a free proline residue (PAEPKI-NH-$C_{16}H_{33}$) as a catalyst in aldol reactions.

- To carry out cytotoxicity assays on the truncated PYY_{3-36} peptides, using a human colon cancer cell line (HCT-116), to understand the impact of lipidation on toxicity.

1.12 References

1. Xiubo Zhao, F. P., Jian R. Lu, Recent development of peptide self-assembly *Progess in Natural Science* **2008**, 653-660.
2. Drew, R. C.; Gordy, W., Electron Spin Resonance Studies of Radiation Effects on Polyamino Acids. *Radiation Research* **1963,** *18* (4), 552-579.
3. Mandal, D.; Nasrolahi Shirazi, A.; Parang, K., Self-assembly of peptides to nanostructures. *Org Biomol Chem* **2014,** *12* (22), 3544-61.
4. Whitesides, G. M.; Boncheva, M., Beyond molecules: self-assembly of mesoscopic and macroscopic components. *P. Natl. Acad. Sci.* **2002,** *99* (8), 4769-4774.
5. I.W.Hamley, Lipopetides: from self-assembly to bioactivity. *The Royal Society of Chemistry* **2015**, 8574-8583.
6. Cui, H. G.; Webber, M. J.; Stupp, S. I., Self-Assembly of Peptide Amphiphiles: From Molecules to Nanostructures to Biomaterials. *Biopolymers* **2010,** *94* (1), 1-18.
7. Lin, L.; Pinker, R. J.; Kallenbach, N. R., Alpha-helix stability and the native state of myoglobin. *Biochem.* **1993,** *32* (47), 12638-43.
8. Rad-Malekshahi, M.; Lempsink, L.; Amidi, M.; Hennink, W. E.; Mastrobattista, E., Biomedical Applications of Self-Assembling Peptides. *Bioconjugate Chem* **2016,** *27* (1), 3-18.
9. Stevens, M. M.; Flynn, N. T.; Wang, C.; Tirrell, D. A.; Langer, R., Coiled-Coil Peptide-Based Assembly of Gold Nanoparticles. *Adv. Mater.* **2004,** *16* (11), 915-918.
10. Do, T. D.; LaPointe, N. E.; Economou, N. J.; Buratto, S. K.; Feinstein, S. C.; Shea, J.-E.; Bowers, M. T., Effects of pH and Charge State on Peptide Assembly: The YVIFL Model System. *The Journal of Physical Chemistry B* **2013,** *117* (37), 10759-10768.
11. Tu, R. S.; Tirrell, M., Bottom-up design of biomimetic assemblies. *Adv. Drug. Deliv. Rev.* **2004,** *56* (11), 1537-1563.
12. Dennis W. P. M. Lowik, J. C. M. v. H., Ppetide based amphiphiles. *The Royal Society of Chemistry* **2004,** *33*, 234-245.
13. Giddi HS, A. M., Bellare JR., Self-assembled surfactant nano-structures important in drug delivery: a review. *Indian Journal of Experimental Biology* **2007,** *45*, 133-159.
14. Torchilin, V. P., Micellar nanocarriers: pharmaceutical perspectives. *Pharmaceutical Research* **2007,** *24* (1), 1-16.
15. Katarzyna Kita-Tokarczyk, J. G., Thomas Haefele, Wolfgang Meier, Block copolymer vesicles - using concepts from polymer chemistry to mimic biomembranes. *Polymer* **2005,** *11*, 3540-3563.
16. Geourjon, C.; Deléage, G., SOPM: a self-optimized method for protein secondary structure prediction. *Protein Engineering, Design and Selection* **1994,** *7* (2), 157-164.
17. Monica C. Branco, J. P. S., Self-assembling materials for therapeutic delivery. *Acta Biomateriala* **2009**, 817-831.
18. Shah RN, S. N., Lim MMDR, Hsieh C, Nuber G, Stupp SI, Supramolecular design of self-assembling nanofibers for cartilage regeneration. *Proceedings of the National Academy of Sciences U.S.A* **2010,** *107*, 3293-3298.
19. Accardo A, T. D., Mangiapia D, Pedone C, Morelli G, Nanostructures by self-assembly peptide amphiphile as potential selective drug carriers. *J. Pept. Sci.* **2006,** *88*, 115-121.

20. Dehsorkhi, A.; Castelletto, V.; Hamley, I. W., Self-assembling amphiphilic peptides. *J Pept Sci* **2014,** *20* (7), 453-67.
21. Hamley, I. W., Lipopeptides: from self-assembly to bioactivity. *Chem Commun (Camb)* **2015,** *51* (41), 8574-83.
22. Zhang, L.; Bulaj, G., Converting Peptides into Drug Leads by Lipidation. *Curr. Med. Chem.* **2012,** *19* (11), 1602-1618.
23. Zhao, H.; Shao, D.; Jiang, C.; Shi, J.; Li, Q.; Huang, Q.; Rajoka, M. S. R.; Yang, H.; Jin, M., Biological activity of lipopeptides from Bacillus. *Applied microbiology and biotechnology* **2017,** *101* (15), 5951-5960.
24. Mnif, I.; Ghribi, D., Review lipopeptides biosurfactants: Mean classes and new insights for industrial, biomedical, and environmental applications. *Biopolymers* **2015,** *104* (3), 129-47.
25. Singh, P.; Cameotra, S. S., Potential applications of microbial surfactants in biomedical sciences. *Trends in Biotechnology* **2004,** *22* (3), 142-146.
26. Steller, S.; Vollenbroich, D.; Leenders, F.; Stein, T.; Conrad, B.; Hofemeister, J.; Jacques, P.; Thonart, P.; Vater, J., Structural and functional organization of the fengycin synthetase multienzyme system from Bacillus subtilis b213 and A1/3. *Chemistry & biology* **1999,** *6* (1), 31-41.
27. Ohno, A.; Ano, T.; Shoda, M., Production of a lipopeptide antibiotic, surfactin, by recombinant Bacillus subtilis in solid state fermentation. *Biotechnology and Bioengineering* **1995,** *47* (2), 209-214.
28. Heerklotz, H.; Seelig, J., Detergent-like action of the antibiotic peptide surfactin on lipid membranes. *Biophys J* **2001,** *81* (3), 1547-1554.
29. Carrillo, C.; Teruel, J. A.; Aranda, F. J.; Ortiz, A., Molecular mechanism of membrane permeabilization by the peptide antibiotic surfactin. *Biochim Biophys Acta* **2003,** *1611* (1-2), 91-7.
30. Hamley, I. W.; Dehsorkhi, A.; Jauregi, P.; Seitsonen, J.; Ruokolainen, J.; Coutte, F.; Chataigné, G.; Jacques, P., Self-assembly of three bacterially-derived bioactive lipopeptides. *Soft Matter* **2013,** *9* (40), 9572-9578.
31. Nasir, M. N.; Besson, F., Interactions of the antifungal mycosubtilin with ergosterol-containing interfacial monolayers. *Biochim Biophys Acta* **2012,** *1818* (5), 1302-8.
32. Deleu, M.; Paquot, M.; Nylander, T., Effect of fengycin, a lipopeptide produced by Bacillus subtilis, on model biomembranes. *Biophys J* **2008,** *94* (7), 2667-2679.
33. Meena, K. R.; Kanwar, S. S., Lipopeptides as the Antifungal and Antibacterial Agents: Applications in Food Safety and Therapeutics. *BioMed Research International* **2015,** *2015*, 9.
34. Woodworth, J. R.; Nyhart, E. H., Jr.; Brier, G. L.; Wolny, J. D.; Black, H. R., Single-dose pharmacokinetics and antibacterial activity of daptomycin, a new lipopeptide antibiotic, in healthy volunteers. *Antimicrobial agents and chemotherapy* **1992,** *36* (2), 318-325.
35. Baltz, R. H.; Miao, V.; Wrigley, S. K., Natural products to drugs: daptomycin and related lipopeptide antibiotics. *Nat. Prod. Rep.* **2005,** *22* (6), 717-741.
36. Silverman, J. A.; Perlmutter, N. G.; Shapiro, H. M., Correlation of daptomycin bactericidal activity and membrane depolarization in Staphylococcus aureus. *Antimicrobial agents and chemotherapy* **2003,** *47* (8), 2538-2544.

37. Alborn, W. E.; Allen, N. E.; Preston, D. A., Daptomycin disrupts membrane potential in growing Staphylococcus aureus. *Antimicrobial Agents and Chemotherapy* **1991,** *35* (11), 2282-2287.
38. Kirkham, S.; Castelletto, V.; Hamley, I. W.; Inoue, K.; Rambo, R.; Reza, M.; Ruokolainen, J., Self-Assembly of the Cyclic Lipopeptide Daptomycin: Spherical Micelle Formation Does Not Depend on the Presence of Calcium Chloride. *ChemPhysChem* **2016,** *17* (14), 2118-2122.
39. Bruno, B. J.; Miller, G. D.; Lim, C. S., Basics and recent advances in peptide and protein drug delivery. *Therapeutic delivery* **2013,** *4* (11), 1443-1467.
40. Katayama, K.; Armendariz-Borunda, J.; Raghow, R.; Kang, A. H.; Seyer, J. M., A pentapeptide from type I procollagen promotes extracellular matrix production. *J Biol Chem* **1993,** *268* (14), 9941-4.
41. Robinson, L. R.; Fitzgerald, N. C.; Doughty, D. G.; Dawes, N. C.; Berge, C. A.; Bissett, D. L., Topical palmitoyl pentapeptide provides improvement in photoaged human facial skin. *International journal of cosmetic science* **2005,** *27* (3), 155-60.
42. Jones, R. R.; Castelletto, V.; Connon, C. J.; Hamley, I. W., Collagen stimulating effect of peptide amphiphile C16-KTTKS on human fibroblasts. *Mol Pharm* **2013,** *10* (3), 1063-9.
43. Werle, M.; Bernkop-Schnurch, A., Strategies to improve plasma half life time of peptide and protein drugs. *Amino Acids* **2006,** *30* (4), 351-67.
44. Tang, L.; Persky, A. M.; Hochhaus, G.; Meibohm, B., Pharmacokinetic Aspects of Biotechnology Products. *J. Pharm. Sci.* **2004,** *93*, 2184-2204.
45. Tryggvason, K.; Wartiovaara, J., How Does the Kidney Filter Plasma? *Physiology* **2005,** *20*, 96-101.
46. Hamley, I. W., PEG–Peptide Conjugates. *Biomacromolecules* **2014,** *15* (5), 1543-1559.
47. Bellmann-Sickert, K.; Elling, C. E.; Madsen, A. N.; Little, P. B., Analogue of Human Pancreatic Polypeptide is Slowly Released into Circulation. *Med. Chem.* **2011**, 2658-2667.
48. Lee, S. H.; Lee, S.; Youn, Y. S.; Na, D. H.; Chae, S. Y.; Byun, Y.; Lee, K. C., Synthesis, characterization, and pharmacokinetic studies of PEGylated glucagon-like peptide-1. *Bioconjug Chem* **2005,** *16* (2), 377-82.
49. Harris, J. M.; Chess, R. B., Effect of PEGylation on Pharmaceuticals. *Nat. Rev. Drug. Disc.* **2003,** *2*, 214-221.
50. Moradi, S. V.; Hussein, W. M.; Varamini, P.; Simerska, P.; Toth, I., Glycosylation, an effective synthetic strategy to improve the bioavailability of therapeutic peptides. *Chemical science* **2016,** *7* (4), 2492-2500.
51. Zhou, P.; Deng, L.; Wang, Y.; Lu, J. R.; Xu, H., Different nanostructures caused by competition of intra- and inter-beta-sheet interactions in hierarchical self-assembly of short peptides. *J Colloid Interface Sci* **2016,** *464*, 219-28.
52. Houston, M. E., Jr.; Wallace, A.; Bianchi, E.; Pessi, A.; Hodges, R. S., Use of a conformationally restricted secondary structural element to display peptide libraries: a two-stranded alpha-helical coiled-coil stabilized by lactam bridges. *J Mol Biol* **1996,** *262* (2), 270-82.
53. Salamone, S.; Guerreiro, C.; Cambon, E.; André, I.; Remaud-Siméon, M.; Mulard, L. A., Programmed chemo-enzymatic synthesis of the oligosaccharide component of a

carbohydrate-based antibacterial vaccine candidate. *Chem Commun* **2015,** *51* (13), 2581-2584.
54. Fujikawa, K.; Koizumi, A.; Hachisu, M.; Seko, A.; Takeda, Y.; Ito, Y., Construction of a high-mannose-type glycan library by a renewed top-down chemo-enzymatic approach. *Chemistry (Weinheim an der Bergstrasse, Germany)* **2015,** *21* (8), 3224-33.
55. Räder, A. F. B.; Reichart, F.; Weinmüller, M.; Kessler, H., Improving oral bioavailability of cyclic peptides by N-methylation. *Bioorgan Med Chem* **2018,** *26* (10), 2766-2773.
56. Ehrlich, G. K.; Michel, H.; Truitt, T., Preparation and Characterisation of Albumin Conjugates of a Truncated Peptide YY Analogue for Half-Life Extension. *Bioconjugate Chem* **2013**, 2015-2024.
57. Kontermann, R. E., Strategies to Extend Plasma Half-lives of Recombinant antibodies. *Biodrugs* **2009,** *23*, 93-109.
58. Kontermann, R. E., Strategies for Extended Serum Half-life of Protein Therapeutics. *Current Opinion in Biotechnology* **2011,** *22*, 868-876.
59. van Witteloostuijn, S. B.; Pedersen, S. L.; Jensen, K. J., Half-Life Extension of Biopharmaceuticals using Chemical Methods: Alternatives to PEGylation. *ChemMedChem* **2016,** *11* (22), 2474-2495.
60. Arik Makovitzki, J. B., and Yechiel Shai, Antimicrobial Lipopolypeptides Composed of Palmitoyl Di- and Tricationic Peptides: In Vitro and in ViVo Activities, Self-Assembly to Nanostructures, and a Plausible Mode of Action. *Biochem.* **2008,** *47*, 10630-10636.
61. Epand, R. M., Biophysical studies of lipopeptide-membrane interactions. *Biopolymers* **1997,** *43* (1), 15-24.
62. Knudsen, L. B.; Nielsen, P. F.; Huusfeldt, P. O.; Johansen, N. L.; Madsen, K.; Pedersen, F. Z.; Thogersen, H.; Wilken, M.; Agerso, H., Potent Derivatives of Glucagon-Like-Peptide-1 with Pharmacokinetic Properties Suitable for Once Daily Administration. *J. Med. Chem.* **2000,** *43*, 1664-1669.
63. Pan, C. Q.; Buxton, J. M.; Yung, S. L.; Tom, I.; Yang, L.; Chen, H.; MacDougall, M.; Bell, A.; Claus, T. H.; Clairmont, K. B.; Whelan, J. P., Design of a Long Acting Peptide Functioning as Both a Glucagon-like Peptide-1 Receptor Agonist and a Glucagon Receptor Antagonist. *The Journal of Biological Chemistry* **2006,** *281*, 12506-12515.
64. Thorens, B., Expression Cloning of the Pancreatic B cell Receptor for the Gluco-Incretin Hormone Glucagon-like Peptide 1. *P. Natl. Acad. Sci.* **1992,** *89*, 8641-8645.
65. Ahmed, E. M., Hydrogel: Preparation, characterization, and applications: A review. *Journal of Advanced Research* **2015,** *6* (2), 105-121.
66. Dasgupta, A.; Mondal, J. H.; Das, D., Peptide hydrogels. *Rsc Adv* **2013,** *3* (24), 9117-9149.
67. Gulrez, S. K. H.; Al-Assaf, S.; Phillips, G. O., Hydrogels: Methods of Preparation, Characterisation and Applications. In *Progress in Molecular and Environmental Bioengineering - From Analysis and Modeling to Technology Applications*, 2011.
68. Tirrell, L. J. D. D. A., *Peptide and Protein Hydrogels*. The Royal Society of Chemistry. *Monographs in Supramolecular Chemistry,* 2013.
69. Mehrban, N.; Zhu, B.; Tamagnini, F.; Young, F. I.; Wasmuth, A.; Hudson, K. L.; Thomson, A. R.; Birchall, M. A.; Randall, A. D.; Song, B.; Woolfson, D. N., Functionalized

α-Helical Peptide Hydrogels for Neural Tissue Engineering. *ACS Biomaterials Science & Engineering* **2015,** *1* (6), 431-439.
70. Banwell, E. F.; Abelardo, E. S.; Adams, D. J.; Birchall, M. A.; Corrigan, A.; Donald, A. M.; Kirkland, M.; Serpell, L. C.; Butler, M. F.; Woolfson, D. N., Rational design and application of responsive alpha-helical peptide hydrogels. *Nat Mater* **2009,** *8* (7), 596-600.
71. Fichman, G.; Gazit, E., Self-assembly of short peptides to form hydrogels: Design of building blocks, physical properties and technological applications. *Acta Biomaterialia* **2014,** *10* (4), 1671-1682.
72. Jayawarna, V.; Ali, M.; Jowitt, T. A.; Miller, A. F.; Saiani, A.; Gough, J. E.; Ulijn, R. V., Nanostructured Hydrogels for Three-Dimensional Cell Culture Through Self-Assembly of Fluorenylmethoxycarbonyl–Dipeptides. *Adv. Mater.* **2006,** *18* (5), 611-614.
73. Orbach, R.; Adler-Abramovich, L.; Zigerson, S.; Mironi-Harpaz, I.; Seliktar, D.; Gazit, E., Self-Assembled Fmoc-Peptides as a Platform for the Formation of Nanostructures and Hydrogels. *Biomacromolecules* **2009,** *10* (9), 2646-2651.
74. Adams, D. J.; Morris, K.; Chen, L.; Serpell, L. C.; Bacsa, J.; Day, G. M., The delicate balance between gelation and crystallisation: structural and computational investigations. *Soft Matter* **2010,** *6* (17), 4144-4156.
75. Chen, L.; Morris, K.; Laybourn, A.; Elias, D.; Hicks, M. R.; Rodger, A.; Serpell, L.; Adams, D. J., Self-Assembly Mechanism for a Naphthalene−Dipeptide Leading to Hydrogelation. *Langmuir* **2010,** *26* (7), 5232-5242.
76. Adams, D. J.; Mullen, L. M.; Berta, M.; Chen, L.; Frith, W. J., Relationship Between Molecular Structure, Gelation Behaviour and Gel Properties of Fmoc-Dipeptides. *Soft Matter* **2010,** *6* (9), 1971-1980.
77. Morris, K. L.; Chen, L.; Raeburn, J.; Sellick, O. R.; Cotanda, P.; Paul, A.; Griffiths, P. C.; King, S. M.; O'Reilly, R. K.; Serpell, L. C.; Adams, D. J., Chemically programmed self-sorting of gelator networks. *Nature Communications* **2013,** *4*, 1480.
78. Marchesan, S.; Waddington, L.; Easton, C. D.; Winkler, D. A.; Goodall, L.; Forsythe, J.; Hartley, P. G., Unzipping the role of chirality in nanoscale self-assembly of tripeptide hydrogels. *Nanoscale* **2012,** *4* (21), 6752-60.
79. Birchall, L. S.; Roy, S.; Jayawarna, V.; Hughes, M.; Irvine, E.; Okorogheye, G. T.; Saudi, N.; De Santis, E.; Tuttle, T.; Edwards, A. A.; Ulijn, R. V., Exploiting CH-π interactions in supramolecular hydrogels of aromatic carbohydrate amphiphiles. *Chemical Science* **2011,** *2* (7), 1349-1355.
80. Ma, M.; Kuang, Y.; Gao, Y.; Zhang, Y.; Gao, P.; Xu, B., Aromatic-aromatic interactions induce the self-assembly of pentapeptidic derivatives in water to form nanofibers and supramolecular hydrogels. *J Am Chem Soc* **2010,** *132* (8), 2719-28.
81. Siddle, K., *Peptide Hormone Secretion: Peptide Hormone Action*. Oxford University Press, Incorporated: 1991.
82. Neal, J. M., *How the Endocrine System Works*. 2nd ed.; Wiley-Blackwell: 2016.
83. Carabotti, M.; Scirocco, A.; Maselli, M. A.; Severi, C., The gut-brain axis: interactions between enteric microbiota, central and enteric nervous systems. *Annals of gastroenterology* **2015,** *28* (2), 203-209.
84. Konturek, S. J.; Konturek, J. W.; Pawlik, T.; Brzozowski, T., Brain-gut axis and its role in the control of food intake. *Journal of physiology and pharmacology : an official journal of the Polish Physiological Society* **2004,** *55* (1 Pt 2), 137-54.

85. Hans-Rudolf Berthoud, C. M., The Brain, Appetite, and Obesity. *The Annual Review of Psychology* **2008,** *59*, 55-92.
86. Wren, A. M.; Bloom, S. R., Gut Hormones and Appetite Control. *Gastroenterology* **2007,** *132* (6), 2116-2130.
87. Coll, A. P.; Farooqi, I. S.; O'Rahilly, S., The hormonal control of food intake. *Cell* **2007,** *129* (2), 251-62.
88. de Lartigue, G., Role of the vagus nerve in the development and treatment of diet-induced obesity. *The Journal of physiology* **2016,** *594* (20), 5791-5815.
89. Parker, S. L.; Balasubramaniam, A., Neuropeptide Y Y2 receptor in health and disease (vol 153, pg 420, 2007). *Brit J Pharmacol* **2008,** *155* (8), 1307-1307.
90. Bewick, G. A., Bowels control brain: gut hormones and obesity. *Biochemia medica* **2012,** *22* (3), 283-97.
91. Klok, M. D.; Jakobsdottir, S.; Drent, M. L., The role of leptin and ghrelin in the regulation of food intake and body weight in humans: a review. *Obes Rev* **2007,** *8* (1), 21-34.
92. Huda, M. S.; Wilding, J. P.; Pinkney, J. H., Gut peptides and the regulation of appetite. *Obes Rev* **2006,** *7* (2), 163-82.
93. Anini Y, J. C., Chariot J, Nagain C, Oxyntomodulin inhibits pancreatic secretion through the nervous system in rats. *Pancreas* **2000,** *20*, 348-360.
94. Schepp W, D. K., Riedel T, Schmidtler J, Schaffer K, Classen M, Oxyntomodulin: a cAMP-dependant stimulus of rat parietal cell function via the receptor for glucagon-like peptide-1 (7-36)NH2. *Digestion* **1996,** *57*, 398-405.
95. Dakin, C. L.; Gunn, I.; Small, C. J.; Edwards, C. M.; Hay, D. L.; Smith, D. M.; Ghatei, M. A.; Bloom, S. R., Oxyntomodulin inhibits food intake in the rat. *Endocrinology* **2001,** *142* (10), 4244-50.
96. Schjoldager, B.; Mortensen, P. E.; Myhre, J.; Christiansen, J.; Holst, J. J., Oxyntomodulin from distal gut. Role in regulation of gastric and pancreatic functions. *Dig Dis Sci* **1989,** *34* (9), 1411-9.
97. Holst, J. J., The physiology of glucagon-like peptide 1. *Physiol Rev* **2007,** *87* (4), 1409-39.
98. Drucker, D. J.; Nauck, M. A., The incretin system: glucagon-like peptide-1 receptor agonists and dipeptidyl peptidase-4 inhibitors in type 2 diabetes. *Lancet* **2006,** *368* (9548), 1696-1705.
99. Drucker, D. J., The biology of incretin hormones. *Cell Metab* **2006,** *3* (3), 153-65.
100. Drucker, D. J., Minireview: the glucagon-like peptides. *Endocrinology* **2001,** *142* (2), 521-7.
101. Anders G. Blomqvist, H. H., Y-receptor subtypes - how many more? *Trends in Neuroscience* **1997**, 294-298.
102. Hutchinson, J. A.; Burholt, S.; Hamley, I. W., Peptide Hormones and Lipopeptides: From Self-Assembly to Therapeutic Applications. *J. Pept. Sci.* **2017,** *23*, 82-94.
103. Katsuura, G.; Asakawa, A.; Inui, A., Roles of pancreatic polypeptide in regulation of food intake. *Peptides* **2002,** *23* (2), 323-9.
104. Adrian, T. E.; Besterman, H. S.; Cooke, T. J.; Bloom, S. R.; Bames, A. J.; Russell, R. C., Mechanism of pancreatic polypeptide release in man. *Lancet* **1997,** *1*, 161-163.
105. RI, H., The pancreatic polypeptide (PP-fold) family: gastrointestinal, vascular, and feeding behavioural implication. *Experimental biology and medicine* **1993,** *203*, 44-63.

106. McTigue, D. M.; Rogers, R. C., Pancreatic polypeptide stimulates gastric motility through a vagal-dependant mechanism in rats. *Neurosci Lett* **1995,** *188*, 93-96.
107. Tatemoto, K., Isolation and Characterization of Peptide YY (PYY), a Candidate Gut Hormone That Inhibits Pancreatic Exocrine Secretion. *P. Natl. Acad. Sci. Biol. Sci.* **1982,** *79* (8), 2514-2518.
108. Ehrlich, G. K.; Michel, H.; Truitt, T.; Riboulet, W.; Pop-Damkov, P.; Goelzer, P.; Hainzl, D.; Qureshi, F.; Lueckel, B.; Danho, W.; Conde-Knape, K.; Konkar, A., Preparation and characterization of albumin conjugates of a truncated peptide YY analogue for half-life extension. *Bioconjug Chem* **2013,** *24* (12), 2015-24.
109. Nygaard, R.; Nielbo, S.; Schwartz, T. W.; Poulsen, F. M., The PP-Fold Solution Structure of Human Polypeptide YY and Human PYY_{3-36} as Determined by NMR. *Biochem.* **2006,** *45* (27), 8350-7.
110. Albertsen, L.; Andersen, J. J.; Paulsson, J. F.; Thomsen, J. K.; Norrild, J. C.; Stromgaard, K., Design and Synthesis of Peptide YY Analogues with C-terminal Backbone Amide-to-Ester Modifications. *Acs Medicinal Chemistry Letters* **2013,** *4* (12), 1228-1232.
111. Keire, D. A.; Bowers, C. W.; Solomon, T. E.; Reeve, J. R., Jr., Structure and receptor binding of PYY analogs. *Peptides* **2002,** *23* (2), 305-21.
112. Michel, M. C.; Beck-Sickinger, A.; Cox, H.; Doods, H. N.; Herzog, H.; Larhammar, D.; Quirion, R.; Schwartz, T.; Westfall, T., XVI. International Union of Pharmacology recommendations for the nomenclature of neuropeptide Y, peptide YY, and pancreatic polypeptide receptors. *Pharmacol Rev* **1998,** *50* (1), 143-50.
113. Chronwall, B. M.; DiMaggio, D. A.; Massari, V. J.; Pickel, V. M.; Ruggiero, D. A.; O'Donohue, T. L., The anatomy of neuropeptide-Y-containing neurons in rat brain. *Neuroscience* **1985,** *15* (4), 1159-81.
114. Dumont, Y.; Fournier, A.; Quirion, R., Expression and characterization of the neuropeptide Y Y5 receptor subtype in the rat brain. *Neuroscience* **1998,** *18*, 5565-5574.
115. Larhammar, D., Structural diversity of receptors for neuropeptide Y, peptide YY and pancreatic polypeptide. *Regul Peptides* **1996,** *65*, 165-174.
116. Wahlestedt, C.; Reis, D. J., Neuropeptide Y-related peptides and their receptors are the receptors potential therapeutic drug targets? *Annual Review of Pharmacology and Toxicology* **1993,** *32*, 309-352.
117. Craik, D. J.; Fairlie, D. P.; Liras, S.; Price, D., The Future of Peptide-based Drugs. *Chemical Biology & Drug Design* **2013,** *81* (1), 136-147.
118. Grant, M.; Leone-Bay, A., Peptide therapeutics: it's all in the delivery. *Ther Deliv* **2012,** *3* (8), 981-96.
119. Webber, M. J.; Berns, E. J.; Stupp, S. I., Supramolecular Nanofibers of Peptide Amphiphiles for Medicine. *Isr J Chem* **2013,** *53* (8), 530-554.
120. Li, Y.; Shao, M. X.; Zheng, X. M.; Kong, W. L.; Zhang, J. N.; Gong, M., Self-Assembling Peptides Improve the Stability of Glucagon-like Peptide-1 by Forming a Stable and Sustained Complex. *Mol. Pharm.* **2013,** *10* (9), 3356-3365.
121. Gao, Z.; Bai, G.; Chen, J.; Zhang, Q.; Pan, P.; Bai, F.; Geng, P., Development, characterization, and evaluation of a fusion protein of a novel glucagon-like peptide-1 (GLP-1) analog and human serum albumin in Pichia pastoris. *Bioscience, biotechnology, and biochemistry* **2009,** *73* (3), 688-94.
122. Wang, Y.; Lomakin, A.; Kanai, S.; Alex, R.; Benedek, G. B., Transformation of Oligomers of Lipidated Peptide Induced by Change in pH. *Mol. Pharm.* **2015,** *12* (2), 411-419.

123. Frederiksen, T. M.; Sonderby, P.; Ryberg, L. A.; Harris, P.; Bukrinski, J. T.; Scharff-Poulsen, A. M.; Elf-Lind, M. N.; Peters, G. H., Oligomerization of a Glucagon-like Peptide 1 Analog: Bridging Experiment and Simulations. *Biophys J* **2015,** *109* (6), 1202-1213.
124. Valery, C.; Artzner, F.; Robert, B.; Gulick, T.; Keller, G.; Grabielle-Madelmont, C.; Torres, M. L.; Cherif-Cheik, R.; Paternostre, M., Self-association process of a peptide in solution: From beta-sheet filaments to large embedded nanotubes. *Biophys J* **2004,** *86* (4), 2484-2501.
125. Gobeaux, F.; Fay, N.; Tarabout, C.; Meneau, F.; Meriadec, C.; Delvaux, C.; Cintrat, J. C.; Valery, C.; Artzner, F.; Paternostre, M., Experimental Observation of Double-Walled Peptide Nanotubes and Monodispersity Modeling of the Number of Walls. *Langmuir* **2013,** *29* (8), 2739-2745.
126. Nespovitaya, N.; Gath, J.; Barylyuk, K.; Seuring, C.; Meier, B. H.; Riek, R., Dynamic Assembly and Disassembly of Functional β-Endorphin Amyloid Fibrils. *J. Am. Chem. Soc.* **2016,** *138* (3), 846-856.
127. Glombik, M. M.; Gerdes, H.-H., Signal-mediated sorting of neuropeptides and prohormones:Secretory granule biogenesis revisited. *Biochimie* **2000,** *82* (4), 315-326.
128. Kolodny, S.; Ford, C.; Grinspan, A.; Acetate, U. O.-L. G., Twenty Years of Continuous Treatment of Multiple Sclerosis with Glatiramer Acetate 20 mg/mL Daily: Long-Term Disability Outcomes in the US Open-Label Extension Study. *Mult Scler J* **2016,** *22* (3), 417-417.
129. Mohammadi, F.; Rahimian, R.; Fakhraei, N.; Rezayat, S. M.; Javadi-Paydar, M.; Dehpour, A. R.; Afshari, K.; Mehr, S. E., Effect of glatiramer acetate on short-term memory impairment induced by lipopolysaccharide in male mice. *Fund Clin Pharmacol* **2016,** *30* (4), 347-356.
130. Guzman-Soto, I.; Salinas, E.; Quintanar, J. L., Leuprolide Acetate Inhibits Spinal Cord Inflammatory Response in Experimental Autoimmune Encephalomyelitis by Suppressing NF-kappa B Activation. *Neuroimmunomodulat* **2016,** *23* (1), 33-40.
131. Rahimi, M.; Mobedi, H.; Behnamghader, A., Aqueous stability of leuprolide acetate: effect of temperature, dissolved oxygen, pH and complexation with beta-cyclodextrin. *Pharm Dev Technol* **2016,** *21* (1), 108-115.
132. Candeias, E. M.; Sebastiao, I. C.; Cardoso, S. M.; Correia, S. C.; Carvalho, C. I.; Placido, A. I.; Santos, M. S.; Oliveira, C. R.; Moreira, P. I.; Duarte, A. I., Gut-brain connection: The neuroprotective effects of the anti-diabetic drug liraglutide. *World J Diabetes* **2015,** *6* (6), 807-827.
133. Rai, Y.; Iwata, H.; Masuda, N.; Anan, K.; Takeuchi, T.; Kohno, N.; Takei, H.; Yanagita, Y.; Noguchi, S., Monthly versus three-monthly goserelin treatment in premenopausal patients with oestrogen receptor-positive early breast cancer. *Ejc Suppl* **2010,** *8* (3), 193-193.
134. Sagara, Y.; Masuda, N.; Kinoshita, T.; Iwata, H.; Nakamura, S.; Yanagita, Y.; Nishimura, R.; Iwase, H.; Kamigaki, S.; Takei, H.; Noguchi, S., The STAGE Study: A Phase III Comparison of Anastrozole Plus Goserelin with Tamoxifen Plus Goserelin as Pre-Operative Treatments in Premenopausal Breast Cancer Patients. *Cancer Res* **2010,** *70*.
135. Gadelha, M. R.; Bronstein, M. D.; Brue, T.; Coculescu, M.; Fleseriu, M.; Guitelman, M.; Pronin, V.; Raverot, G.; Shimon, I.; Lievre, K. K.; Fleck, J.; Aout, M.; Pedroncelli, A. M.; Colao, A.; Grp, P. C. S., Pasireotide versus continued treatment with octreotide or lanreotide in patients with inadequately controlled acromegaly (PAOLA): a randomised, phase 3 trial. *Lancet Diabetes Endo* **2014,** *2* (11), 875-884.

136. Giustina, A.; Karamouzis, I.; Patelli, I.; Mazziotti, G., Octreotide for acromegaly treatment: a reappraisal. *Expert Opin Pharmaco* **2013,** *14* (17), 2433-2447.
137. Chambers, E. E.; Lame, M. E.; Bardsley, J.; Hannam, S.; Legido-Quigley, C.; Smith, N.; Fountain, K. J.; Collins, E.; Thomas, E., High sensitivity LC-MS/MS method for direct quantification of human parathyroid 1-34 (teriparatide) in human plasma. *Journal of Chromatography B-Analytical Technologies in the Biomedical and Life Sciences* **2013,** *938*, 96-104.
138. Gatti, D.; Rossini, M.; Viapiana, O.; Povino, M. R.; Liuzza, S.; Fracassi, E.; Idolazzi, L.; Adami, S., Teriparatide Treatment in Adult Patients with Osteogenesis Imperfecta Type I. *Calcified Tissue Int* **2013,** *93* (5), 448-452.
139. Fan, H.; Pan, Q. R.; Xu, Y.; Yang, X. C., Exenatide improves type 2 diabetes concomitant with non-alcoholic fatty liver disease. *Arq Bras Endocrinol* **2013,** *57* (9), 702-708.
140. Qi, F.; Wu, J.; Fan, Q. Z.; He, F.; Tian, G. F.; Yang, T. Y.; Ma, G. H.; Su, Z. G., Preparation of uniform-sized exenatide-loaded PLGA microspheres as long-effective release system with high encapsulation efficiency and bio-stability. *Colloid Surface B* **2013,** *112*, 492-498.
141. Chang, Y. H.; Chen, W. C.; Hsieh, P. H.; Chen, D. W.; Lee, M. S.; Shih, H. N.; Ueng, S. W. N., In Vitro Activities of Daptomycin-, Vancomycin-, and Teicoplanin-Loaded Polymethylmethacrylate against Methicillin-Susceptible, Methicillin-Resistant, and Vancomycin-Intermediate Strains of Staphylococcus aureus. *Antimicrobial Agents and Chemotherapy* **2011,** *55* (12), 5480-5484.
142. Larioza, J.; Girard, A.; Brown, R. B., Clinical Experience With Daptomycin for Outpatient Parenteral Antibiotic Therapy. *Am J Med Sci* **2011,** *342* (6), 486-488.
143. Kireev, K. A.; Krasnopeev, A. V.; Kireeva, T. S., Clinical case history of eptifibatide use during coronary intervention in patient with coronary failure. *Ration Pharmacother* **2015,** *11* (2), 159-164.
144. Pancioli, A. M.; Adeoye, O.; Schmit, P. A.; Khoury, J.; Levine, S. R.; Tomsick, T. A.; Sucharew, H.; Brooks, C. E.; Crocco, T. J.; Gutmann, L.; Hemmen, T. M.; Kasner, S. E.; Kleindorfer, D.; Knight, W. A.; Martini, S.; McKinney, J. S.; Meurer, W. J.; Meyer, B. C.; Schneider, A.; Scott, P. A.; Starkman, S.; Warach, S.; Broderick, J. P.; Investigators, C.-E., Combined Approach to Lysis Utilizing Eptifibatide and Recombinant Tissue Plasminogen Activator in Acute Ischemic Stroke-Enhanced Regimen Stroke Trial. *Stroke* **2013,** *44* (9), 2381-2387.
145. Scatena, R., Bivalirudin: a new generation antithrombotic drug. *Expert Opin Inv Drug* **2000,** *9* (5), 1119-1127.
146. Yamada, T.; Kurihara, K.; Ohnishi, Y.; Tamada, T.; Tomoyori, K.; Masumi, K.; Tanaka, I.; Kuroki, R.; Niimura, N., Neutron and X-ray crystallographic analysis of the human alpha-thrombin-bivalirudin complex at pD 5.0: Protonation states and hydration structure of the enzyme-product complex. *Bba-Proteins Proteom* **2013,** *1834* (8), 1532-1538.
147. Cope, S. M.; Sizemore, S. M.; Roy, A.; Ghirlanda, G.; Vaiana, S. M., Structure and Internal Dynamics of Calcitonin Family Peptides: Implications for Amyloid Formation. *Biophys J* **2014,** *106* (2), 687a-687a.
148. Deftos, L. J.; Nolan, J. J.; Seely, B. L.; Clopton, P. C.; Cote, G. J.; Whitham, C. L.; Florek, L. J.; Christensen, T. A.; Hill, M. R., Intrapulmonary drug delivery of bone-active

peptides: Bioactivity of inhaled calcitonin approximates injected calcitonin. *J Bone Miner Res* **1996,** *11*, 4-4.
149. Karsdal, M. A.; Henriksen, K.; Arnold, M.; Christiansen, C., Calcitonin - A drug of the past or for the future? Physiologic inhibition of bone resorption while sustaining osteoclast numbers improves bone quality. *Biodrugs* **2008,** *22* (3), 137-144.
150. Caplin, M. E.; Pavel, M.; Cwikla, J. B.; Phan, A. T.; Raderer, M.; Sedlackova, E.; Cadiot, G.; Wolin, E. M.; Capdevila, J.; Wall, L.; Rindi, G.; Langley, A.; Martinez, S.; Gomez-Panzani, E.; Ruszniewski, P.; Investigators, C., Anti-tumour effects of lanreotide for pancreatic and intestinal neuroendocrine tumours: the CLARINET open-label extension study. *Endocr-Relat Cancer* **2016,** *23* (3), 191-199.
151. Sun, L. C.; Yu, C. Y.; Mackey, L. V.; Coy, D. H., Lanreotide and its Potential Applications in Polycystic Kidney and Liver Diseases. *Curr Top Med Chem* **2016,** *16* (2), 133-140.
152. Greenfield, N. J., Using circular dichroism spectra to estimate protein secondary structure. *Nat Protoc* **2006,** *1*, 2876-2890.
153. Lleres, D.; Swift, S.; Lamond, A. I., Detecting protein-protein interactions in vivo with FRET using multiphoton fluorescence lifetime imaging microscopy (FLIM). *Current protocols in cytometry* **2007,** *Chapter 12*, Unit12.10.
154. Rose, H. H., Optics of high-performance electron microscopes. *Science and technology of advanced materials* **2016,** *9* (1), 014107-014107.
155. Kohl, H. R., Ludwig, *Transmission Electron Microscopy : Physics of Image Formation*. 2008.
156. Rice, S. A., Small angle scattering of X-rays. A. Guinier and G. Fournet. Translated by C. B. Wilson and with a bibliographical appendix by K. L. Yudowitch. Wiley, New York, 1955. 268 pp. *Journal of Polymer Science* **1956,** *19* (93), 594-594.
157. Hubbell, J. H., Relativistic atomic form factors and photon coherent scattering cross sections. *Journal of Physical and Chemical Reference Data* **1979,** *8* (1), 69-106.
158. Nyman, M.; McQuade, L., Small Angle X-ray Scattering of Group V Polyoxometalates. 2015; pp 151-170.
159. Li, T.; Senesi, A. J.; Lee, B., Small Angle X-ray Scattering for Nanoparticle Research. *Chem Rev* **2016,** *116* (18), 11128-11180.
160. Jauncey, G. E., The Scattering of X-Rays and Bragg's Law. *P. Natl. Acad. Sci.* **1924,** *10* (2), 57-60.
161. Castelletto, V.; Hamley, I. W., Self assembly of a model amphiphilic phenylalanine peptide/polyethylene glycol block copolymer in aqueous solution. *Biophysical chemistry* **2009,** *141* (2-3), 169-74.
162. Sunde, M.; Blake, C., The Structure of Amyloid Fibrils by Electron Microscopy and X-Ray Diffraction. In *Advances in Protein Chemistry*, Richards, F. M.; Eisenberg, D. S.; Kim, P. S., Eds. Academic Press: 1997; Vol. 50, pp 123-159.
163. Morris, K. L.; Serpell, L. C., X-ray fibre diffraction studies of amyloid fibrils. *Methods Mol Biol* **2012,** *849*, 121-35.

Chapter 2 - Effect of Lipidation and Position of Lipidation on the Self-Assembly of the Gastrointestinal Peptide Hormone PYY_{3-36}

2.1 Introduction

Peptide YY (PYY) is a gut hormone released by the L-cells in the gastrointestinal tract following food intake. There are two endogenous forms: PYY_{1-36}, and PYY_{3-36}, with the latter having a high selectivity for the Y2 G-coupled protein receptors, associated with reduced food intake via the vagal inhibitory loop.[1] The vagus nerve plays an important role in controlling metabolism, by communicating with the gut via cell-signalling to understand its nutritional status. This allows the stimulation or inhibition of food intake depending on the feeding status. Unfortunately, the sensitivity of this mechanism is reduced when chronic calorie overload occurs, which helps to drive obesity.[2] Studies of PYY_{3-36} in humans and mice have shown it to significantly reduce calorific intake.[3-6] This makes PYY_{3-36} an attractive agent for the treatment of obesity and type II diabetes. One major downfall is its short half-life of around 9 minutes, due to rapid clearance from circulation as a result of low molecular weight.[7] Peptide lipidation to overcome this issue would allow the peptide to non-covalently bind to serum albumin, increasing the molecular weight substantially, protecting the whole complex from proteolytic degradation.[8]

Previous self-assembly studies of PYY_{3-36} have shown it to adopt a predominant α-helical secondary structure.[9] Here, we use a range of spectroscopic, scattering, and microscopy techniques to further investigate the self-assembly of PYY_{3-36}, and how lipidation

impacts the self-assembly. Three lipidated derivatives of PYY_{3-36} and the peptide itself were examined, to determine whether lipidation has an impact on the self-assembly and aggregation, as a result of the increased amphiphilicity caused by lipidation. Palmitoyl chains were covalently attached to the peptides, by substitution of γ-L-glutamoyl(Nα-hexadecanoyl) lysine residues at position 11 (PYY11), 17 (PYY17), or 23 (PYY23) as shown in Figure 2.1. Unlipidated PYY_{3-36} was characterized using the same techniques, and shown for comparison (Figure 2.2). Characterisation of PYY17 in solution was carried out by PhD student Sam Burholt (University of Reading), but results are included here to allow a full comparison between lipidation points.

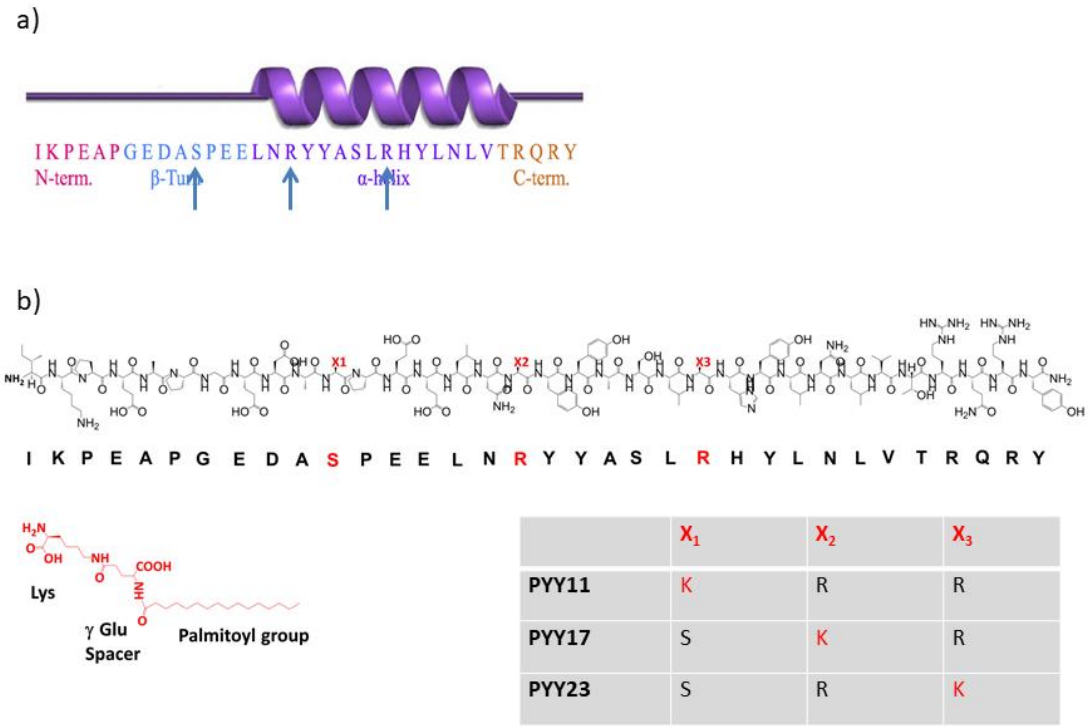

	X_1	X_2	X_3
PYY11	K	R	R
PYY17	S	K	R
PYY23	S	R	K

Figure 2.1. a) Sequence and structure of PYY $_{3\text{-}36}$ with the positions of lipidation shown by the arrows.[10] b) Scheme of PYY $_{3\text{-}36}$ showing the three lipidation positions, 11 (PYY11), 17 (PYY17), and 23 (PYY23). At each lipidation position, the amino acid present (Ser or Arg) is replaced with a lysine derivative in which the alkyl chain is attached via a γ –L-glutamic acid spacer.

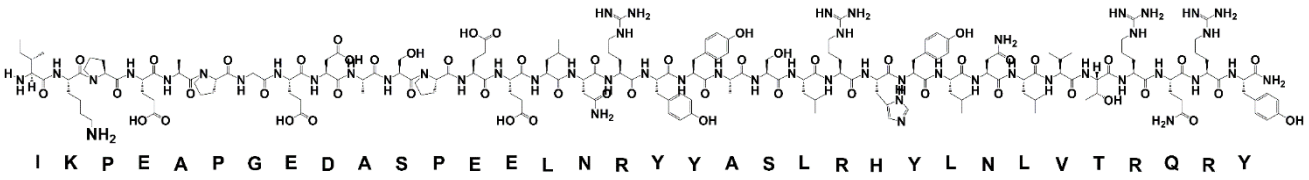

Figure 2.2. Scheme of PYY $_{3\text{-}36}$.

2.2 Results and Discussion

2.2.1 Solution studies

Fluorescence assays using pyrene and Thioflavin T (ThT) as the fluorescent probes, were carried out to investigate the presence of a critical aggregation concentration (cac). Pyrene is a fluorophore that is sensitive to the local hydrophobic environment, [11] and has been successfully used previously to determine the cac of peptides and peptide amphiphiles.[12-13] In the presence of micelles and other macromolecular systems, it becomes encapsulated in the interior regions of the aggregates.[11] This allows the cac to be determined, because upon aggregation, hydrophobic sites are formed that interact with the fluorescent probes. As a result there is a distinct break in intensity of fluorescence which defines the cac. ThT is selective towards amyloid fibril structures,[14-15] and upon binding, there is a distinct increase in fluorescence intensity, similar to pyrene.[16] The exact binding mechanism of ThT is not yet fully understood, but it is thought that amyloid fibrils provide a ThT binding site that sterically traps the bound dye, leading to an increase in fluorescence.[17]

Pyrene was used to determine the cac of the three lipidated peptides, and it was calculated by measuring the fluorescence intensity of the I_1 (λ= 373 nm) peak, corresponding to the first vibronic band of pyrene. A plot of I_1 (373 nm) intensity with concentration is presented in Figure 2.3 to show the cac of all three peptides at native pH in ultrapure water (pH 4). The native pH is defined as the pH of the solution when the peptide is dissolved in ultrapure water. The fluorescence intensity shows breaks at 0.013, 0.015, and 0.0091 wt % (± 0.005 wt %), indicating these as the cac values for PYY11, PYY17, and PYY23 respectively. The pH dependence of the cac was also

investigated using pyrene. Plots of I_1/I_3 [I (373 nm)/I (383 nm)] corresponding to the ratio of the intensities of the first to third vibronic bands of pyrene are shown in Figure 2.4, as well as plots of I_1 (373 nm). Plots of I_1/I_3 for PYY11 were not well-defined throughout the pH range studied, or for PYY23 at pH 2. As a result, only plots of I_1 (373 nm) for PYY11 in the pH range 2-8, and PYY23 at pH 2 are shown to define the cac values (Figure 2.4). From previous studies using other fluorescent probes to compare to pyrene, the concentration dependence of I_1 provides a reliable assay for cac values.[12-13, 18] Results indicate that the cac values are lower for the peptide solutions at native pH compared to pH 2 and 8, suggesting a decrease in hydrophobicity when the pH is altered from the native pH. Table 2.1 summarises the cac values of all 3 peptides as a function of pH.

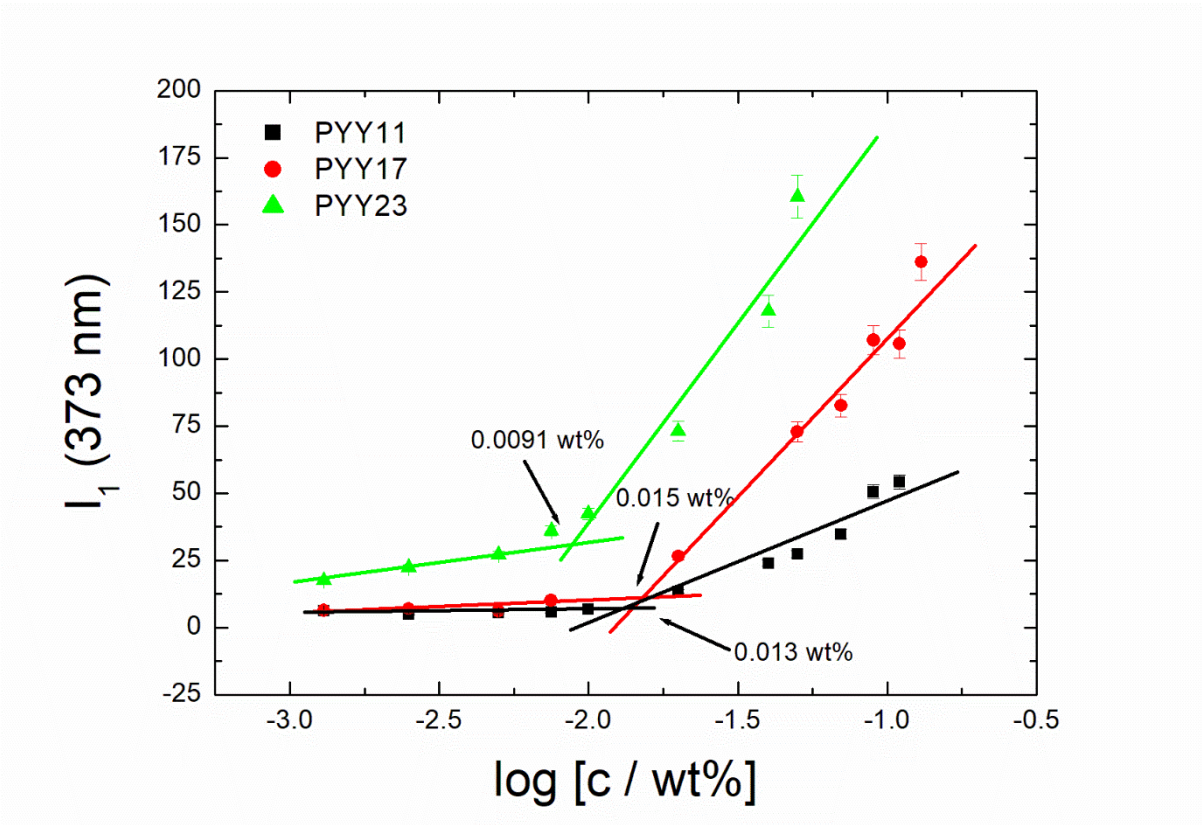

Figure 2.3. Pyrene fluorescence intensity of I 1(373 nm) as a function of concentration, for PYY11, PYY17, and PYY23 at native pH (pH 4). The intersections of the lines defines the cac.

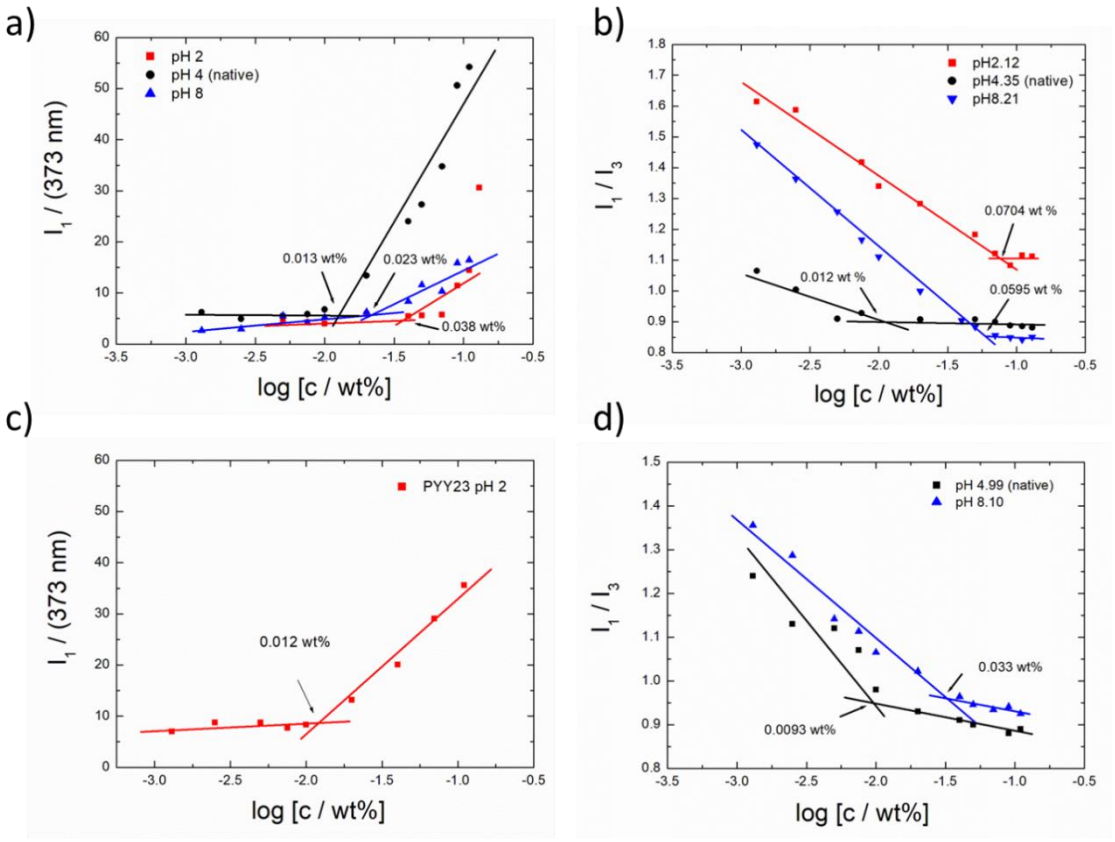

Figure 2.4. Concentration dependence of pyrene fluorescence of PYY11, PYY17, and PYY23 in the pH range 2-8 to determine the cac. The intersections of the lines defines the cac. a) I_1(373 nm) as a function of concentration, for PYY11 in the range pH 2-8. b) I_1/I_3 as a function of concentration, for PYY17 in the pH range 2-8 (vibronic band = I(373 nm)/I(383 nm)). c) I_1 (373 nm) as a function of concentration, for PYY23 at pH 2. d) I_1/I_3 as a function of concentration, for PYY23 at pH 4 and 8.

Table 2.1. Cac values of PYY11, PYY17, and PYY23 in the pH range 2-8 at 20 °C.

	pH 2 (wt%)	pH 4 (native pH) (wt%)	pH 8 (wt%)
PYY11	0.0038	0.013	0.023
PYY17	0.0704	0.012	0.0595
PYY23	0.012	0.0093	0.033

Fluorescence using Thioflavin T (ThT) as the probe was used for PYY_{3-36}, since pyrene proved to be unsuccessful in defining a cac. This could be due to the peptide not having enough hydrophobic sites for pyrene to bind to. The distinct breaks in intensity to define the cac values occur at 0.046 wt% and 0.022 wt% for pH 6, and pH 8 respectively (Figure 2.5). No cac was observed for PYY_{3-36} at pH 2, suggesting a lack of amyloid formation at low pH. This indicates that the unlipidated peptide is not stable to changes in pH when compared to the lipidated peptides.

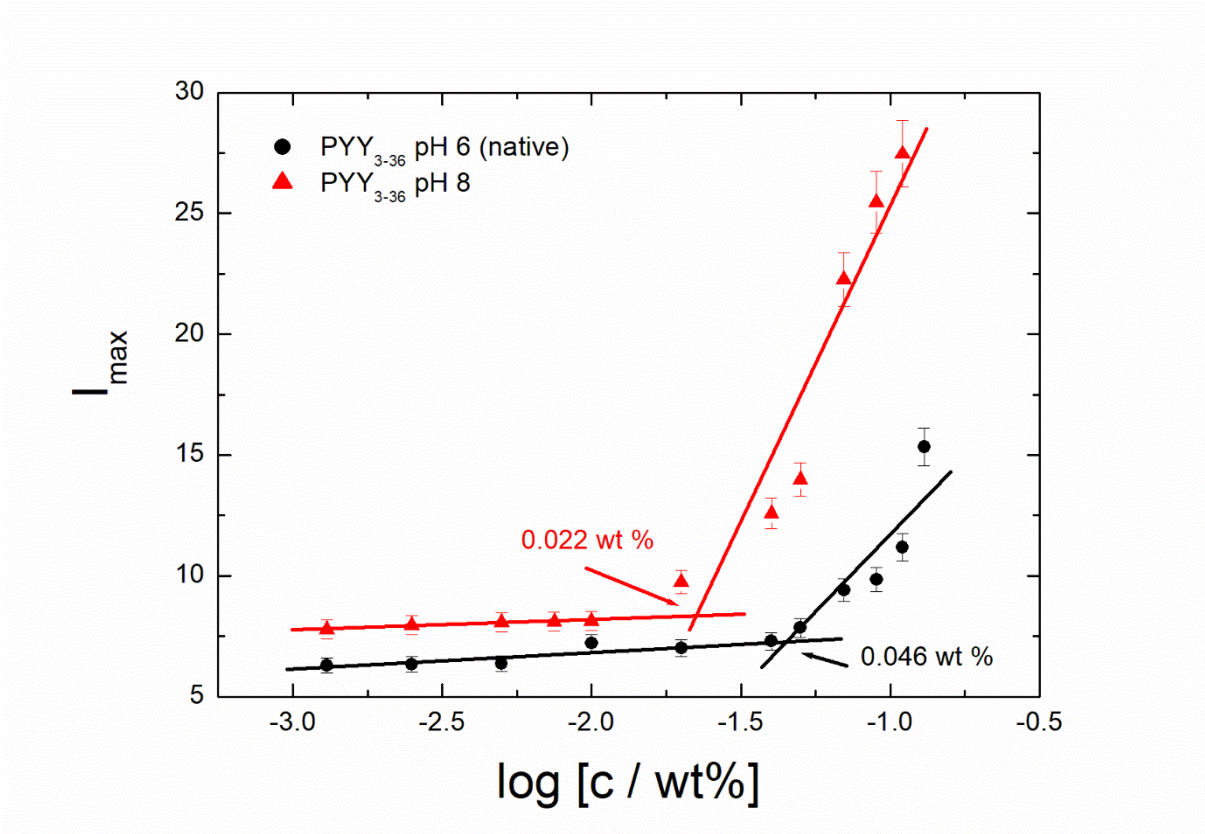

Figure 2.5. Thioflavin T fluorescence intensity of I max (488 nm) as a function of concentration of PYY_{3-36} at pH 6 (native pH) and pH 8 to define the cac.

Titrations were carried out to determine the isoelectric point (pI) of each peptide because calculated values were significantly different from the point at which precipitation was observed. Precipitation occurred at around pH 6 for the lipidated

peptides, therefore this was tentatively associated with experimental pI. Experiments were carried out using 2 wt% peptide solutions and the starting pH was pH 10, following the addition of NaOH. The pH was plotted as a function of added volumes of HCl, where HCl was added dropwise. The plot indicates that the pH shows an initial sharp decrease with a plateau at around pH 5, close to the pH at which precipitation occurred. This is associated with an effective pI (Figure 2.6). The exact isoelectric point of each peptide was not able to be measured from the titration graph due to the range of pKa values of the residues within the peptide sequences.

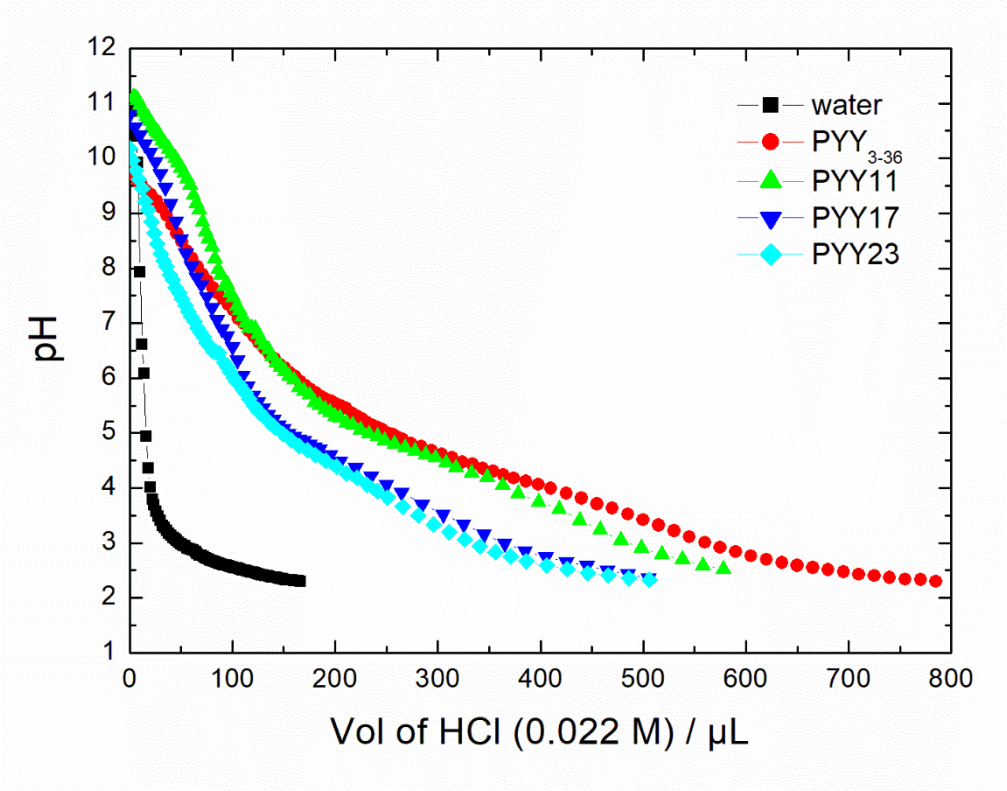

Figure 2.6. pH titrations using HCl to show pKa transitions.

It is known that the pKa values of ionisable groups in proteins can vary substantially from their expected values when in the folded state. This depends on three main environmental factors; The Born Effect (dehydration), Coulombic interactions (charge-

charge interactions), and hydrogen bonding.[19-20] The Born effect allows for pKa values of Asp, Glu, Cys, and Tyr to increase, and those of His, Lys, and Arg to decrease if they are buried within a folded protein. This is due to it being energetically unfavourable to transfer a charged group from water to the interior of a protein where the dielectric constant is lower. Coulombic interactions follow Coulomb's law where an energy minimum is reached depending on the distance between charges. This can result in amino acids becoming polarized, and cause pKa values to change. Hydrogen bonding affects pKa depending on whether the hydrogen bonding interactions are more favourable in the protonated or deprotonated state. For the former, the pKa values will increase, and for the latter they will decrease. All three of these environmental factors can cause pKa values to change by several units.[21] An experiment to look at pKa shifts of lysine residues within SNase with pH change was carried out by Isom et al, and they remarkably found that the values were lowered by more than 5 units, some of the largest shifts in pKa ever measured.[20]

Zeta potential measurements were also carried out to further investigate the particle charge with varied pH. Studies were performed in the pH range 2-4, and results indicated a positive charge on all 3 lipidated peptides under these conditions (Table 2.2).

Table 2.2. Zeta potential values of PYY11, PYY17 and PYY23, at pH 2 and 4.

Sample	pH	Zeta Potential (mV)	Mobility (µm cm/V s)	Conductivity (mS/cm)
PYY11	2	44.43	3.48	1.93
PYY11	4	33.57	2.63	0.065
PYY17	2	42.63	3.34	1.91
PYY17	4	16.47	1.29	0.053
PYY23	2	41.10	3.22	4.89
PYY23	4	20.00	1.57	0.031

The secondary structures of PYY_{3-36}, PYY11, PYY17, and PYY23 were examined using circular dichroism (CD) spectroscopy well above the cac values. Temperature ramp experiments were carried out at pH 2, 4, 6, and 8 from 20 to 70 °C. Figures 2.7-2.8 show CD spectra of all peptides in the pH range 2−8 at 20 °C and 70 °C. The spectra at 20 °C for all samples studied show two minima near 222 and 208 nm, and these features are typical of α-helical secondary structure, and are consistent with coiled coil formation.[22-24] When increasing the temperature to 70 °C, there appears to be a transition into β-sheet above 50 °C for PYY17 and PYY23 at pH 8, with a minimum near 217 nm, characteristic of β-sheet secondary structures (Figure 2.9).[22-24] This transition could be related to the lower theoretical isoelectric point for PYY17 and PYY23 compared to PYY11 and PYY_{3-36}. At pH 8, PYY17 and PYY23 are expected to have a charge of +2, and PYY11 and PYY_{3-36} are expected to have a charge of +3, meaning that there are only weak interactions to overcome in order to aggregate, and that hydrogen bonding can more readily overcome the electrostatic interactions to form a β-sheet structure.[25] Interestingly, PYY11 does not undergo this transition, which suggests that the position of lipidation causes a difference in the stability of the secondary structures. It seems that lipidating the peptide outside of the α-helical region of the molecule reduces the tendency for β-sheet formation at high pH. PYY_{3-36} does not undergo this transition either, suggesting that the increased amphiphilicity of the lipidated peptides PYY17 and PYY23 influences the secondary structure, at higher pH. The lower stability of PYY_{3-36} to temperature changes is also shown by the significant decrease in molar ellipticity upon heating (Figure 2.10).

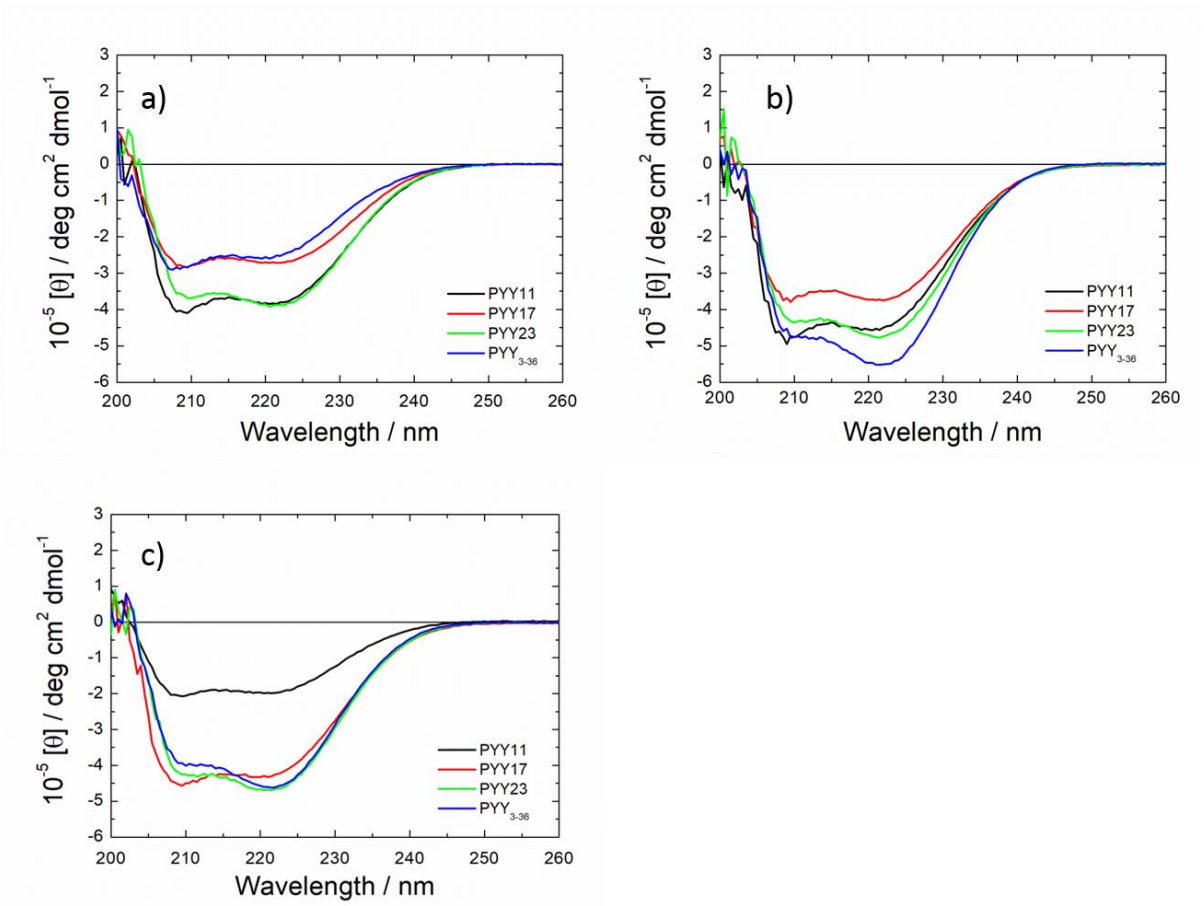

Figure 2.7. CD spectra of 0.5 wt% solutions of PYY11, PYY17, PYY23, and PYY_{3-36} at 20 °C. a) pH 2, b) native pH (pH 4 for lipidated peptides, and pH 6 for unlipidated peptide), c) pH 8.

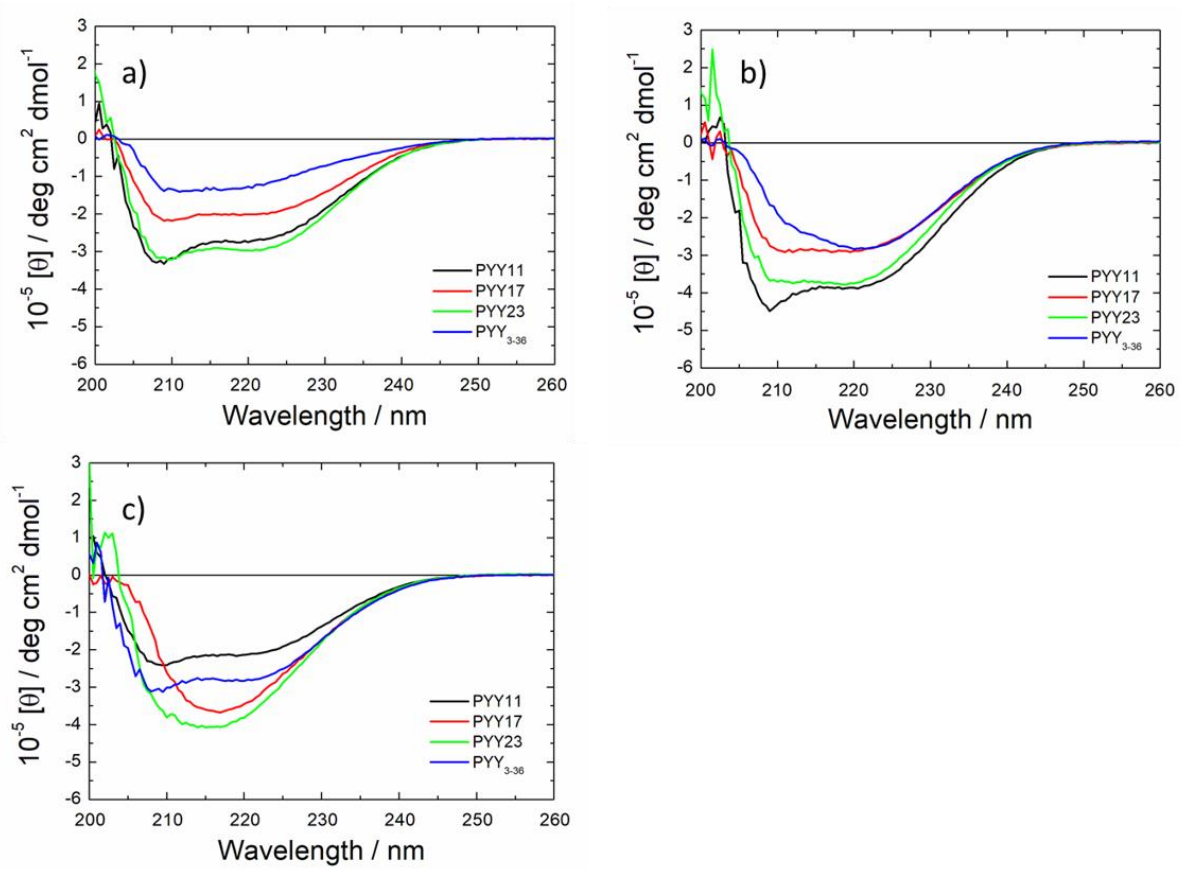

Figure 2.8. CD spectra from 0.5 wt% solutions of PYY11, PYY17, PYY23, and PYY_{3-36} at 70 °C. a) pH 2, b) native pH (pH 4 for lipidated peptides, and pH 6 for unlipidated peptide), c) pH 8.

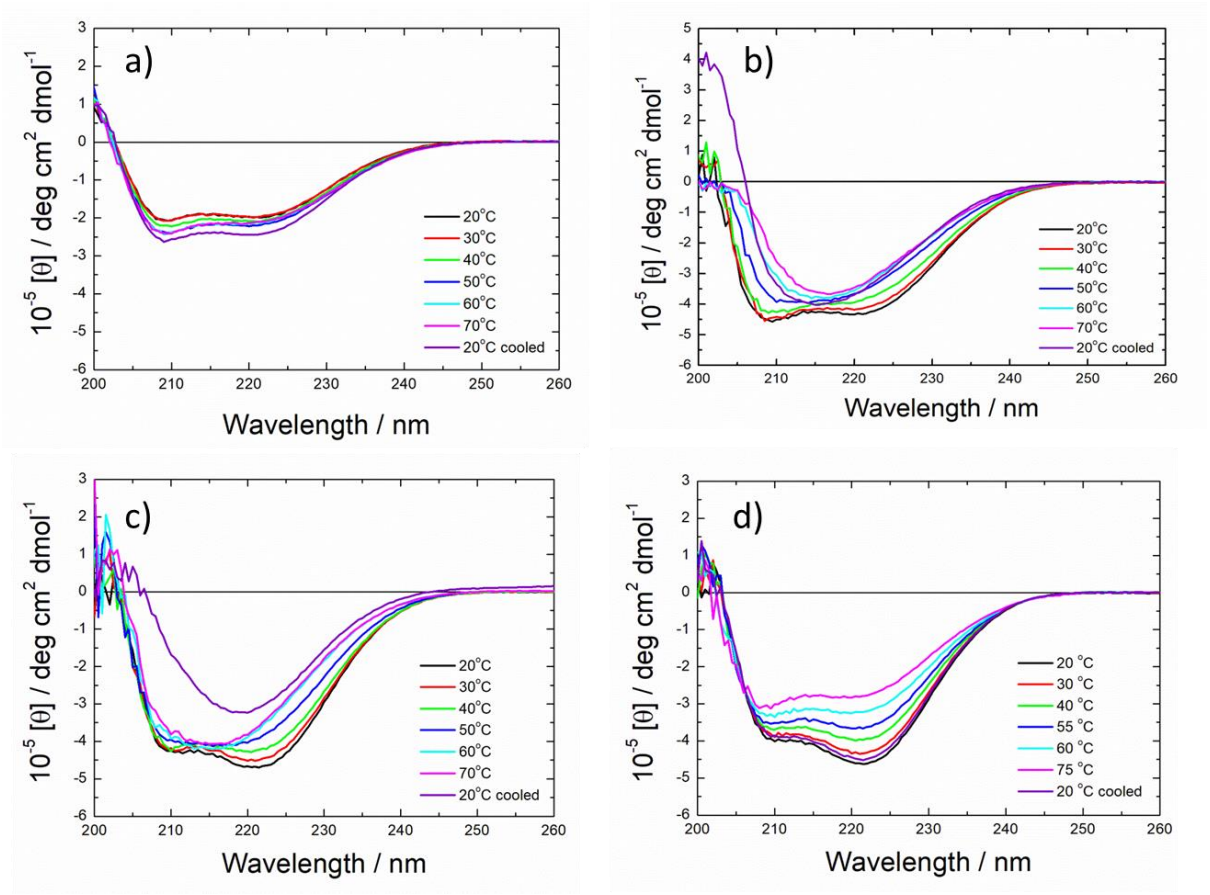

Figure 2.9. Temperature ramp CD spectra using 0.5 wt% solutions of PYY11, PYY17, PYY23, and PYY_{3-36} from 20-70 °C at pH 8 to show α-helix to β-sheet transition. a) PYY11, b) PYY17, c) PYY23, d) PYY_{3-36}.

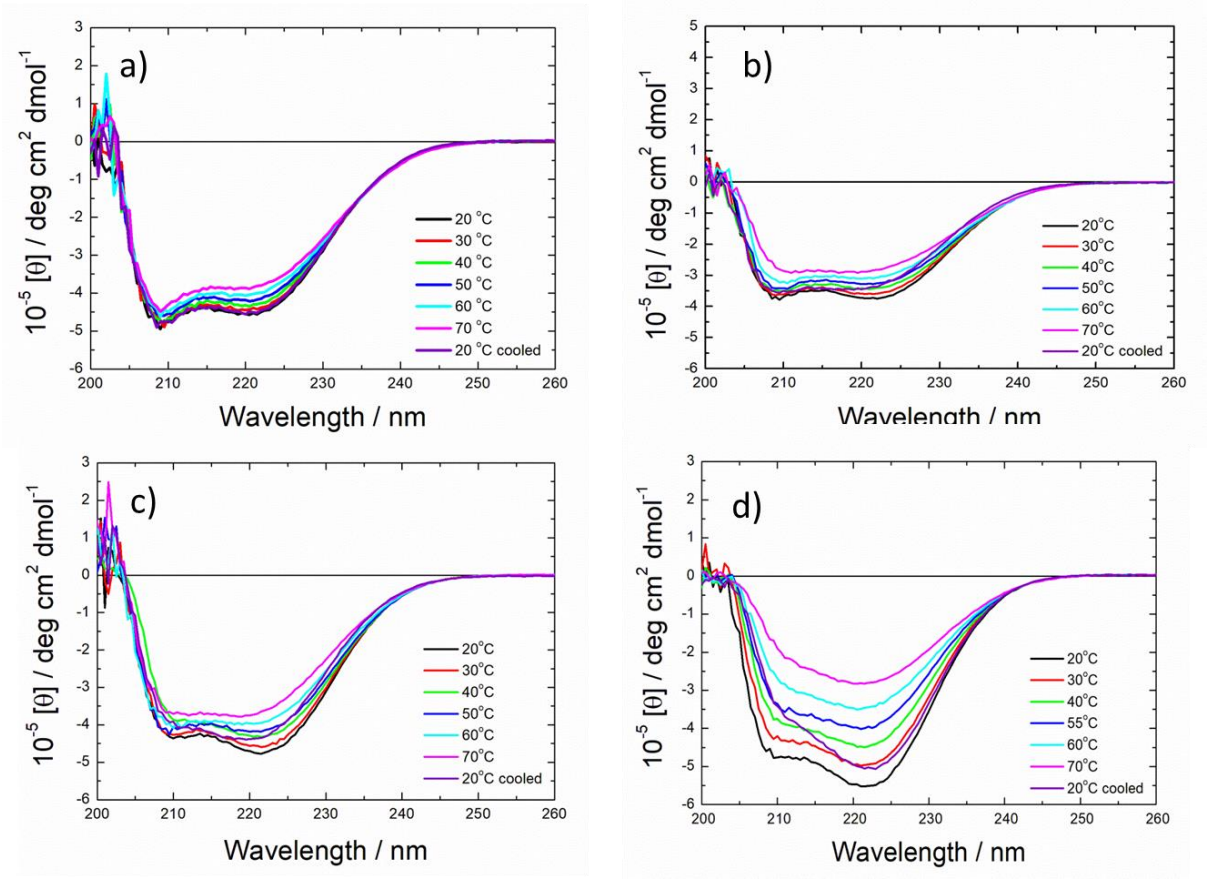

Figure 2.10. Temperature ramp CD spectra using 0.5 wt% solutions of PYY11, PYY17, PYY23, and PYY_{3-36} from 20-70 °C at native pH (pH 4 for lipidated peptides and pH 6 for unlipidated PYY_{3-36} in ultrapure water. a) PYY11, b) PYY17, c) PYY23, d) PYY_{3-36}.

The α-helix content was calculated based on a molar ellipticity value reported for an infinite length 100% helical peptide, where [Θ] = −37,400 deg cm^2 $dmol^{-1}$.[26-27] The results indicate that the position of lipidation does not appear to affect the secondary structure, apart from PYY11 at pH 8 where the α-helix content is significantly decreased (Figure 2.11). The calculated α-helical content of the peptides is summarized in Table 2.3. Apart from PYY11 at pH 8, each lipidated peptide shows a reduced dependence of α-helix content on pH and temperature compared to PYY_{3-36}. This useful result shows that lipidation enhances the stability of the peptides α-helical domain to changes in pH

and temperature. The results in Figure 2.11 also show that PYY23 has the highest α-helical content out of all three lipidated peptides studied throughout the whole pH and temperature range. This is the peptide which is lipidated in the core of the α-helical domain (Figure 2.1a).

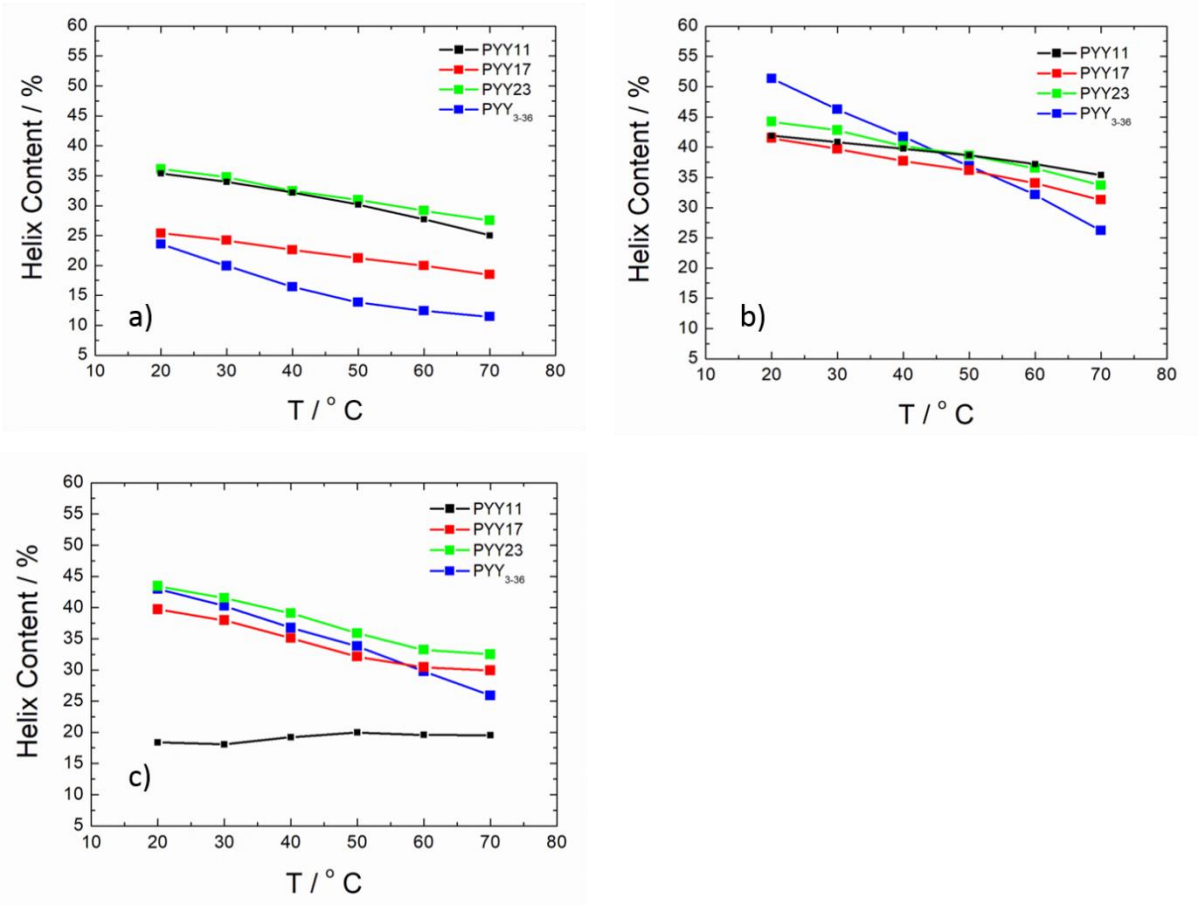

Figure 2.11. Calculated α-helix content of PYY_{3-36}, PYY11, PYY17, and PYY23 at; a) pH 2, b) the native pH of the peptide (pH 4 for lipidated peptides and pH 6 for native PYY_{3-36}, and c) pH 8, 20-70 °C.

Table 2.3. Calculated α-helix content of PYY_{3-36}, PYY11, PYY17, and PYY23 at pH 2, native pH in ultrapure water (pH 4 for lipidated and pH 6 for unlipidated peptide), and pH 8, at 20 °C.

Helix Content (%) at 20 °C	pH 2	pH 4 (native pH in ultrapure water)	pH 8
PYY_{3-36}	19.9	43.3	36.3
PYY11	29.9	35.3	15.5
PYY17	21.4	35.0	33.5
PYY23	30.5	37.3	36.6

The aggregation morphology of all 4 peptides was examined in the pH range 2-8, using SAXS and cryo-TEM, to investigate the impact of lipidation. Cryo- TEM avoids the need to dry or stain the sample, by vitrifying the solution. Images of all three lipidated peptides in the pH range 2-8 are shown in Figures 2.12-2.15. The images indicate the presence of long entangled fibers with some globular objects, with variable lengths of several hundred nanometres for PYY11 at pH 8, PYY17 at pH 2−8, and PYY23 at pH 4 and pH 8. Although the fibril length cannot be accurately determined at these magnifications, the fibril radius is measured as 8.0 nm (±1.6 nm) at pH 4, and 2.9 nm (±0.5 nm) at pH 8 for PYY17, and 8.2 nm (±1.6 nm), and 2.7 nm (±0.5 nm) at pH 4 and 8, respectively, for PYY23. Accurate radius values of PYY11 fibrils could not be measured due to the entangled nature of the structures. However, the radius was observed to be

approximately less than 10 nm. Images of PYY11 at pH 2 and 4, and PYY23 at pH 2 show the appearance of micelles with an average radius of 4.8 nm (±0.7 nm) and 3.7 nm (±0.8 nm) for PYY11, and 23 respectively. It is also very interesting to see that the position of lipidation affects the aggregated structure at pH 2, where PYY17 forms fibers, and PYY11 and PYY23 form micelles. This is presumably due to enhanced electrostatic interactions between charged residues in PYY11 and PYY23. The native peptide forms twisted nanotapes (Figure 2.15); it is thus clear that lipidation causes a change in aggregation, especially at low pH.

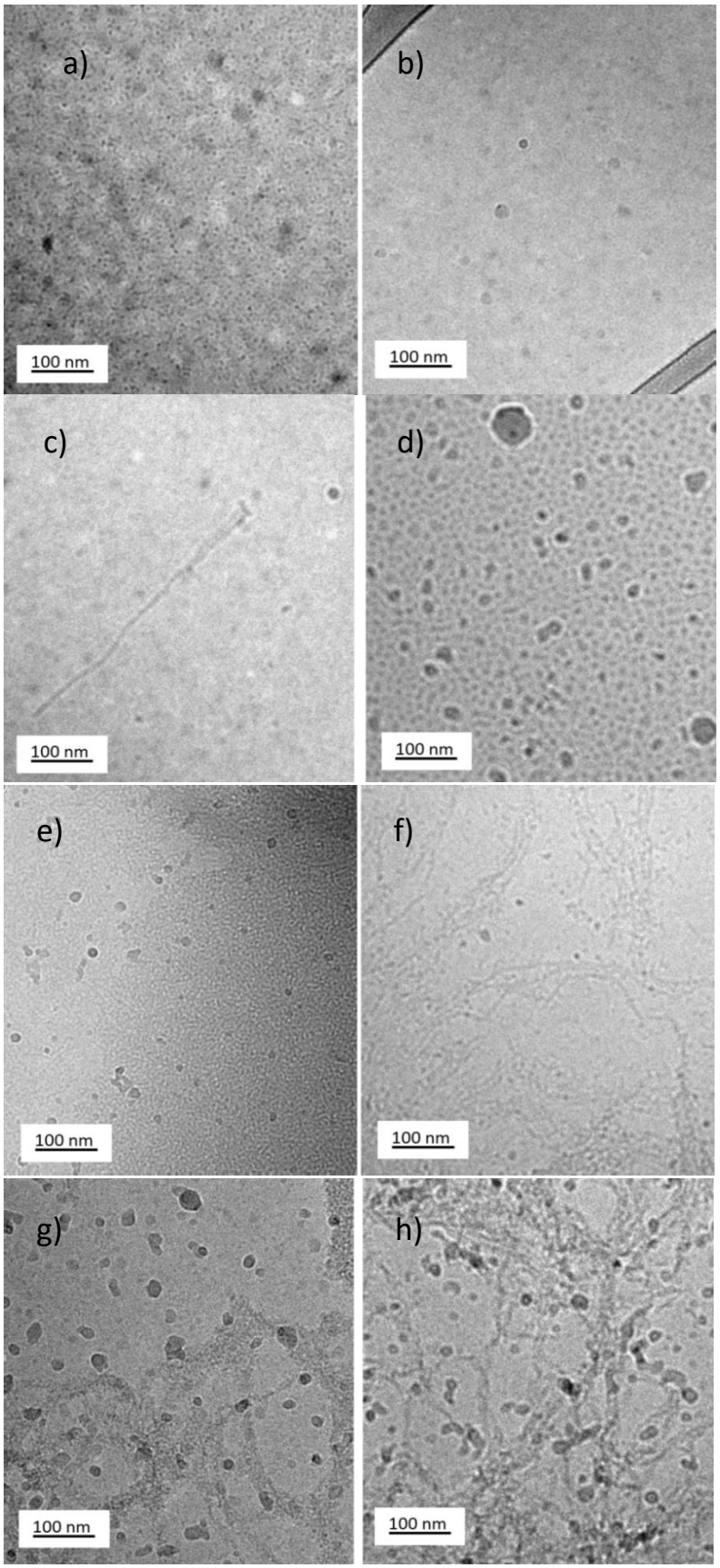

Figure 2.12. Cryo-TEM images of PYY11, 0.5 wt% in H_2O. a) pH 2, b) pH 2, c) pH 4 (native), d) pH 4 (native) e) pH 6, f) pH 6 g) pH 8, h) pH 8.

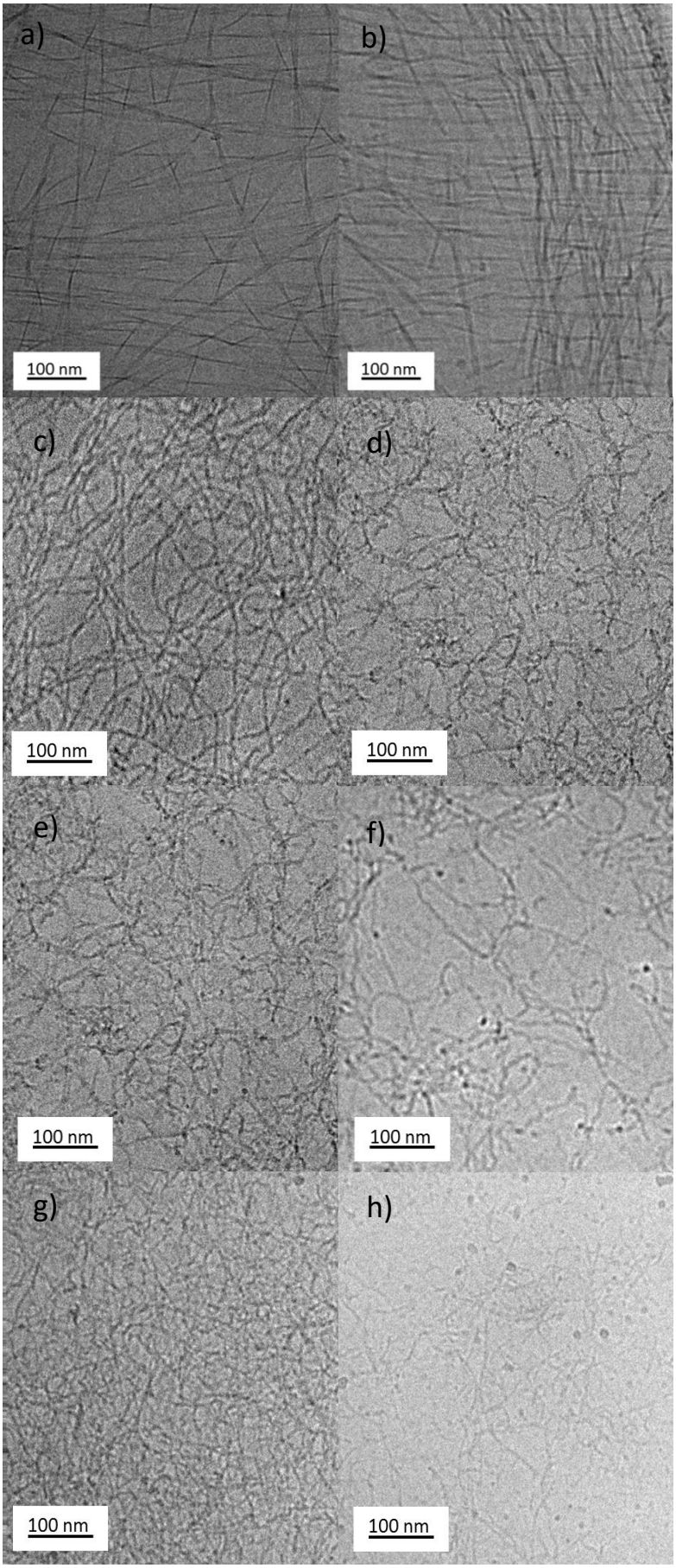

Figure 2.13. Cryo-TEM images of PYY17, 0.5 wt% in H_2O. a) pH 2, b) pH 2, c) pH 4 (native pH), d) pH 4 (native pH), e) pH 6, f) pH 6, g) pH 8, h) pH 8.

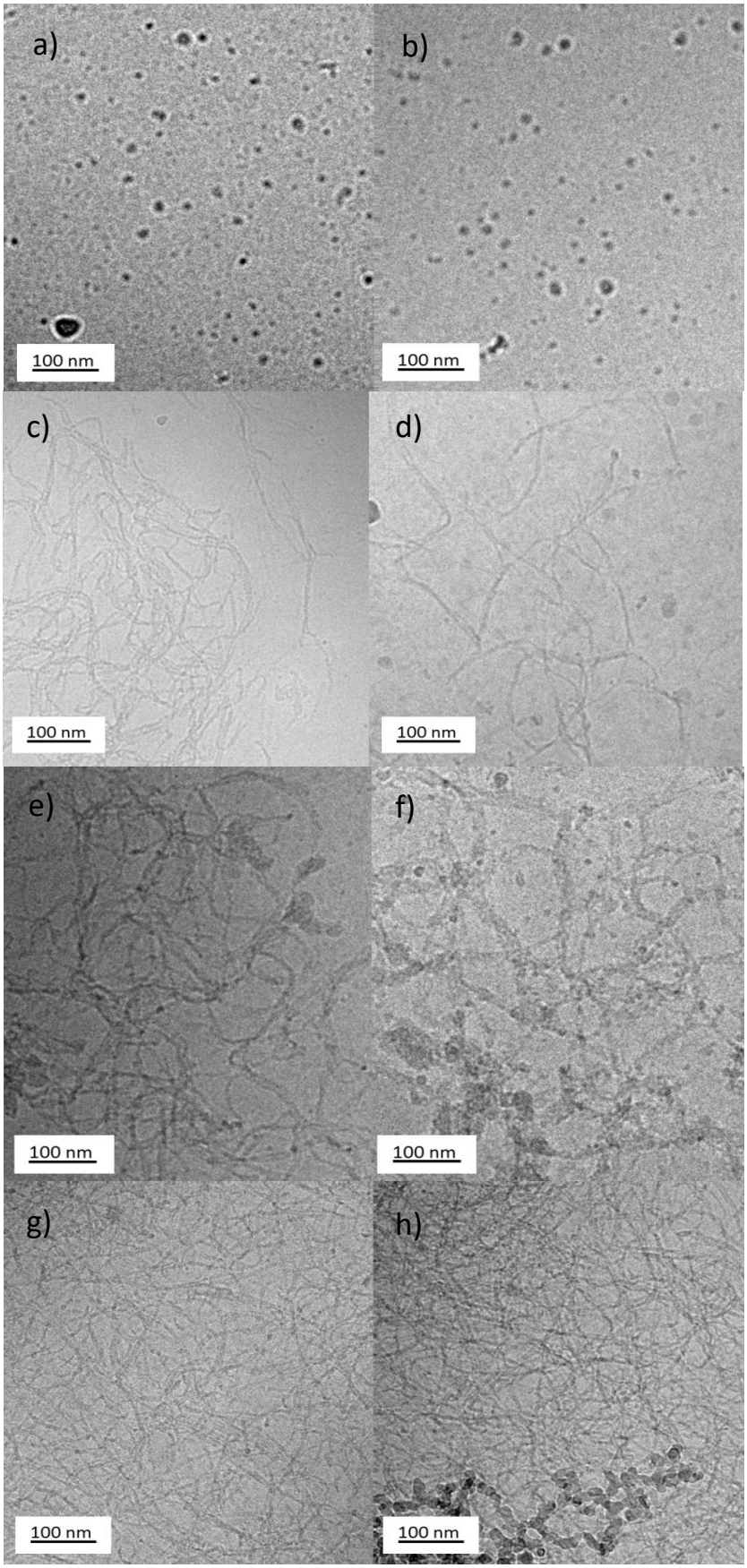

Figure 2.14. Cryo-TEM images of PYY23, 0.5 wt% in H_2O. a) pH 2, b) pH 2, c) pH 4 (native pH), d) pH 4 (native pH), e) pH 6, f) pH 6, g) pH 8, h) pH 8.

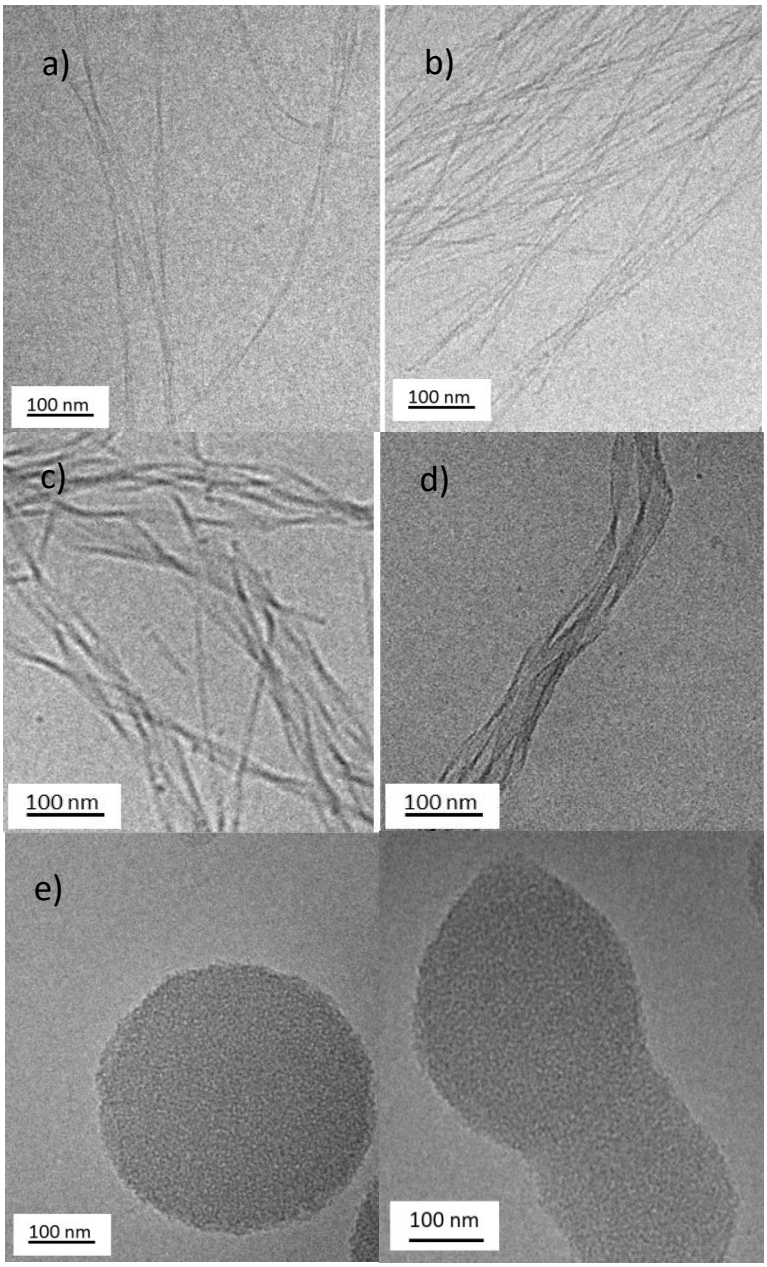

Figure 2.15. Cryo-TEM images of PYY_{3-36}, 0.5 wt% in H_2O. a) pH 2, b) pH 4, c) native pH (6.15), d) native pH (6.15), e) pH 8, f) pH 8.

Cryo-TEM was complimented with SAXS, which provides accurate dimensions and internal structures of the nanostructures. The SAXS intensity profiles for PYY11, 17, and 23 are shown in Figure 2.16. The data for PYY_{3-36} is shown in Figure 2.17. The scattering data can be fitted to a spherical shell form factor for PYY11 at pH 2 and 4 and for PYY23 at pH 2. A long cylindrical shell form factor was used to fit the remaining data for the lipidated peptides. SAXS data of the native peptide, PYY_{3-36} was fitted to a generalized Gaussian coil at pH 2 and 6. This form factor is used to represent isolated peptide unimers in solution. Although cryo-TEM images show a population of twisted nanotapes, the SAXS profiles are dominated by unimers. The data at pH 8 was fitted to a bilayer Gaussian form factor which is used to represent nanotape structures. Despite the Cryo-TEM images of PYY_{3-36} at pH 8 showing aggregated clusters, the SAXS data indicates the presence of nanosheets. This is in contrast to the lipidated peptides, suggesting that lipidation significantly changes self-assembly throughout the whole pH range (pH 2−8). The fitted parameters are listed in Tables 2.4-2.7. The fittings were carried out using the software SASfit.[28] A notable observation when comparing SAXS data of the lipidated peptides across the whole pH range is the difference in radius (R) and shell thickness (DR) values (Figure 2.18). Changing the pH of PYY17 away from its native pH caused the radius to decrease, whereas for PYY23 the opposite occurred, whereby increasing the pH caused the radius value to increase. As the pH was raised from 2 to 8, the shell thickness for PYY17 also increased.

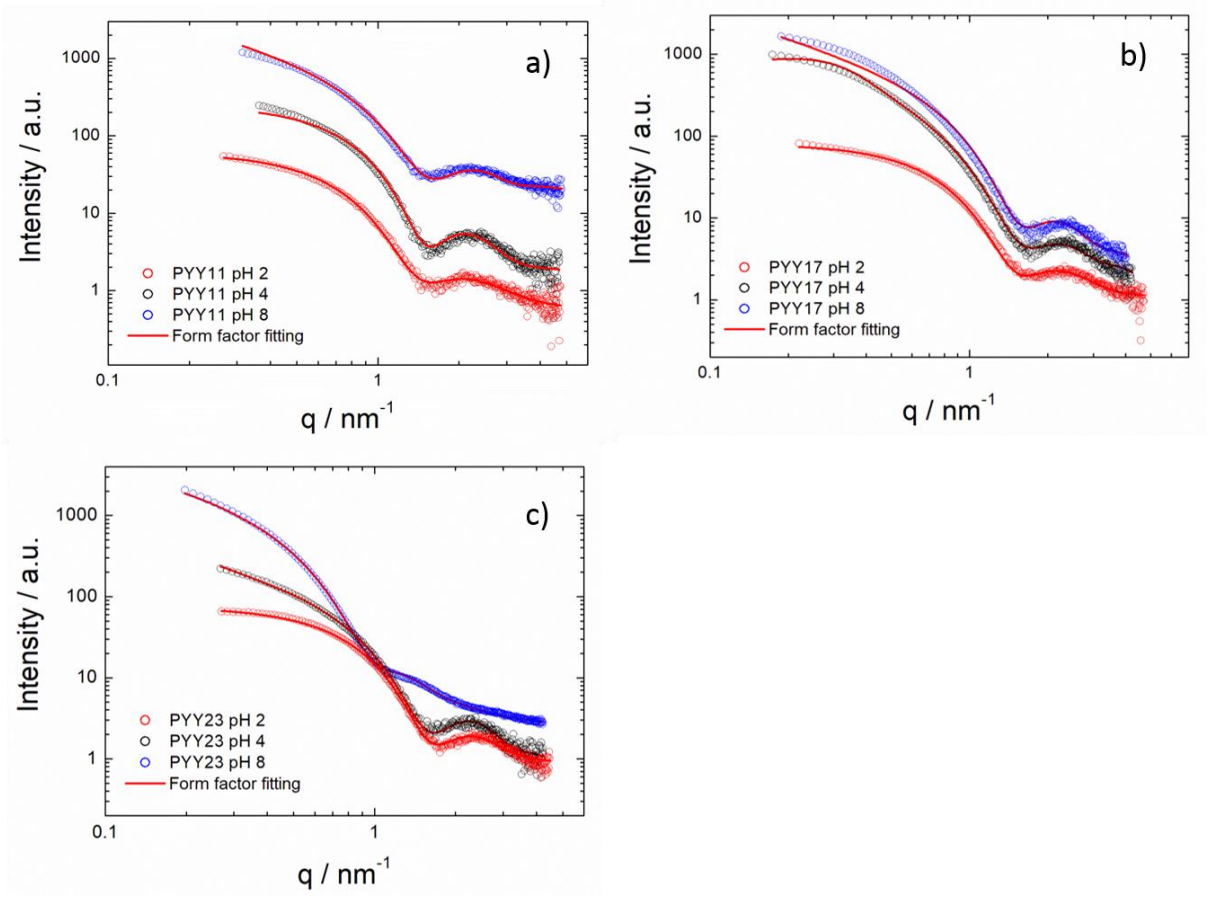

Figure 2.16. SAXS intensity profiles. a) PYY11, b) PYY17, c) PYY23 at pH 2-8. All samples were at 0.5 wt% and 20 °C. PYY11 data was fit to a spherical shell form factor at pH 2 and 4, and a long cylindrical shell form factor at pH 8. PYY17 data was fit to a long cylindrical shell form factor for all pH values. PYY23 was fit to a spherical shell form factor at pH 2 and a long cylindrical shell form factor at pH 4 and 8.

Table 2.4. SAXS form factor parameters of PYY11, and PYY23 at pH 2 and 4 at 0.5 wt% fit to a spherical shell form factor model using SASfit. Key: BG = background. N= scaling factor. σ = Gaussian width. R_1= inner radius. R_2 = outer radius. μ = scattering contrast of inner core. η = scattering contrast of shell.

Sample	BG	*N* / arb. units	σ/ nm	R_1 / nm	R_2 / nm	μ	η
PYY11 pH 2	1.24	1.83	0.834	1.69	0.826	-1.89	0.156
PYY11 pH 4	0.180	0.323	0.503	2.31	0.851	-1.30	0.137
PYY23 pH 2	0.900	1.93	0.502	2.06	0.771	-1.34	0.126

Table 2.5. SAXS form factor parameters of PYY11, PYY17, and PYY23 at pH 2, 4, and 8 and 0.5 wt% fit to a long cylindrical shell model using SASfit. Key: BG = background. N = scaling factor. σ = Gaussian width. R = inner radius. DR =shell thickness. L = length of cylinder. η_{core}= scattering contrast of core. η_{shell}= scattering contrast of shell. η_{solv}= scattering contrast of solvent.

Sample	BG	*N* / arb. units	σ/ nm	*R* / nm	*DR* / nm	L / nm	η_{core}	η_{shell}	η_{solv}
PYY11 pH 8	1.8	0.120	0.261	1.33	0.250	500	0.0212	0.218	0.0162
PYY17 pH 2	0.9	0.258	0.286	1.27	0.113	500	0.0357	0.312	0.0314
PYY17 pH 4	0.9	0.267	0.321	1.63	0.151	500	0.0408	0.241	0.0185
PYY17 pH 8	0.8	0.286	0.347	1.45	0.271	500	0.0469	0.165	0.0266
PYY23 pH 4	0.514	0.333	0.283	1.41	0.126	500	0.0322	0.285	0.0242
PYY23 pH 8	2.4	0.197	0.776	2.55	0.209	500	0.0570	0.180	0.0308

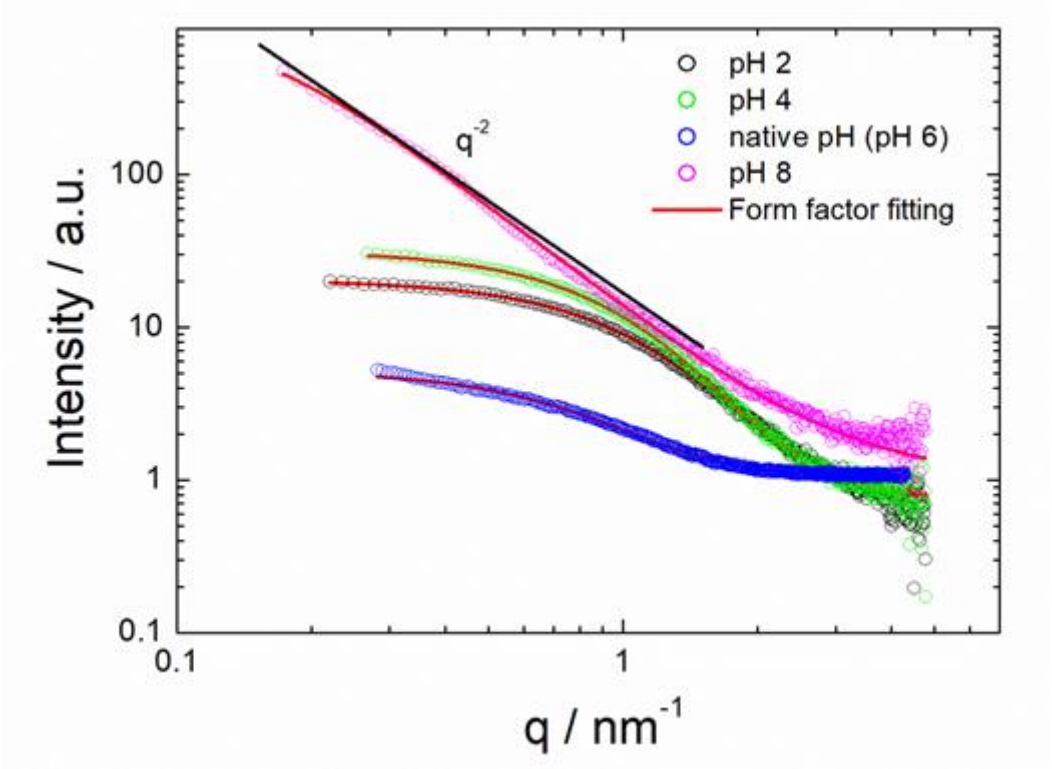

Figure 2.17. SAXS data and form factor fittings of PYY_{3-36} in the pH range 2-8. pH 2-6 was fitted to a generalized Gaussian coil form factor, characteristic of unimers. pH 8 data was fitted to a bilayer Gaussian form factor to represent nanosheet structures.

Table 2.6. SAXS form factor parameters of PYY_{3-36} at pH 2-6 and 0.5 wt% fit to a generalized Gaussian coil form factor model using SASfit. Key: BG = background. N= scaling factor. Rg = radius of gyration. ν = Flory exponent. I_0= forward scattering.

Sample	BG	*N* / arb. units	Rg / nm	ν	I_0
PYY_{3-36} pH 2	0.700	0.100	1.69	0.278	198
PYY_{3-36} pH 4	0.750	0.152	1.87	0.254	205
PYY_{3-36} pH 6 (native pH)	0.0207	1.00	22.1	0.295	0.0842

Table 2.7. SAXS fitting parameters of PYY_{3-36} at pH 8 and 0.5 wt% fit to a bilayer Gaussian form factor. BG = background. N = scaling factor. σ = Gaussian width. t = bilayer thickness. σ_{out}= Scattering density of outer Gaussians. b_{out} = width of outer Gaussians. σ_{core} = scattering density of inner Gaussian. b_{core} = width of inner Gaussians D = diameter of disc (fixed parameter).

Sample	BG	*N* / arb. units	σ/ nm	t/ nm	σ_{out}	b_{out}	σ_{core}	b_{core}	D/ nm
PYY_{3-36} pH 8	2.09	1.39	1.74	3.19	0.597	8.62×10^{-4}	3.59	-1.35×10^{-4}	1000

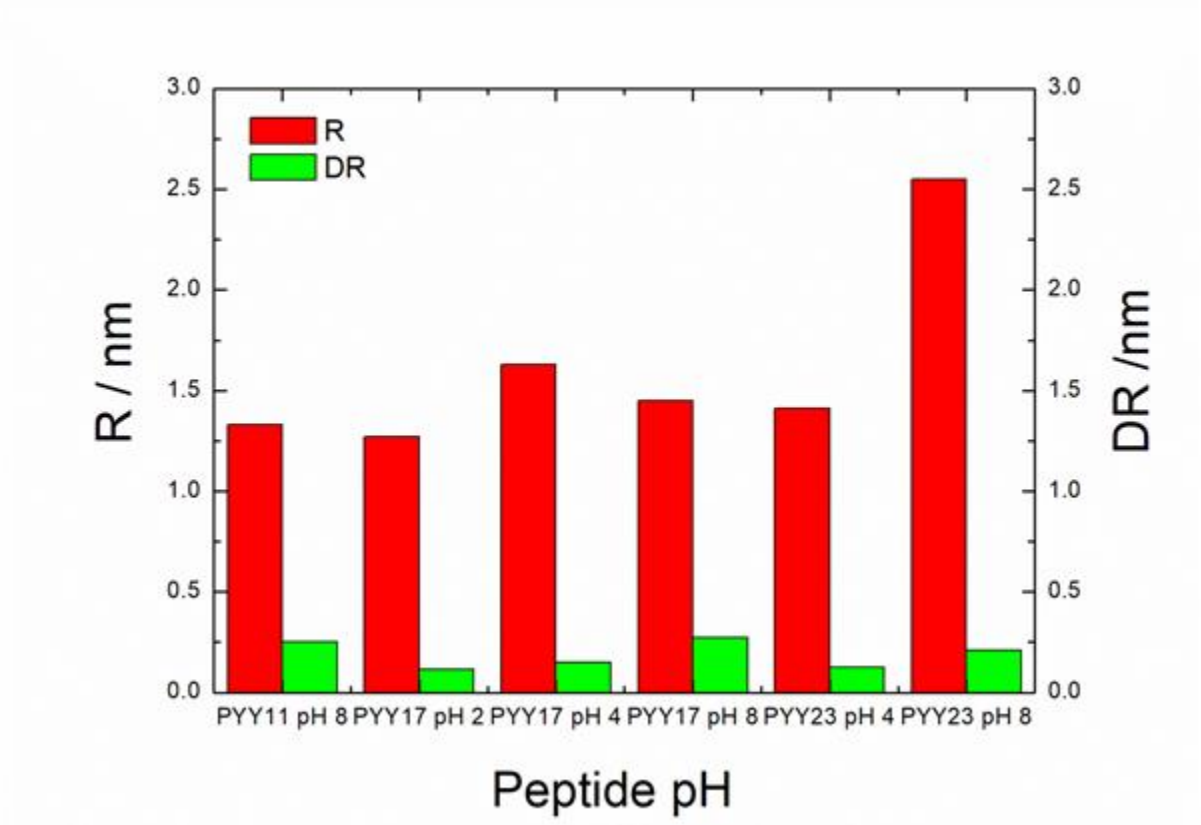

Figure 2.18. Radius R and shell thickness DR versus pH for PYY11, PYY17, and PYY23 using a long cylindrical shell form factor fitting from SASfit.

2.2.2 Hydrogel Studies

Hydrogels have many useful properties for use in therapeutic applications such as drug delivery and tissue engineering. Limited studies have been reported on lipidated peptide hydrogels thus far, in particular α-helical peptides. Some studies have been reported for lipidated β-sheet forming peptides, where a network of non-covalently cross-linked fibers under favourable conditions lead to gelation.[29-31] Since cryo-TEM and SAXS of the lipidated PYY_{3-36} peptides indicated the formation of fibers under appropriate pH conditions, it was of interested to examine their gelation properties. Studies were carried out in the pH range 2-9 to understand the impact of pH on gelation, and the native peptide was also studied to allow for comparison. Experiments to discover the possibility of gel formation of PYY17 and PYY23 were carried out by Sam Burholt, but the table of parameters are included here to allow for a full comparison. Interestingly, all three lipidated peptides formed hydrogels at pH 8, the pH at which a thermal transition from α-helix to β-sheet occurred in solution. Contrary to this, gelation of PYY_{3-36} was not observed throughout the pH range studied, highlighting the importance of the thermal transition, amongst other parameters, for gel formation. The pH values at which gels were observed are listed in Table 2.8 and representative images are shown in Figure 2.19. Results indicate that it is possible to form hydrogels by a simple pH adjustment from the peptides native pH, with heating. An interesting observation is that PYY11 only gelates at around pH 8, whereas the other two lipidated peptides formed hydrogels at pH 3, 6, and 7 also. At pH values close to pH 6, all three lipidated peptides formed precipitates, suggesting that this pH is close to the PI of the peptides as discussed previously, which may influence gelation. The reason for gelation not

occurring between pH 4 and 6 may be the increased charge on the peptides in this pH range due to the pKa values of the charged residues. This is very hard to quantify because the pKa in peptides can shift upon aggregation.[32-33]

Table 2.8. pH values at which gelation occurred for the lipidated peptides.

Successful pH values for gel formation (± 0.01)		
PYY11	PYY17	PYY23
pH 8.47	pH 3.80	pH 3.19
pH 8.76	pH 7.35	pH 6.09
	pH 7.77	pH 6.11
	pH 8.67	pH 6.56
	pH 8.88	pH 7.16
		pH 8.57

No gels formed from unlipidated PYY 3-36

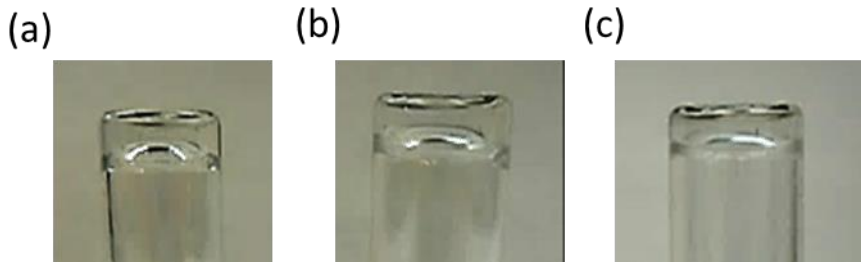

Figure 2.19. Gels formed by the lipidated peptides at pH 8. a) PYY11 b) PYY17, c) PYY23.

CD and fiber XRD were used to investigate gel conformation, along with SAXS and TEM to understand the morphology. Polarized optical microscopy (POM) was also used to observe green birefringence from binding of the dye Congo red to amyloid fibrils. Gel CD studies were carried out at pH 8, the pH at which all three lipidated peptides formed gels. Results (shown in Figure 2.20) show a β-sheet secondary structure, with a minimum near 217 nm. These results are distinctly different to the peptides in solution, where an α-helical structure was observed below 50 °C. Above 50 °C, a thermal transition from α-helix to β-sheet occurred as mentioned above. An interesting point to note is that at pH 6, PYY17 did not form a gel, but the CD data still shows β -sheet structure with a minimum at 217 nm (Figure 2.20a). As a result, it is suggested that the factors behind gelation a combination of pH change, and a thermal transition from α-helix to β-sheet.

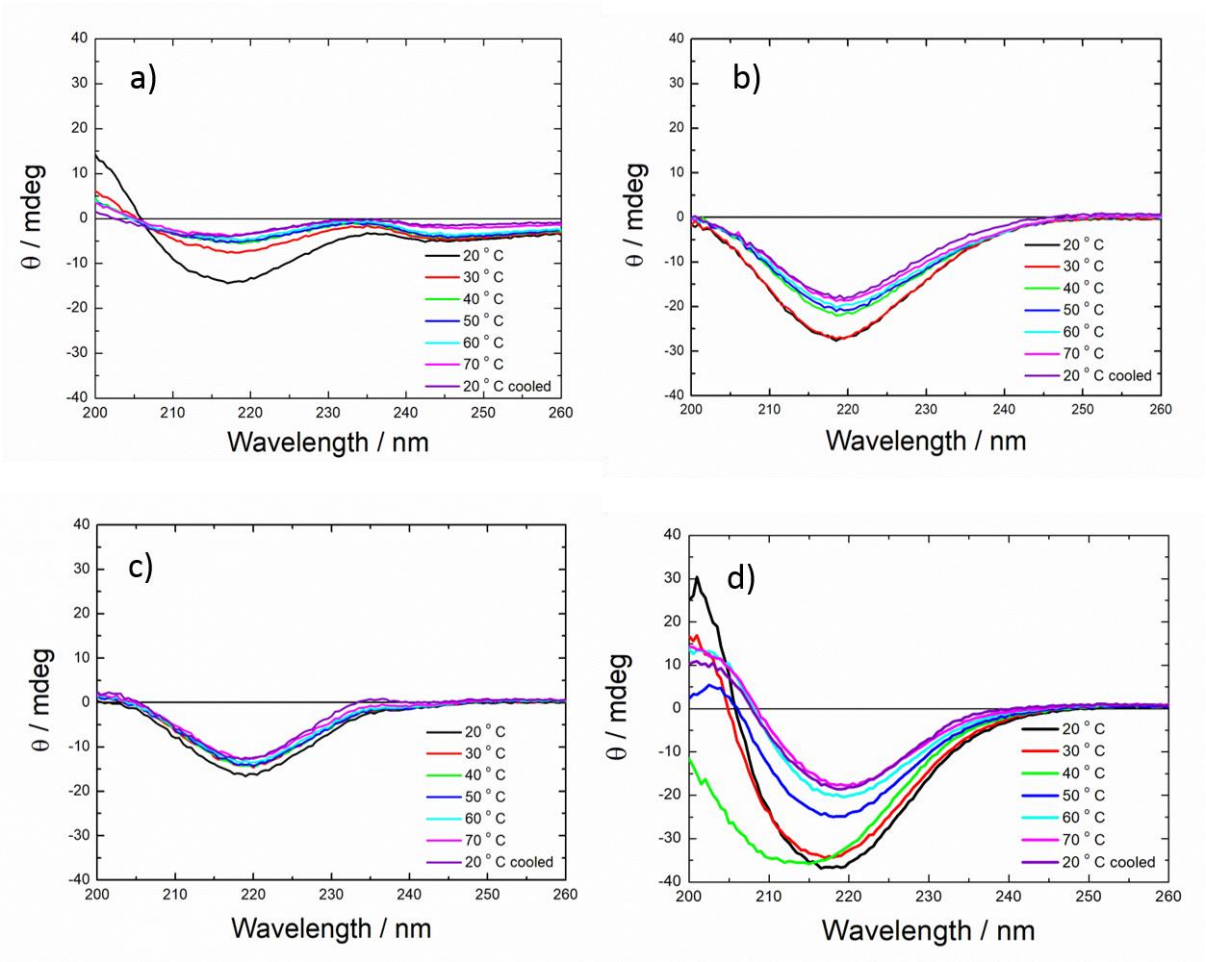

Figure 2.20. Temperature-dependent circular dichroism spectra at 2 wt% of: a) PYY17 pH 5.98, b) PYY17 pH 8.88, c) PYY23 pH 6.09, d) PYY23 pH 8.60.

The thermal transition from α-helix to β-sheet of PYY11 was examined using CD at pH 8 (Figure 2.21). The experiment was carried out using a 2 wt % peptide solution and this pH was chosen as the pH at which all lipidated peptides formed the strongest gels. The pH was changed using NaOH (0.5 M) and HCl (0.5 M). The sample was heated in a water bath at 60 °C and measurements were taken every 20 min until the transition occurred. The results show that the transition started to occur at 60 minutes and after 80 minutes the structure was fully β-sheet with a minimum at 218 nm.

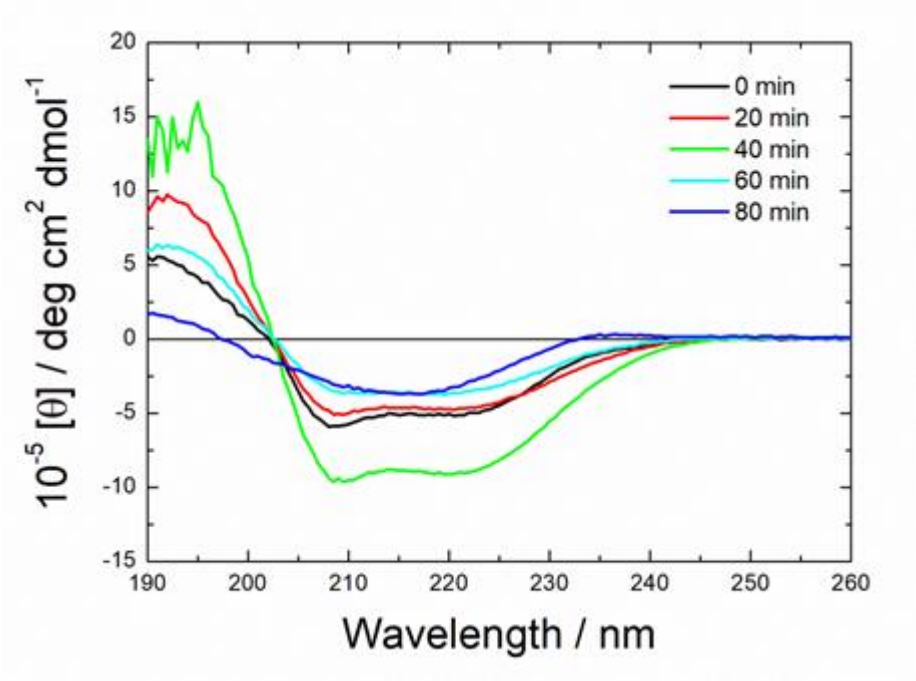

Figure 2.21. CD spectra during annealing at 56 °C, showing the thermal transition of PYY11 at pH 8.47 and 2 wt% from α-helix to β-sheet.

SAXS data measured for the gels is shown in Figure 2.22b and was fitted to a long cylindrical shell model using SASfit, the fitting parameters being shown in Table 2.9. The form factor profiles and fitting parameters of PYY23 appear to be distinctly different to the other two lipidated peptides. The radius R is significantly larger than the others and the shell thickness DR is significantly lower. TEM images of all peptide gels (Figure 2.22c) show a network of entangled fibers, very similar to the cryo-TEM images of the samples in solution. An interesting observation is that PYY11 and PYY23 did not form a gel at pH 2, which is informative in terms of understanding the mechanism of gelation, since they both form micelles at pH 2, whereas PYY17 forms fibers. This indicates that a fiber morphology could be crucial to gelation.

Fiber X-ray diffraction (XRD) was performed to compliment the SAXS data, providing information on the local packing of the lipidated peptides, i.e. on secondary structure.

The obtained 2D patterns were isotropic, so the data were reduced to one-dimensional form. The resulting intensity profiles are shown in Figure 2.23. The results for PYY17 and 23 show α-helical structures with sharp peaks corresponding to a d- spacing = 5.70 Å.[34] XRD results of PYY11 show the presence of β-sheet structures with sharp peaks corresponding to d-spacings = 10.01 and 4.65 Å.[35] These are assigned as inter-sheet and inter-strand spacings in a 'cross-β' XRD pattern respectively. The apparent discrepancy between XRD showing α-helical structure and cryo-TEM/SAXS showing fibril structures requires further investigation to give explanation.

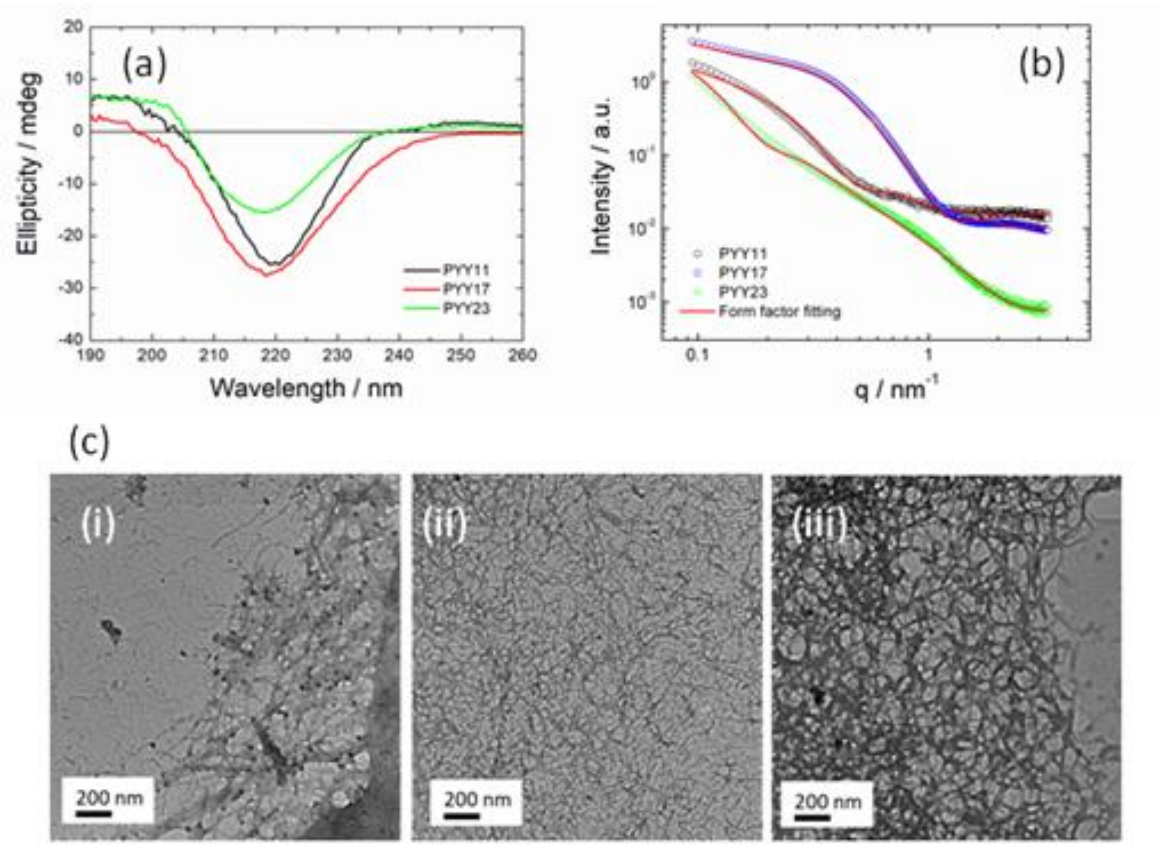

Figure 2.22. (a) CD spectra from gels of all three lipidated peptide at pH 7-8 and 20 ^{o}C. (b) SAXS intensity profiles and form factor fittings for gels of PYY11, PYY17, and PYY23 at pH 7-8. All data was fitted to a long cylindrical shell form factor. (c) TEM images of the peptide hydrogels at pH 8. (i) PYY11, (ii) PYY17, (iii) PYY23.

Table 2.9. Form factor fitting parameters for PYY11, PYY17 and PYY23 gels at pH 7-8 and 2 wt%, all fitted to a long cylindrical shell model. Key: BG = background. N = scaling factor. σ = Gaussian width. R = inner radius. DR =shell thickness. L = length of cylinder. η_{core}= scattering contrast of core. η_{shell}= scattering contrast of shell. η_{solv}= scattering contrast of solvent.

Sample	BG	*N* / arb. units	σ/ nm	*R* / nm	*DR* / nm	L / nm	η_{core}	η_{shell}	η_{solv}
PYY11 pH 8	1.58×10^{-3}	5.37×10^{-9}	12.9	22.6	28.1	5000	-3.68×10^{-5}	-5.49×10^{-4}	2.00×10^{-4}
PYY17 pH 8	1.02×10^{-2}	1.01×10^{-5}	23.1	30.0	48.6	1000	2.70×10^{-4}	-6.91×10^{-5}	0.00
PYY23 pH 7	8.26×10^{-6}	1.45×10^{-7}	14.8	55.2	6.55	5000	1.10×10^{-3}	3.57×10^{-3}	5.90×10^{-4}

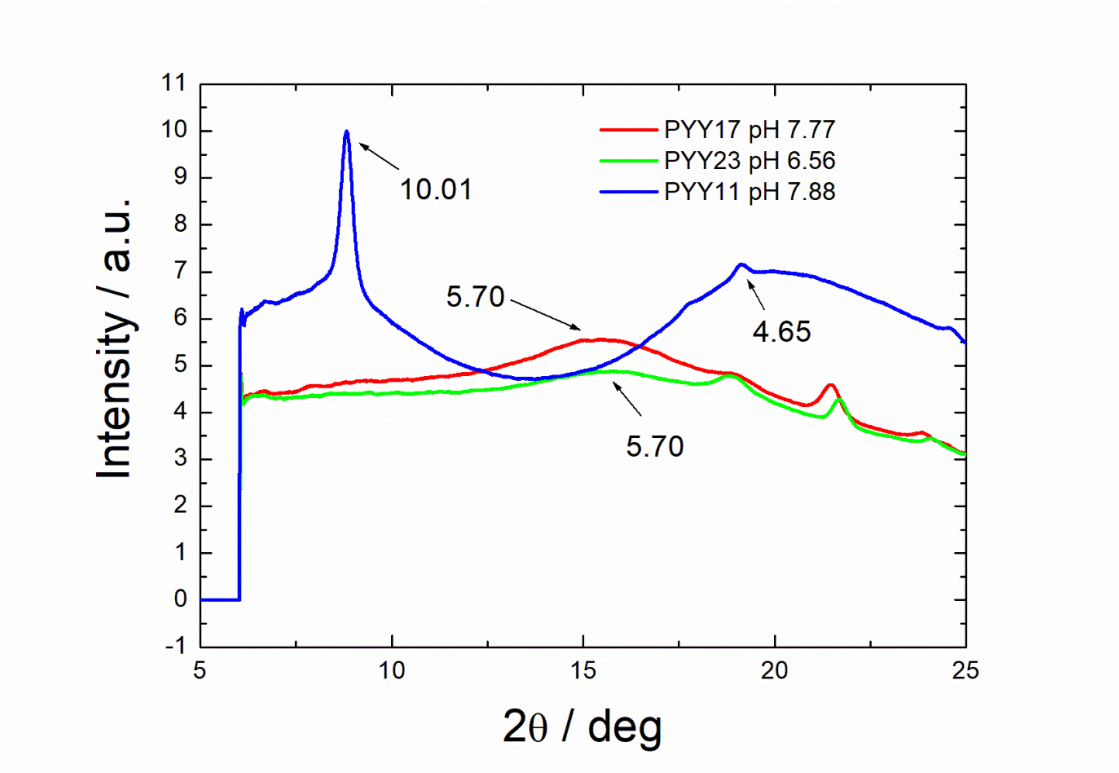

Figure 2.23. Fibre XRD intensity profiles for PYY11, PYY17 and PYY23, measured from a hydrogel or from a dried stalk at varied pH, with main Bragg spacing indicated.

Polarized optical microscopy was carried out on the peptide hydrogels using Congo red as a staining agent to show green birefringence in polarized light from the presence of amyloid fibrils.[36-37] Congo red is an azo dye that has an orientated arrangement on amyloid fibrils by forming hydrogen bonds between amino and hydroxyl groups within the dye and on amyloid structures.[38] When stained with Congo red in alkaline conditions, the fibrils appear red in unpolarized light, and green in polarized light. Microscopy images are shown in Figure 2.24 and yellow/green birefringence is observed for all three lipidated peptides, indicating the presence of amyloid fibrils.

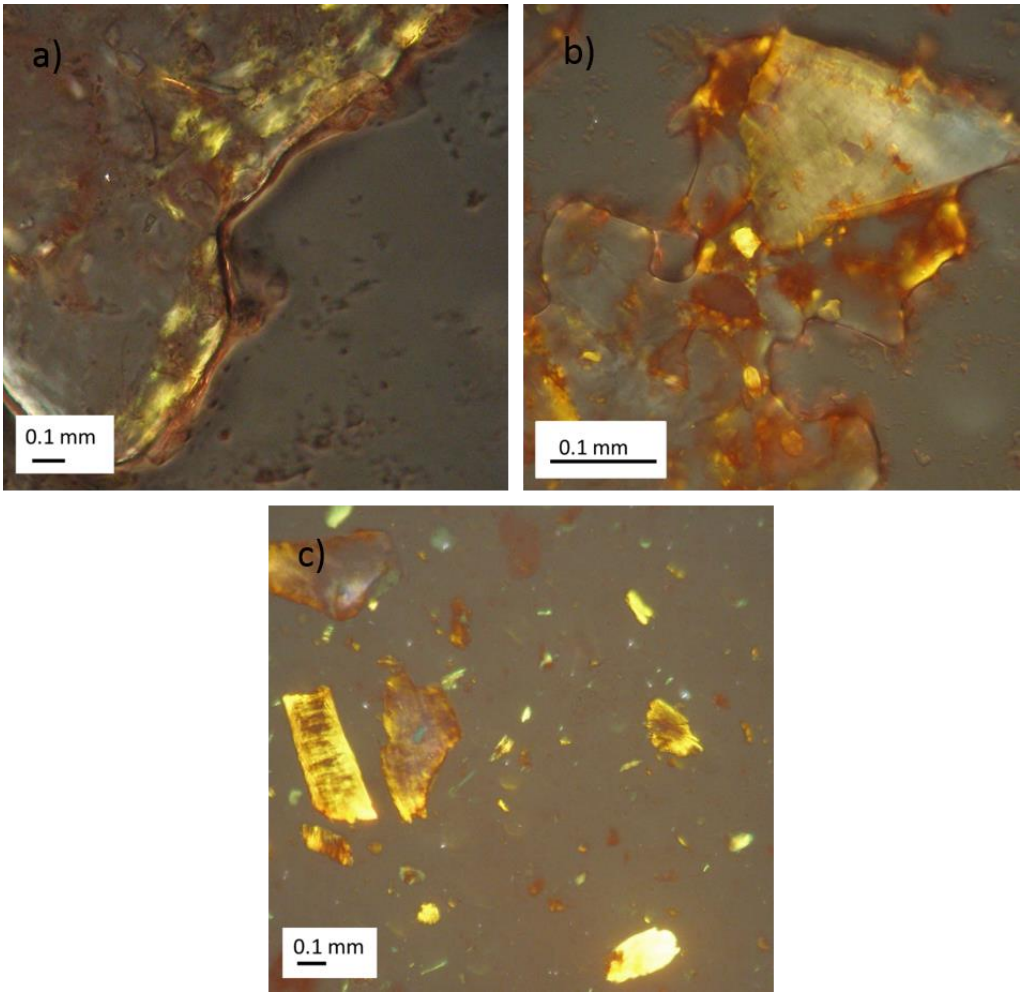

Figure 2.24. Polarized optical microscopy images of samples stained with Congo red to show birefringence in the presence of amyloid fibrils. a) PYY11 gel at pH 8, b) PYY17 gel at pH 8, c) PYY23 gel at pH 8.

2.2.3 Self-Assembly of PYY_{3-36} with Vitamin B_{12}

Although many studies on the use of PYY_{3-36} to reduce food intake have been very promising, the need for it to be injected creates problems with patient compliance and quality of life. Challenges associated with oral peptide therapeutics include: rapid renal clearance, proteolytic degradation in the stomach and intestine, and poor absorption due to their inability to cross the ileal epithelium.[39]

The vitamin B_{12} dietary uptake pathway for use as a peptide delivery system has gained a significant amount of interest over the years.[40] Vitamin B_{12} (B_{12}), also known as cobalamin, is a water-soluble essential nutrient co-factor involved in the metabolism of every cell in animals, including humans. B_{12} is the largest B vitamin with a complex molecular structure. It consists of a nucleotide moiety and a planar porphyrin-like corrin ring, containing a central cobalt (III) atom Figure 2.25.[40] Only certain bacteria synthesise B_{12}, and the main source for humans is found via dietary intake of meat and dairy products.

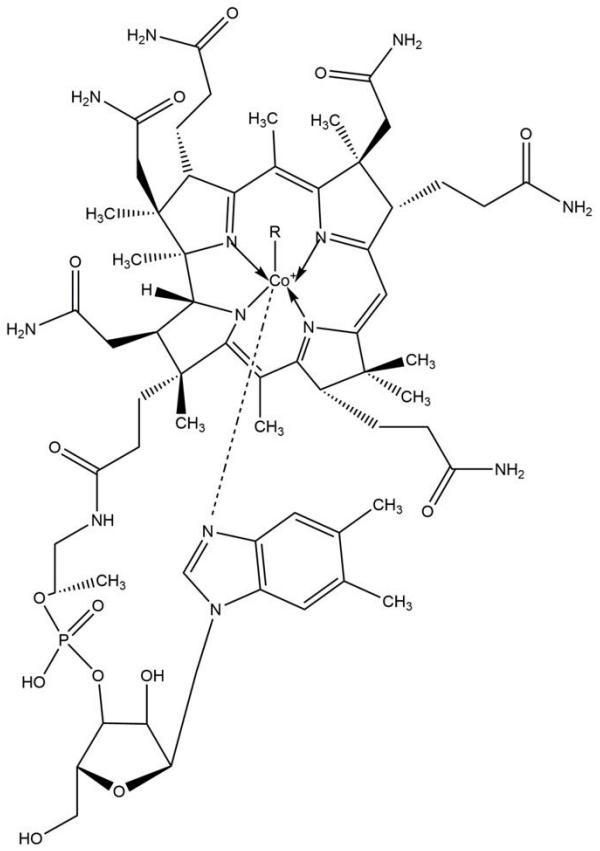

Figure 2.25. Chemical structure of vitamin B_{12}.

Humans have developed a highly efficient absorption and cellular uptake mechanism of B_{12} in the gastrointestinal tract, which can be adapted for peptide delivery as long as the recognition and affinity of the B_{12} binding proteins aren't altered.[39-40] B_{12} is efficiently absorbed and is protected in the GI tract by salivary haptocorrin (HC), a glycoprotein that has a high affinity for B_{12} under acidic conditions when the pH is less than 3.[40] HC protects B_{12} from acid hydrolysis in the stomach, and upon binding forms a HC to B_{12} complex, which then travels from the stomach to the duodenum. The pH is increased in the duodenum, causing a decrease in affinity of HC for B_{12}. This allows HC to be digested by pancreatic enzymes, releasing B_{12}. Following this, a second glycoprotein, intrinsic factor (IF) binds to B_{12}, to facilitate the transport across the intestinal enterocyte via

receptor mediated endocytosis. Finally, B_{12} appears in the blood plasma up to 4 hours after ingestion.[40]

A vital aspect when considering the use of B_{12} as a dietary uptake drug delivery system is receptor selectivity and activity. The interaction of B_{12} with the drug must not reduce the drug's receptor selectivity, and the vitamin must still be recognised by the proteins involved in its uptake.[40] In vitro studies on conjugated B_{12}-PYY_{3-36} have been promising, showing a similar agonism for the Y2 receptor compared to native PYY_{3-36}, implying that B_{12} does not seem to affect the biological activity of both the vitamin and the peptide.[40]

Although investigations have been carried out on conjugated B_{12}-PYY_{3-36} systems to look at biological activity, there seems to be limited research on non-covalent interactions. The following experiments look at the effect of B_{12} on the self-assembly of PYY_{3-36}, to gain an insight into how they potentially interact with each other with relevance to possible drug delivery systems.

CD studies of PYY_{3-36} with different molar ratios of B_{12} are shown in Figure 2.26a. There appears to be no significant impact on secondary structure using a 0.1:1 molar ratio of

B_{12} to PYY_{3-36}, with the spectrum exhibiting a predominant α-helix structure. Upon increasing the ratio of B_{12} to 2:1 B_{12}:PYY_{3-36} however, there is a substantial loss of α-helical structure, with reduced molar ellipticity, indicating that the addition of B_{12} above a concentration threshold disturbs secondary structure.

Cryo-TEM images show that the increased molar ratio of B_{12} enhances aggregation, with a significantly larger number of nanotapes present as the molar ratio increases from 0.1:1 to 2:1. SAXS was used to investigate this further. The data (Figure 2.26b) implies

that the different molar ratios have little impact on aggregation, since the scattering patterns mainly correspond to unimers, similar to PYY_{3-36} on its own. SAXS data was fit to a generalized Gaussian coil form factor to represent these unimers, and the fitting parameters are shown in Table 2.10. The discrepancy between cryo-TEM and SAXS, with cryo-TEM showing nanotapes which are not detected by SAXS can be attributed to the structures being dominated by unimers. This is due to SAXS measurements giving an overall average of the size and structure. SAXS parameters don't appear to differ substantially when adding B_{12}, with all ratios of B_{12} with PYY_{3-36} having similar structural parameters. As a result it can be concluded that the addition of vitamin B_{12} to PYY_{3-36} does not impact aggregation significantly, and thus is a promising starting point to understanding the non-covalent interactions between them both.

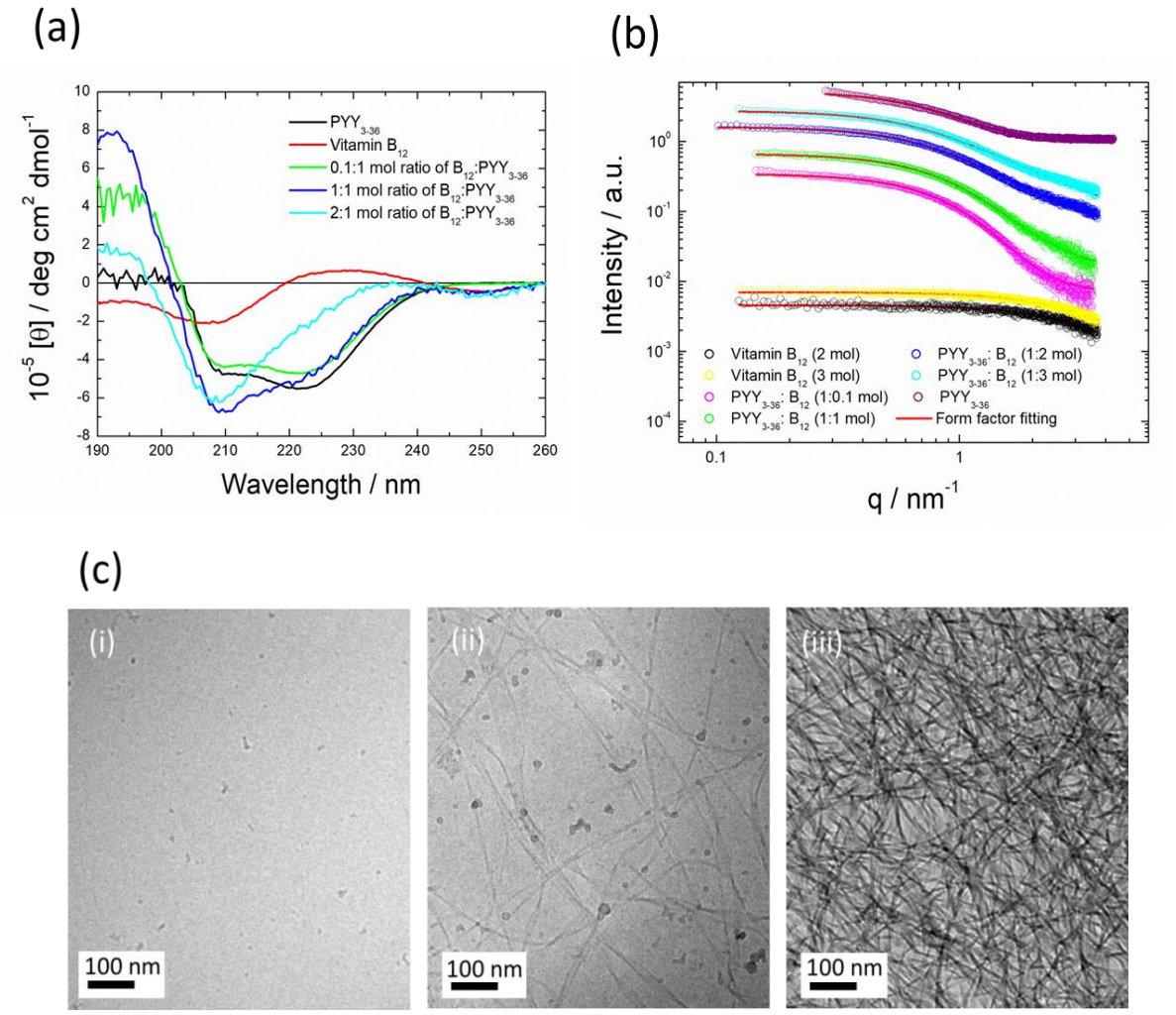

Figure 2.26. a) CD spectra of PYY_{3-36} with vitamin B_{12} at 0.1:1, 1:1, and 2:1 molar ratios and 20 °C. b) SAXS intensity profiles and form factor fittings of PYY_{3-36} with vitamin B_{12} at different molar ratios and native pH. All data was fitted to a generalized Gaussian coil form factor characteristic of unimers. c) TEM images of PYY_{3-36} with vitamin B_{12}. (i) B_{12}, (ii) 1:1 PY_{3-36} to B_{12}, (iii) 1:2 PYY_{3-36} to B_{12}.

Table 2.10. SAXS form factor parameters of PYY_{3-36} (0.5 wt%) with vitamin B_{12} at native pH fit to a generalized Gaussian coil form factor model using SASfit. Key: BG = background. N= scaling factor. Rg = radius of gyration. ν = Flory exponent. I_0= forward scattering.

Sample	BG	*N* / arb. units	Rg / nm	ν	I_0
Vitamin B_{12}	$4.0x10^{-4}$	$9.83x10^{-2}$	5.292	0.410	$6.7x10^{-2}$
PYY_{3-36}:B_{12} (1:0.1 mol)	$7.0x10^{-4}$	0.455	20.31	0.226	$7.5x10^{-2}$
PYY_{3-36}:B_{12} (1:1 mol)	$7.0x10^{-4}$	0.447	20.08	0.310	$7.3\ x10^{-2}$
PYY_{3-36}:B_{12} (1:2 mol)	$9.0x10^{-4}$	0.566	20.93	0.480	$7.0x10^{-2}$
PYY_{3-36}:B_{12} (1:3 mol)	$9.0x10^{-4}$	0.700	21.43	0.560	$6.4x10^{-2}$
PYY_{3-36} pH 6 (native pH)	$2.1x10^{-4}$	1.00	22.12	0.295	$8.4x10^{-2}$

2.3 Conclusion

Various physical characterisation techniques including but not limited to CD, microscopy, and X-ray techniques, have been employed to investigate the impact of lipidation on the self-assembly and gelation behaviour of the gut derived peptide hormone PYY_{3-36}.

Three lipidated derivatives of PYY_{3-36} were studied, with C_{16} alkyl chains covalently attached at positions 11, 17, and 23 to the peptide by substitution of γ-L-glutamoyl(Nα-hexdecanoyl) lysine residues. Results show distinct differences between lipidated and

unlipidated peptides, with the lipidated peptides having micelle and fiber morphology, and the unlipdated peptide being predominantly unimers with some nanotape structures. Furthermore, the lipidated peptides were more stable to pH and temperature change, and formed hydrogels under certain pH and temperature changes. The unlipidated peptide did not gelate under the conditions studied.

Further experiments were carried out using vitamin B_{12} (B_{12}), to look at the non-covalent interactions between B_{12} and PYY_{3-36}. Results show that the addition of B_{12} has an impact on self-assembly. As the ratio of B_{12} was increased, the α-helical conformation decreased shown by CD. SAXS showed predominantly unimers throughout the concentration range of B_{12} used, and cryo-TEM suggested that B_{12} enhanced fibril aggregation as the concentration was increased. Further experiments are required to understand the behaviour in more detail but these experiments are a promising starting point.

2.4 Materials and Methods

Human PYY_{3-36} acetate salt was synthesised by Bachem, Switzerland. The molecular mass by MALDI-MS was measured by the supplier using a Shimadzu Biotech Axima-CFR instrument, and found to be 4049.61 g mol^{-1} (expected: 4047.07 g mol^{-1}). The molecular mass was checked in our labs by ESI-MS using a Thermo Scientific LTQ- Orbitrap XL instrument, and found to be 4049.07 g mol^{-1}. The purity was 96.9% determined by HPLC.

PYY11 acetate salt was custom synthesised by Bachem, Switzerland. The molecular mass by MALDI-MS was measured by the supplier using a Shimadzu Biotech Axima-CFR

instrument, and found to be 4458.19 g mol^{-1} (expected: 4454.37 g mol^{-1}).The molecular mass was checked in our labs by ESI-MS using a Thermo Scientific LTQ- Orbitrap XL instrument, and found to be 4458.41 g mol^{-1}. The purity was 95.4 % as determined by HPLC.

PYY17 acetate salt was custom synthesised by Bachem, Switzerland. The molecular mass by MALDI-MS was measured by the supplier using a Shimadzu Biotech Axima-CFR instrument, and found to be 4389.13 g mol^{-1} (expected: 4387.32 g mol^{-1}). The molecular mass was checked in our labs by ESI-MS using a Thermo Scientific LTQ- Orbitrap XL instrument, and found to be 4389.32 g mol^{-1}. The purity was 97.8 % as determined by HPLC.

PYY23 acetate salt was custom synthesised by Bachem, Switzerland. The molecular mass by MALDI-MS was measured by the supplier using a Shimadzu Biotech Axima-CFR instrument, and found to be 4389.27 g mol^{-1} (expected: 4387.32 g mol^{-1}). The molecular mass was checked in our labs by ESI-MS using a Thermo Scientific LTQ- Orbitrap XL instrument, and found to be 4389.33 g mol^{-1}. The purity was 98.3% as determined by HPLC.

2.4.1 Fluorescence Spectroscopy

Fluorescence spectra were recorded with a Varian Cary Eclipse fluorescence spectrometer (Varian IEEE-488, Australia) with samples in 4 mm inner diameter quartz cuvettes. Pyrene assays were performed using 1.3 $x10^{-3}$to 0.13 wt% peptide solutions, in 2.167 $x10^{-5}$ wt% pyrene solution. The samples were excited at a wavelength λ_{ex} = 339 nm, and the fluorescence emission was measured for λ = 360−500 nm. Thioflavin T (ThT) assays were performed using 1.3 $x10^{-3}$ to 0.13 wt% peptide solutions, in 5.0 x 10^{-3} wt%

ThT solution. The samples were excited at a wavelength λ_{ex} = 440 nm, and the fluorescence emission was measured for λ = 460−600 nm.

2.4.2 Circular Dichroism (CD)

CD spectra were recorded using a Chirascan spectropolarimeter (Applied Photophysics, UK). Spectra are presented with absorbance A < 2 at any measured point with a 0.5 nm step, 1 nm bandwidth, 1 s collection time per step, and 3 repeats. The CD signal from the background (water) was subtracted from the CD signal of the sample solution. Ellipticity is reported as the mean residue ellipticity ([θ], in deg cm^2/dmol) and calculated as:

$[\theta] = [\theta]_{obs}$ MRW/10cl

Where $[\theta]_{obs}$ is the ellipticity measured in millidegrees, MRW is the mean residue molecular weight of the peptide (molecular weight divided by the number of amino acid residues), c is the concentration of the sample in mg/mL, and l is the optical path length of the cell in centimeters.

Samples were measured using quartz plaques (0.2 mm spacing for solutions and 0.01 mm for gels) with 0.5 wt% solution concentrations with a pH range from 2-8. Gel concentrations measured ranged from 1.6-2.4 wt%. CD spectra were measured using a temperature range of 20-70 °C and a 5 °C step. The sample was equilibrated at each temperature for 2 minutes before measurements were recorded.

2.4.3 Cryogenic Transmission Electron Microscopy (Cryo-TEM)

Imaging was carried out in Finland by Jani Seitsonen, and Janne Ruokolainen, using a field emission cryo-electron microscope (JEOL JEM-3200FSC) operating at 200 kV.

Images were taken using bright-field mode and zero loss energy filtering (omega type) with a slit width of 20 eV. Micrographs were recorded using a CCD camera (Gatan Ultrascan 4000, USA). The specimen temperature was maintained at -187 °C during the imaging. Vitrified specimens were prepared using an automated FEI Vitrobot device using Quantifoil 3.5/1 holey carbon copper grids, with a 3.5 µm hole sizes. Grids were cleaned using a Gatan Solarus 9500 plasma cleaner just prior to use and then transferred into the environmental chamber of a FEI Vitrobot at room temperature and 100% humidity. Following this, 3 µL of sample solution at 0.5 wt % concentration was applied on the grid, blotted once for 1 s, and then vitrified in a 1:1 mixture of liquid ethane and propane at −180 °C. Grids with vitrified sample solutions were maintained in a liquid nitrogen atmosphere and then cryo-transferred into the microscope.

2.4.4 Transmission electron microscopy (TEM)

Imaging was performed using a 2100 plus TEM instrument. A thin film of peptide gel was added to the surface of a carbon film coated TEM grid and stained with 1 wt% uranyl acetate solution for 1 minute, followed by washing with distilled water by applying enough water to cover the grid and leaving it for 1 minute. The grids were then taken and placed in the TEM Instrument and images were taken, using a 4.0 megapixel CMOS camera, at various magnifications.

2.4.5 Polarized Optical Microscopy (POM)

Images were obtained with an Olympus BX41 polarized microscope by placing the sample between crossed polarizers. Approximately 20 µL of Congo red solution (450 µM) was added to gel samples and left for an hour to allow the Congo red solution to

absorb into the gels. The resulting mixtures were placed between a glass slide and a coverslip. Images were collected using an Olympus SP-350 digital camera.

2.4.6 Small-Angle X-ray Scattering (SAXS)

Solution SAXS experiments were performed on the bioSAXS beamline BM29 at the ESRF, Grenoble, France, and also on the bioSAXS beamline B21 at Diamond, Harwell, UK. Solutions containing 0.5 wt% of peptide in water were loaded into PCR tubes in an automated sample changer. At the ESRF, SAXS data were collected using a Pilatus 1 M detector. The sample−detector distance was 2.84 m. The X-ray wavelength was 0.99 Å. At Diamond, SAXS data was collected using a 2 M detector and at a fixed camera length of 3.9 m with a wavelength $\lambda = 1$ Å. The wavenumber $q = 4\pi \sin\theta / \lambda$ scale was calibrated using silver behenate, where λ is the x-ray wavelength and 2θ is the scattering angle. SAXS on hydrogels was performed at Diamond on beamlines I22 and B21. On I22, Samples were placed in DSC pans modified with mica or Teflon windows to enable transmission of the X-ray beam. The sample-to-SAXS detector distance was 7.483 m. A Pilatus P3-2M detector was used to acquire the 2D SAXS scattering patterns. SAXS data collected for samples with Teflon windows was corrected for the Teflon background scattering. Diffraction from silver behenate was used to calibrate the wavevector scale of the scattering curve. Data processing was performed using software DAWN (Data Analysis Software group, Diamond Light Source Ltd.). On beamline B21 at Diamond, samples were placed in custom made gel holder cells with Kapton (polyimide) windows. SAXS data was collected using a 2 M detector and at a fixed camera length of 3.9 m with a wavelength $\lambda = 1$ Å.

2.4.7 Fiber X-ray Diffraction (XRD)

XRD of gels (1.6-2.4 wt%) was performed on dried peptide stalks prepared by creating a fibre of peptide between the ends of wax coated capillaries. After separation of the capillaries after drying, a stalk was left on the end of one of the capillaries. Stalks were vertically mounted onto the goniometer of an Oxford Diffraction Gemini Ultra instrument, equipped with a Sapphire CCD detector. The sample to detector distance was 44 mm. The X-ray wavelength was $\lambda = 1.54$ Å. The wavenumber scale ($q = 4\pi \sin\theta/\lambda$ where 2θ is the scattering angle) was geometrically calculated.

2.4.8 Zeta Potential (ζ)

ζ potentials were measured using a Zetasizer Nano ZS from Malvern Instruments. A 1 mL aliquot of sample was placed inside a disposable folded capillary cell. The sample was left to equilibrate for 120 s before measuring the ζ potential, using an applied voltage of 50.0 V. The results presented are the average over three measurements.

2.4.9 pH titration measurement

Titrations were carried out using 2 wt% peptide solutions in water (3 mg in 150 µL). Sodium hydroxide (0.25 M) was added to the peptide solutions until pH 10 was reached. Titrations were performed by adding diluted HCl (0.022 M) dropwise, and measuring the pH using a pH meter until the pH had dropped to pH 2. Water was also titrated in the same way as a control experiment.

2.4.10 Nanodrop Concentration Determination

For gels, concentrations were measured using a Thermo Scientific NanoDrop 1000 spectrophotometer, and ND-1000 version 3.7 software. 2 µL of each sample was pipetted onto a cleaned measurement pedestal. The absorbance at 280 nm was recorded. A molar absorbance coefficient was calculated using the following equation,ε = (nW × 5500) + (nY × 1490) + (nC × 125). At 280 nm, this is the weighted sum of the 280 nm molar absorption coefficients of tryptophan (W), tyrosine (Y) and cysteine (C) amino acids. Given there are four tyrosine residues in each of the lipidated peptides this equation produces a molar absorbance coefficient of 5960 L mol^{-1} cm^{-1}. This absorbance and molar absorbance coefficient were then used to calculate the molarity using the Beer-Lambert equation. From the molarity the weight of peptide present was found and subsequently converted to a weight percent, using known volumes and molecular weights.

2.4.11 PYY11 Hydrogel Formation

Gels of PYY11 were prepared by making up 1-2 wt% peptide solutions in ultrapure water and changing the pH accordingly using 1 M HCl or 1 M NaOH. The solutions were heated to 60 °C for approximately 2 hours and then left to stand for a couple of hours to a couple of days for the gelation to occur. The concentration of gels was determined by Nanodrop experiments and ranged from 1.6-2.4 wt%. The pH range studied was pH 2-8.

2.5 References

1. Parker, S. L.; Balasubramaniam, A., Neuropeptide Y Y2 receptor in health and disease (vol 153, pg 420, 2007). *Brit J Pharmacol.* **2008**, 155 (8), 1307-1307.
2. de Lartigue, G., Role of the vagus nerve in the development and treatment of diet-induced obesity. *The Journal of physiology*. **2016**, 594 (20), 5791-5815.
3. Batterham, R. L.; Cohen, M. A.; Ellis, S. M.; Le Roux, C. W.; Withers, D. J.; Frost, G. S.; Ghatei, M. A.; Bloom, S. R., Inhibition of food intake in obese subjects by peptide YY3-36. *The New England journal of medicine.* **2003**, 349 (10), 941-8.
4. Batterham, R. L.; Bloom, S. R., The Gut Hormone Peptide YY Regulates Appetite. *Ann. Ny. Acad. Sci.* **2003**. 994, 162-168.
5. Degen, L.; Oesch, S.; Casanova, M.; Graf, S.; Ketterer, S.; Drewe, J.; Beglinger, C., Effect of peptide YY3-36 on food intake in humans. *Gastroenterology.* **2005**, 129 (5), 1430-6.
6. Parkinson, J. R.; Dhillo, W. S.; Small, C. J.; Chaudhri, O. B.; Bewick, G. A.; Pritchard, I.; Moore, S.; Ghatei, M. A.; Bloom, S. R., PYY3-36 injection in mice produces an acute anorexigenic effect followed by a delayed orexigenic effect not observed with other anorexigenic gut hormones. *American journal of physiology Endocrinology and metabolism.* **2008**, 294 (4), 698-708.
7. Ballantyne, G. H., Peptide YY(1-36) and Peptide YY(3-36): Part I. Distribution, Release and Actions. *Obes. Surg.* **2006**, 16 (5), 651-658.
8. Zhang, L.; Bulaj, G., Converting Peptides into Drug Leads by Lipidation. Curr. Med. Chem. **2012**, 19 (11), 1602-1618.
9. Hegefeld, W. A.; Kuczera, K.; Jas, G. S., Structural Dynamics of Neuropeptide hPYY. *Biopolymers.* **2011**, 95 (7), 487-502.
10. Henry, K. E.; Elfers, C. T.; Burke, R. M.; Chepurny, O. G.; Holz, G. G.; Blevins, J. E.; Roth, C. L.; Doyle, R. P., Vitamin B12 Conjugation of Peptide-YY3–36 Decreases Food Intake Compared to Native Peptide-YY3–36 Upon Subcutaneous Administration in Male Rats. *Endocrinology.* **2015**, 156 (5), 1739-1749.
11. Kalyanasundaram, K.; Thomas, J. K., Environmental Effects on Vibronic Band Intensities in Pyrene Monomer Fluorescence and their Application in Studies of Micellar Systems. *J. Am. Chem. Soc.* **1977**, 99 (7), 2039-2044.
12. Hamley, I. W.; Dehsorkhi, A.; Castelletto, V.; Walter, M. N. M.; Connon, C. J.; Reza, M.; Ruokolainen, J., Self-Assembly and Collagen-Stimulating Activity of a Peptide Amphiphile Incorporating a Peptide Sequence from Lumican. *Langmuir*. **2015**, 31 (15), 4490-4495.
13. Miravet, J. F.; Escuder, B.; Segarra-Maset, M. D.; Tena-Solsona, M.; Hamley, I. W.; Dehsorkhi, A.; Castelletto, V., Self-Assembly of a Peptide Amphiphile: Transition from Nanotape Fibrils to Micelles. *Soft Matter.* **2013**, 9 (13), 3558-3564.
14. Levine, H., Thioflavine-T Interaction with Synthetic Alzheimers-Disease Beta-Amyloid Peptides - Detection of Amyloid Aggregation in Solution. *Protein. Sci.* **1993**, 2 (3), 404-410.
15. Nilsson, M. R., Techniques to study amyloid fibril formation in vitro. *Methods* (San Diego, Calif.) **2004**, 34 (1), 151-60.

16. Castelletto, V.; Hamley, I. W., Self assembly of a model amphiphilic phenylalanine peptide/polyethylene glycol block copolymer in aqueous solution. *Biophysical chemistry.* **2009**, 141 (2-3), 169-74.
17. Biancalana, M.; Koide, S., Molecular mechanism of Thioflavin-T binding to amyloid fibrils. *Bba-Proteins Proteom.* **2010**, 1804 (7), 1405-1412.
18. Castelletto, V.; Gouveia, R. M.; Connon, C. J.; Hamley, I. W.; Seitsonen, J.; Nykanen, A.; Ruokolainen, J., Alanine-Rich Amphiphilic Peptide Containing the RGD Cell Adhesion Motif: A Coating Material for Human Fibroblast Attachment and Culture. *Biomater. Sci.* **2014**, 2 (3), 362-369.
19. Pace, C. N.; Grimsley, G. R.; Scholtz, J. M., Protein Ionizable Groups: pK Values and Their Contribution to Protein Stability and Solubility. *J. Biol. Chem.* **2009**, 284 (20), 13285-13289.
20. Isom, D. G.; Castaneda, C. A.; Cannon, B. R.; Garcia-Moreno, B., Large Shifts in pKa Values of Lysine Residues Buried Inside a Protein. *Proc Natl Acad Sci U S A.* **2011**, 108 (13), 5260-5.
21. Li, H.; Robertson, A. D.; Jensen, J. H., Very fast empirical prediction and rationalization of protein pKa values. *Proteins.* **2005**, 61 (4), 704-21.
22. Woody, R. W., Circular Dichroism of Peptides and Proteins. In Circular Dichroism: Principles and Applications, *Wiley, J., Ed. New York.* **1994**, 473-496.
23. Bulheller, B. M.; Rodger, A.; Hirst, J. D., Circular and linear dichroism of proteins. *Phys Chem Chem Phys*. **2007**, 9 (17), 2020-2035.
24. Nordén, B.; Rodger, A.; Dafforn, T. R., Linear Dichroism and Circular Dichroism: A Textbook on Polarized-Light Spectroscopy RSC: Cambridge, **2010**.
25. Cerpa, R.; Cohen, F. E.; Kuntz, I. D., Conformational Switching in Designed Peptides: The Helix/Sheet Transition. *Folding and Design.* **1996**, 1 (2), 91-101.
26. Su, J. Y.; Hodges, R. S.; Kay, C. M., Effect of Chain Length on the Formation and Stability of Synthetic a-Helical Coiled Coils. *Biochem.* **1994**, 33, 15501-15510.
27. Vandermeulen, G. W. M.; Tziatzios, C.; Klok, H.-A., Reversible Self-Organization of Poly(ethylene glycol)-Based Hybrid Block Copolymers Mediated by a De Novo Four-Stranded α-Helical Coiled Coil Motif. *Macromolecules.* **2003**, 36 (11), 4107-4114.
28. Bressler, I.; Kohlbrecher, J.; Thünemann, A. F., SASfit: A Tool for Small-Angle Scattering Data Analysis using a Library of Analytical Expressions. *J. Appl. Crystallogr.* **2015**, 48, 1587-1598.
29. Hartgerink, J. D.; Beniash, E.; Stupp, S. I., Peptide-amphiphile nanofibers: A versatile scaffold for the preparation of self-assembling materials. *P. Natl. Acad. Sci.* **2002**, 99 (8), 5133-5138.
30. Paramonov, S. E.; Jun, H. W.; Hartgerink, J. D., Self-assembly of peptide-amphiphile nanofibers: The roles of hydrogen bonding and amphiphilic packing. *J. Am. Chem. Soc.* **2006**, 128 (22), 7291-7298.
31. Rodriguez, L. M. D.; Hemar, Y.; Cornish, J.; Brimble, M. A., Structure-mechanical property correlations of hydrogel forming beta-sheet peptides. *Chem. Soc. Rev.* **2016**, 45 (17), 4797-4824.
32. Tang, C.; Ulijn, R. V.; Saiani, A., Effect of Glycine Substitution on Fmoc-Diphenylalanine Self-Assembly and Gelation Properties. *Langmuir.* **2011**, 27 (23), 14438-14449.

33. Adams, D. J.; Mullen, L. M.; Berta, M.; Chen, L.; Frith, W. J., Relationship Between Molecular Structure, Gelation Behaviour and Gel Properties of Fmoc- Dipeptides. *Soft Matter.* **2010**, 6 (9), 1971-1980.
34. Creighton, T. E., Proteins: Structures and Molecular Properties. W.H.Freeman & Co Ltd. **1986**.
35. Morris, K. L.; Serpell, L. C., X-ray fibre diffraction studies of amyloid fibrils. *Methods Mol Biol.* **2012**, 849, 121-35.
36. Hamley, I. W., Peptide fibrillization. *Angew Chem Int Edit*. **2007**, 46 (43), 8128-8147.
37. Howie, A. J.; Brewer, D. B.; Howell, D.; Jones, A. P., Physical basis of colors seen in Congo red-stained amyloid in polarized light. *Lab Invest.* **2008**, 88 (3), 232-242.
38. Howie, A. J.; Brewer, D. B., Optical properties of amyloid stained by Congo red: History and mechanisms. *Micron.* **2009**, 40 (3), 285-301.
39. Fazen, C. H.; Valentin, D.; Fairchild, T. J.; Doyle, R. P., Oral delivery of the appetite suppressing peptide hPYY(3-36) through the vitamin B12 uptake pathway. *J Med Chem*. **2011**, 54 (24), 8707-11.
40. Petrus, A. K.; Fairchild, T.J.;Doyle, R.P., Traveling the Vitamin B12 Pathway: Oral Delivery of Protein and Peptide Drugs. *Angewandte Chemie International Edition in English.* **2009**, 48, 1022-1028.

Chapter 3 - The Self-Assembly of Lipopeptides Containing Short Peptide Fragments Derived from the Gastrointestinal Hormone PYY_{3-36}: From Micelles to Amyloid Fibrils

3.1 Introduction

The self-assembly of three lipidated peptide fragments of the gastrointestinal peptide hormone PYY_{3-36} is studied in this chapter, and compared to the native fragments. Previous studies on various truncated versions of PYY have examined the Y2 receptor affinity and biological function, specifically at the C-terminus.[1] The self-assembly of truncated PYY peptides however has not been studied.

Here, we investigate the effect of pH, temperature, concentration, and lipidation on the self-assembly and conformation of three truncated fragments of PYY_{3-36}. The peptides studied consist of the first six and eight amino acid residues of the whole peptide sequence, with a palmitoyl alkyl chain covalently attached either at the N-terminus (IKPEAP and IKPEAPGE), or the C-terminus (PAEPKI) (Figure 3.1). Cytocompatibilty studies using MTT assays are also investigated to test cytotoxicity. The palmitoyl chain that is typically attached to the peptide is able to bind to serum albumin, causing steric hindrance, helping to delay proteolytic attack and renal clearance.[2, 3-5]

Studies have shown that PYY_{3-36} has a partially α-helical secondary structure.[6] The short peptide fragments studied here are not within the α-helical part of the whole sequence, and they also contain proline residues which are structure breaking residues that disfavour α-helix confirmations.[7] This occurs due to the disruption of hydrogen bonding

caused by the amide bond lacking the proton necessary for hydrogen bond stabilisation. Lipidation using palmitoyl (C_{16}, hexadecyl) chains is favourable, as it allows the molecule to fuse with the cell membrane and potentially act as a transducing molecule *in vivo*.[8]

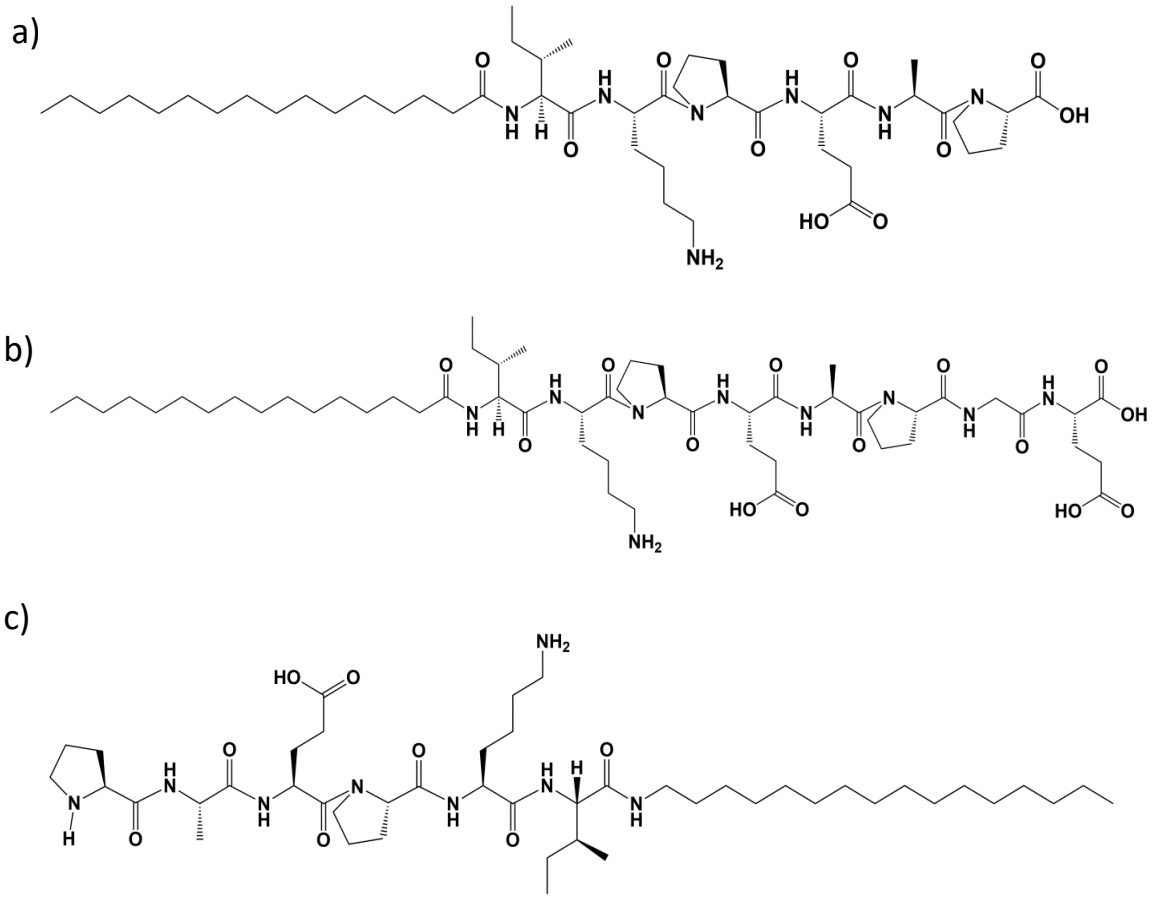

Figure 3.1. Chemical structures of a) C_{16}IKPEAP, b) C_{16}IKPEAPGE, and c) PAEPKI-NH-$C_{16}H_{33}$.

3.2 Results and Discussion

3.2.1 C_{16}IKPEAP and C_{16}IKPEAPGE

Fluorescence measurements using 8-anilinonaphthalene-1-sulfonic acid (ANS), and pyrene as fluorescent probes, were carried out to determine the critical micelle concentrations (cmc) of C_{16}IKPEAP and C_{16}IKPEAPGE. ANS interacts with hydrophobic binding sites to cause an increase in fluorescence and a blue shift of the $\lambda_{max.}$[9] Pyrene is also sensitive to the hydrophobic environment, and in the presence of micelles and other macromolecular systems, it becomes encapsulated in the interior hydrophobic regions of the aggregates.[10] Figure 3.2 shows results of ANS fluorescence measurements, and calculated critical micelle concentration (cmc) values were 0.0056 wt% and 0.0029 wt% for C_{16}IKPEAP and C_{16}IKPEAPGE respectively at their native pH in water. Results for the non-lipidated IKPEAP and IKPEAPGE did not show a distinct break in the intensity of fluorescence and it appears these peptides do not aggregate. Fluorescence experiments using pyrene were also carried out as a function of pH to investigate the effect of pH on aggregation concentration. Results indicate an increase in cmc with increased pH for both peptides (Figure 3.3 and Table 3.1). Interestingly there was no cmc observed for C_{16}IKPEAPGE at pH 12. It's not fully understood why this is, but it could be due to the negative charge caused by the additional glutamic acid residue affecting aggregation of the larger peptide at higher pH.

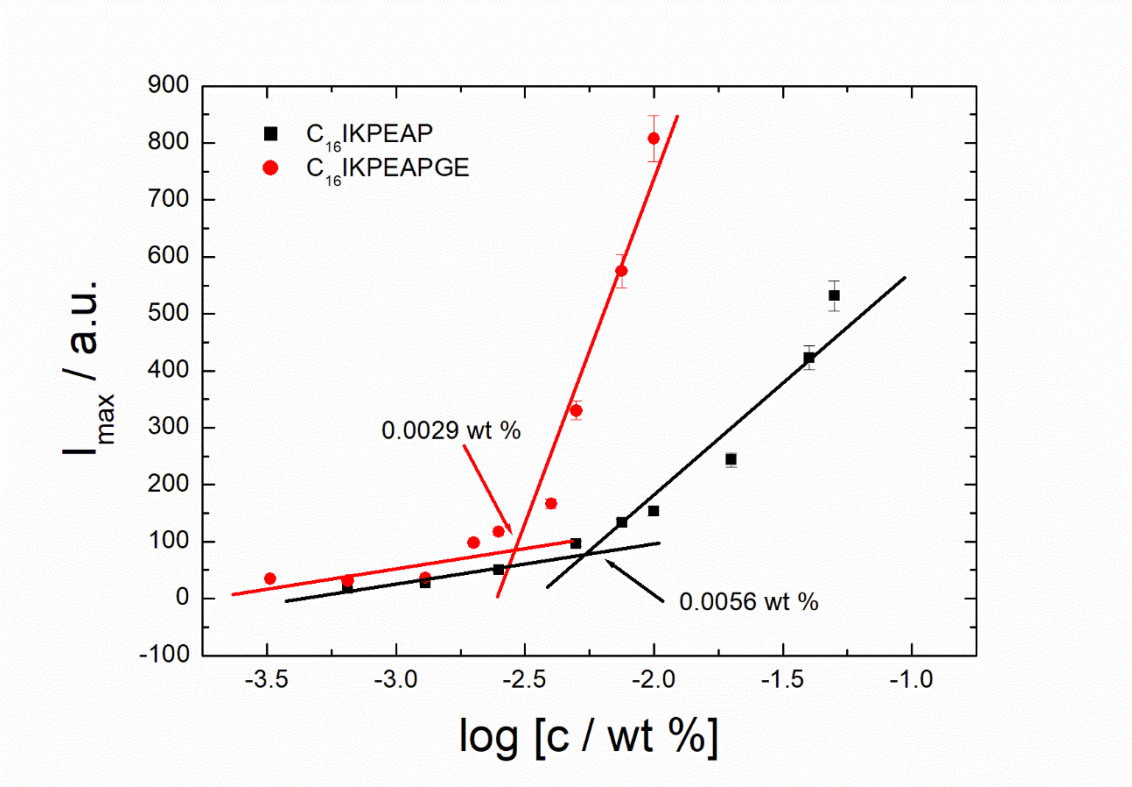

Figure 3.2. Concentration dependence of ANS I_{max} fluorescence to show the critical micelle concentration (cmc) of the lipidated peptides at their native pH in water. The intersection of the lines indicates the cac.

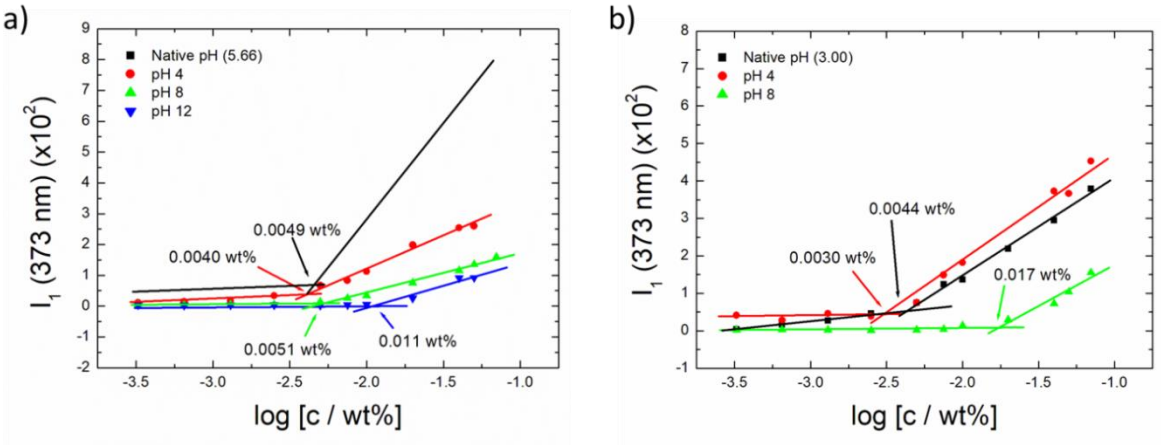

Figure 3.3. Concentration dependence of pyrene fluorescence I_1 (373 nm), at 20 ° C, to show pH dependence on the cmc of (a) C_{16}IKPEAP in the pH range 4-12 and (b) C_{16}IKPEAPGE in the pH range 2-8. The intersection of the lines defines the cmc.

Table 3.1. Tabulated critical aggregation concentration values of C_{16}IKPEAP and C_{16}IKPEAPGE in the pH range 2-12 and at 20 ^{o} C.

	C_{16}IKPEAP	**C_{16}IKPEAPGE**
Native pH (wt %)	0.0049	0.0044
pH 4 (wt %)	0.0040	0.0030
pH 8 (wt%)	0.0051	0.017
pH 12	0.011	-

Further fluorescence experiments were performed to investigate the interaction of the two lipidated peptide fragments with bovine serum albumin (BSA). Peptide concentrations well above the cmc were used, with BSA concentrations of 0.00375 wt%. Serum albumin accounts for around 60% of the total serum content in humans, making it the most abundant plasma protein for use in transportation of a wide variety of substrates such as hormones and metabolites.[11] The experiment carried out here was just a simple fluorescence experiment, to determine whether the peptide bound to BSA. Interestingly the peptide appeared to have auto-fluorescence with an emission wavelength of around 315 nm in the absence of BSA, which was surprising since the peptide does not contain any aromatic residues. The auto-fluorescence must therefore be due to the proline residues, which have been shown to auto-fluoresce with emission wavelengths ranging from 298-446 nm depending on the excitation wavelength.[12] Results show that there is a significant increase in intensity of both lipidated peptides in the presence of BSA, with a slight red shift to show a decrease in hydrophobicity,[13]

suggesting that the peptide has successfully bound to it (Figure 3.4). Further experiments are required to understand the binding interactions between the peptides and BSA however. These could include calculating the binding contant, K, and also using different concentrations of peptide and BSA.

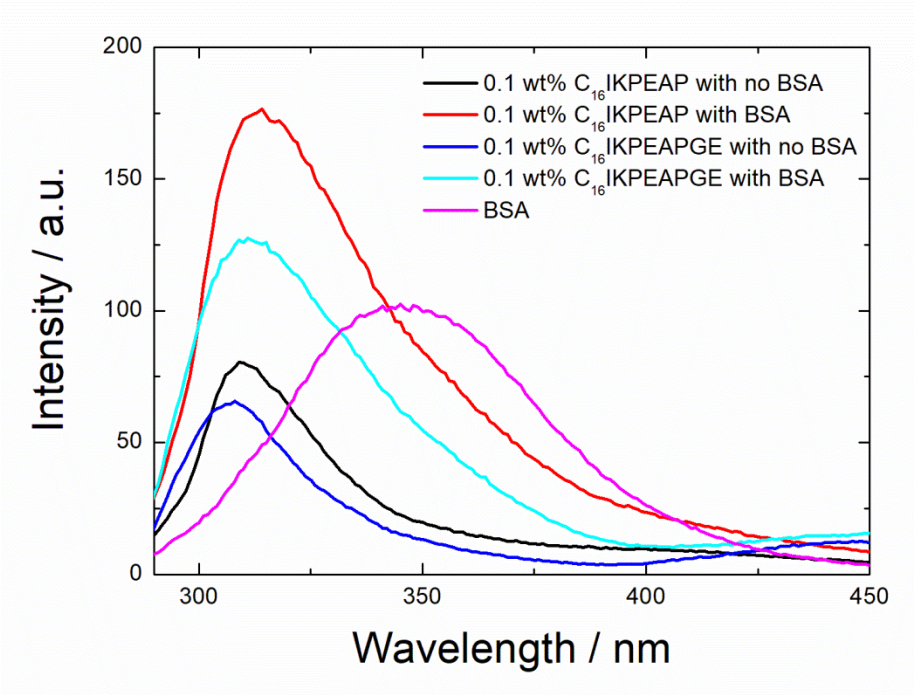

Figure 3.4. Fluorescence emission spectra to show bovine serum albumin binding of C_{16}IKPEAP, and C_{16}IKPEAPGE at 20 ° C.

Circular dichroism (CD) was used to determine secondary structure at concentrations above the cmc for the lipidated peptides. The same concentration of non-lipidated peptides were also used for comparison. Spectra of lipidated and unlipidated peptides were compared to determine what effect, if any, that the lipidation had on the secondary structure of the peptides. Spectra at the peptides native pH and 20 °C showed a disordered conformation for both C_{16}IKPEAP, and C_{16}IKPEAPGE, and a polyproline II helix for IKPEAP and IKPEAPGE, with positive molar ellipticity values near 220 nm [14-15]

(Figure 3.5). CD spectra at other pH values studied (pH 4-12) showed a disordered structure with minimum at around 195 nm at 20 ^{o}C (Figure 3.6).

Temperature ramp CD experiments to study thermal stability from 20-70 ^{o}C display similar results, shown in Figures 3.7-3.8. Lipidation enhances thermal stability at pH 4 since the lipidated peptides are much more thermally reversible when compared to the peptides themselves, shown by molar ellipticity values being more negative. Lipopeptide C_{16}IKPEAP at native pH (pH 6.28), and pH 8 appears to have very little secondary structure. This could be attributed to the measured pH values being close to the calculated isoelectric point which was found to be pH 6.86 for IKPEAP, whereas for IKPEAPGE it was pH 4.15, using Innovagen software.[16] The additional two residues; glutamic acid and glycine in the latter peptide lead to a substantial increase in peptide chirality, pointing to the important role of the charged terminal glutamic acid residue, since glycine is achiral. At pH 4 the molar ellipticity values are all fairly similar for all peptides, with the lipidated derivatives having a slight red shift. Results in the pH range 8-12 indicate that lipidation enhances the secondary structure of the larger peptide fragment, with molar ellipticity results 2 x 10^4 deg cm^2 dmol^{-1} more negative for the C_{16}IKPEAPGE fragment compared to IKPEAPGE.

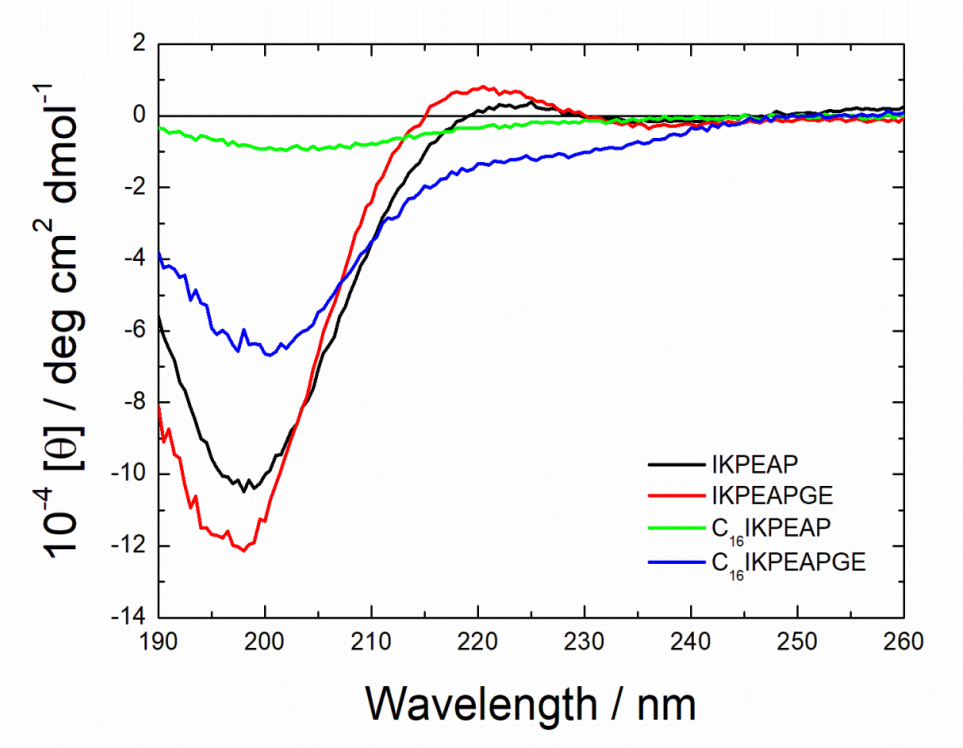

Figure 3.5. CD spectra comparing lipidated and unlipidated peptides at native pH and 20 °C.

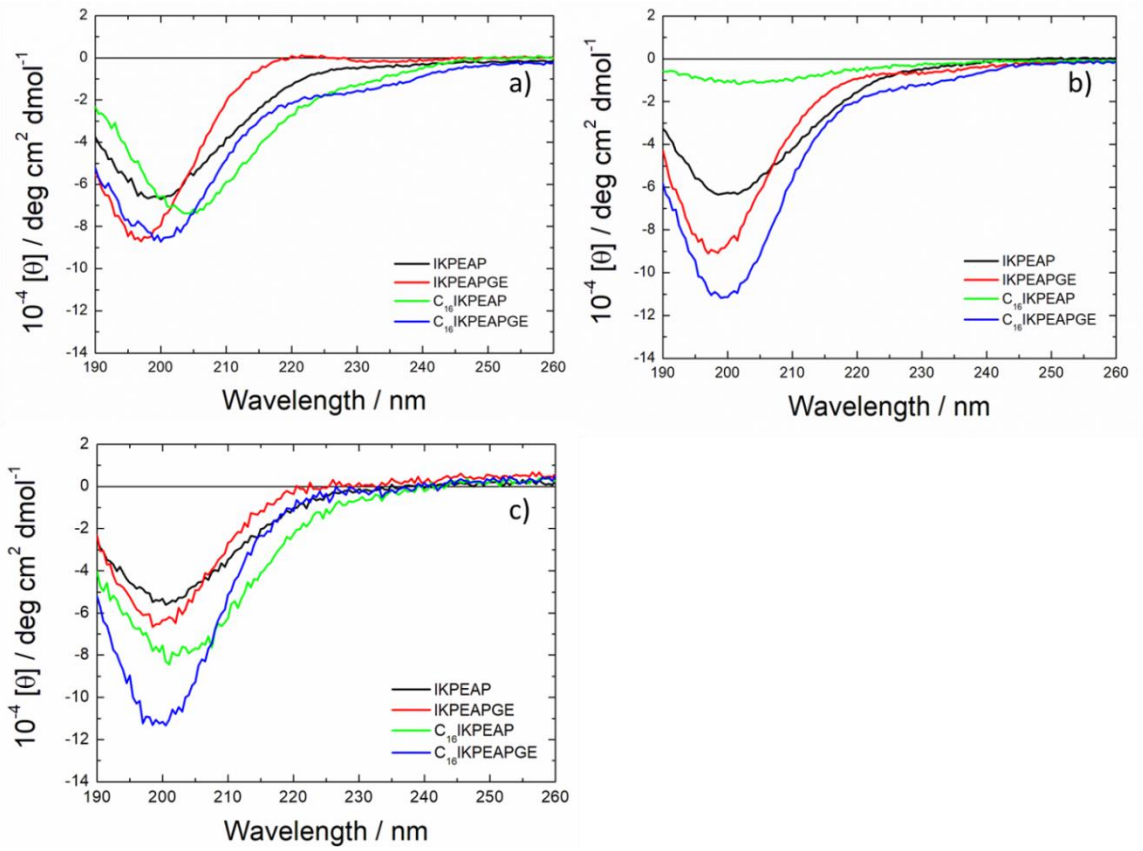

Figure 3.6. CD spectra comparing lipidated and unlipidated peptides at 20 °C. a) pH 4, b) pH 8, c) pH 12.

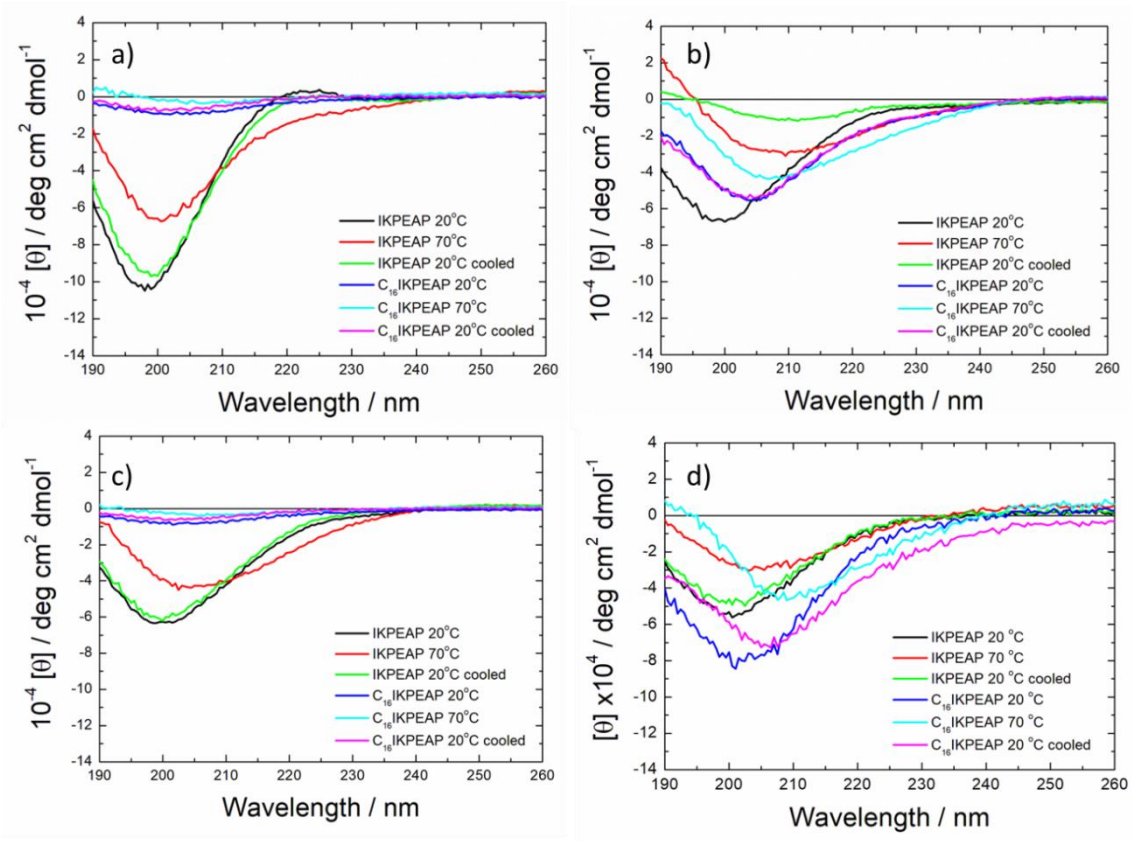

Figure 3.7. CD spectra showing thermal stability of C_{16}IKPEAP and IKPEAP from 20-70 °C. a) native pH of the peptide (pH 6.28 for C_{16}IKPEAP and pH 2.46 for IKPEAP), b) pH 4, c) pH 8, d) pH 12.

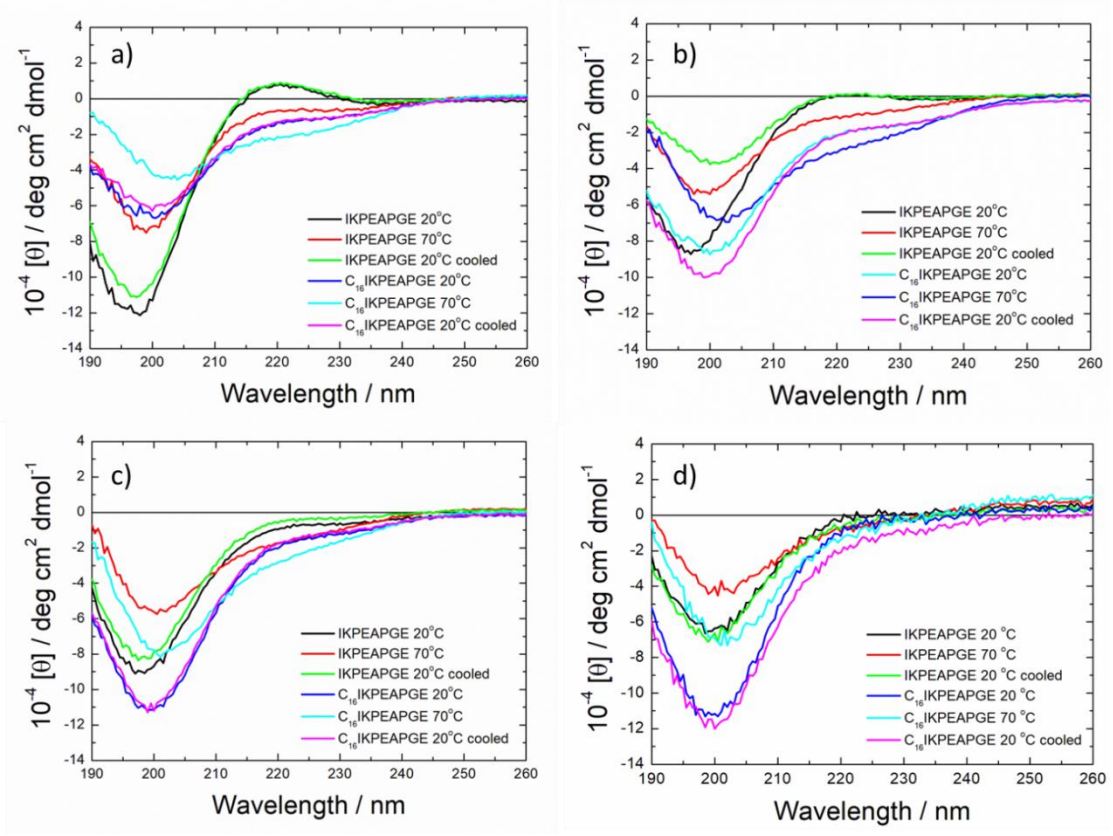

Figure 3.8. CD spectra showing thermal stability of C_{16}IKPEAPGE and IKPEAPGE from 20-70 °C. a) native pH of the peptide (pH 1.60 for C_{16}IKPEAPGE and pH 2.27 for IKPEAPGE), b) pH 4, c) pH 8, d) pH 12.

Cryogenic transmission electron microscopy (cryo-TEM) images of C_{16}IKPEAP and C_{16}IKPEAPGE showed the presence of micelles with a radius less than 5 nm (Figure 3.9). In contrast, cryo-TEM images of IKPEAP and IKPEAPGE showed no self-assembled structures at the same concentration (1 wt%). This is in agreement with the fluorescence probe measurements which revealed no cmc.

Dynamic light scattering (DLS) was used to provide an independent measure of the micelle size. The number weighted radius distributions at θ = 90° of the lipidated peptides are shown in Figure 3.10. The number weighted radius values were 1.90 nm

and 3.07 nm for C_{16}IKPEAP and C_{16}IKPEAPGE respectively which agreed with the cryo-TEM images that show the micelles to be less than 5 nm in radius.

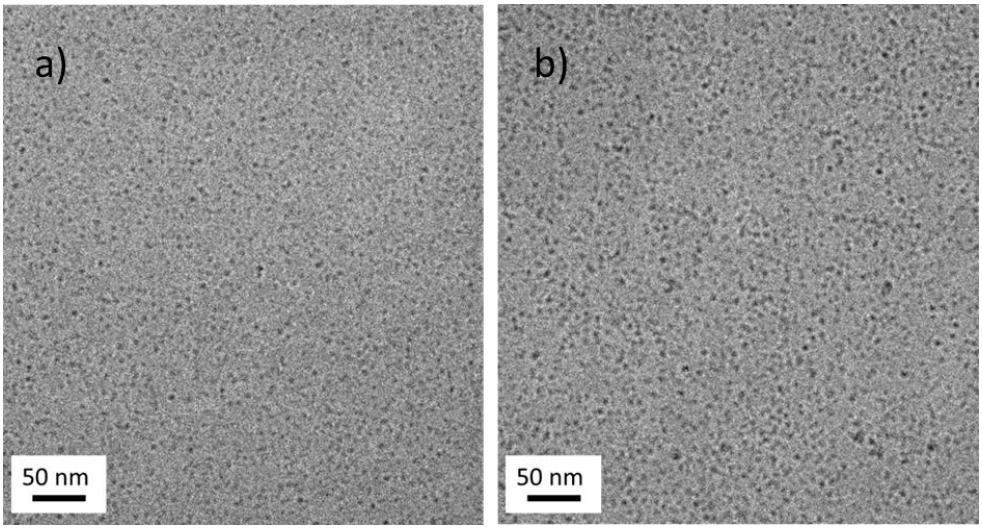

Figure 3.9. Cryo-TEM images obtained by J. Seitsonen and J. Ruokolainen, Finland, of: (i) C_{16}IKPEAP and (ii) C_{16}IKPEAPGE at native pH and 1 wt% showing micelles.

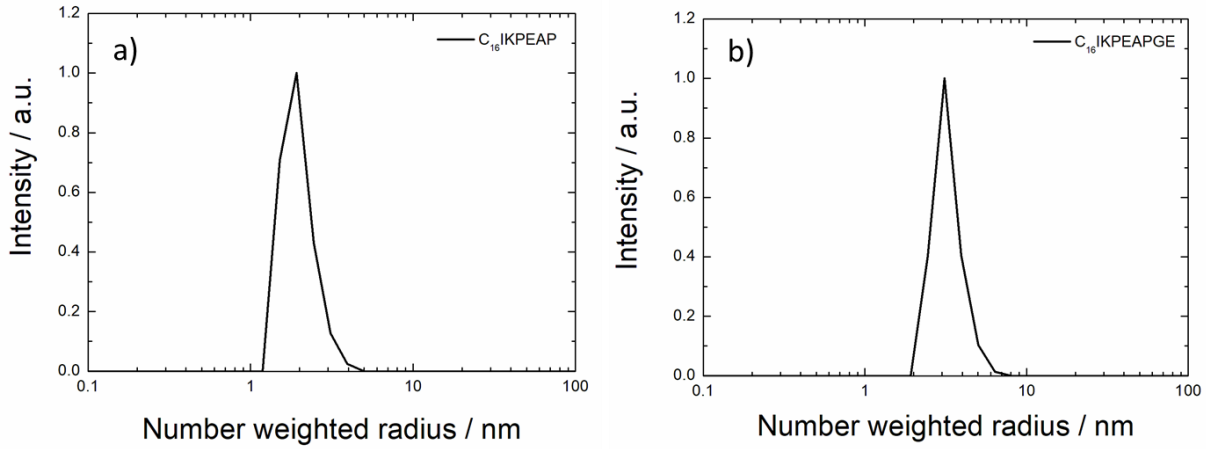

Figure 3.10. DLS intensity distributions showing the number weighted radius of C_{16}IKPEAP and C_{16}IKPEAPGE at native pH and 0.1 wt%

Small-angle X-ray scattering (SAXS) was used to further investigate the shape and size of the self-assembled peptide nanostructures in solution. The intensity profiles with model form factor fits of the lipidated peptide fragments are shown in Figure 3.11, and the fitted parameters are shown in Tables 3.2-3.3. The profiles of the lipidated fragments are consistent with the cryo-TEM images that showed spherical micelle structures, and the data can be fitted to a spherical shell form factor. The unlipidated fragments showed completely different shaped intensity profiles, and again were consistent with cryo-TEM images where there was no observable self-assembled structure. The SAXS data was fitted to a generalized Gaussian coil form factor to represent monomers in solution (Figure 3.12), and the fitted parameters are shown in Tables 3.4-3.5.

Ths SAXS data of the lipidated peptide fragments reveals differences in the outer radius of the micelles as a function of pH. Increasing the pH from 2 to 8 significantly decreases the radius for both peptide systems. This could be related to the loss of charge on the lysine residue at pH 8, causing an increase in net negative charge in the micelle, thus reducing the size. When comparing both lipidated peptides over pH 2-8, there are no obvious differences in the size of aggregates, suggesting that the length of the peptide does not affect the self-assembly behaviour, and that pH is the main contributing factor.

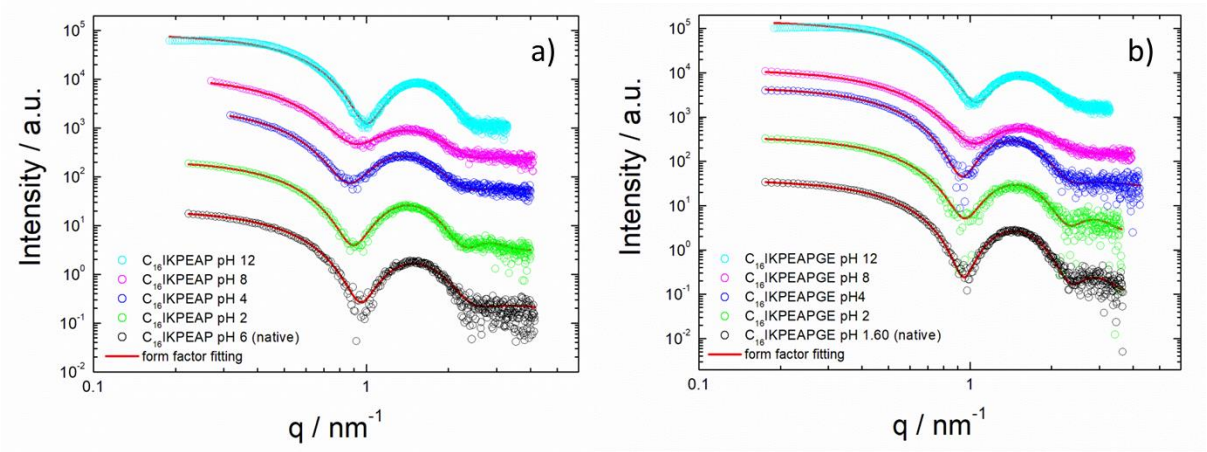

Figure 3.11. SAXS intensity profiles and form factor fits in the pH range 2-12. a) 0.134 wt% C_{16}IKPEAP, b) 0.162 wt% C_{16}IKPEAPGE. Data was fitted to a spherical shell form factor.

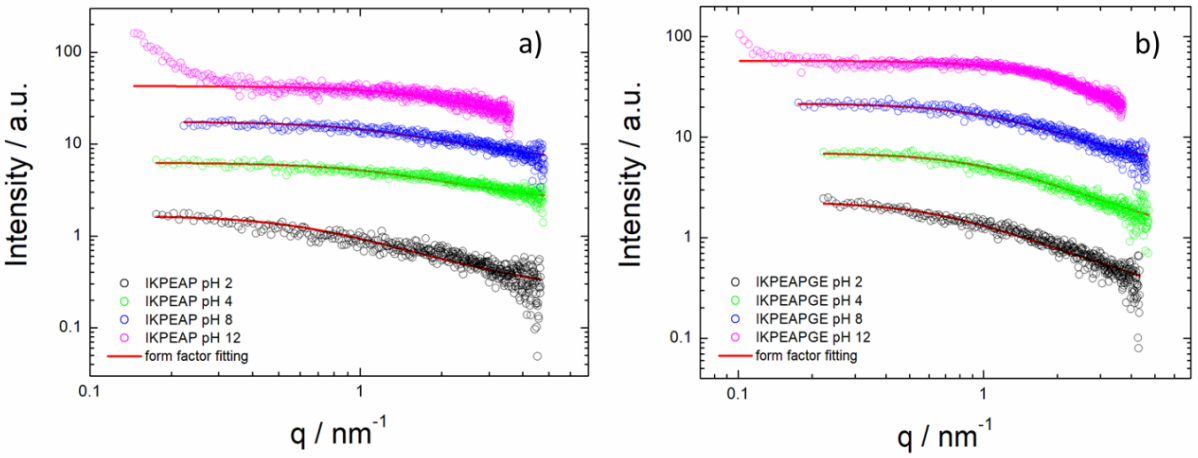

Figure 3.12. SAXS intensity profiles and form factor fits in the pH range 2-12. a) 0.13 wt% IKPEAP, b) 0.16 wt% IKPEAPGE. Peptides were fitted to a generalized Gaussian coil form factor.

Table 3.1. SAXS form factor parameters of C_{16}IKPEAP (0.134 wt%) at pH 2-8 fit to a spherical shell form factor model using SASfit.[17] Key: BG = background, *N*= scaling factor, σ = polydispersity in outer radius (Gaussian width), R_1= outer radius, R_2 = inner radius, μ = scattering contrast of the shell, η = scattering contrast of inner core.

Sample	BG	*N* / arb. units	σ/ nm	R_1 / nm	R_2 / nm	μ	η
C_{16}IKPEAP pH 2	0.310	0.604	0.486	3.26	1.91	-1.36	5.5×10^{-2}
C_{16}IKPEAP pH 4	0.525	0.602	0.713	3.24	1.76	-1.87	4.75×10^{-2}
C_{16}IKPEAP pH 6 (native pH)	0.200	0.554	0.535	3.24	1.60	-1.87	4.75×10^{-2}
C_{16}IKPEAP pH 8	0.776	1.04	0.926	2.67	1.66	-1.69	5.12×10^{-2}
C_{16}IKPEAP pH 12	1.41×10^{-3}	1.61×10^{-8}	3.78	31.82	16.09	-1.64	2.36×10^{-2}

Table 3.3. SAXS form factor parameters of C_{16}IKPEAPGE (0.162 wt%) at pH 2-8 fit to a spherical shell form factor model using SASfit.[17] Key as for Table 3.2.

Sample	BG	*N* / arb. units	σ/ nm	R_1 / nm	R_2 / nm	μ	η
C_{16}IKPEAPGE pH 2 (native pH)	0.266	1.01	0.535	3.18	1.88	-1.03	5.33×10^{-2}
C_{16}IKPEAPGE pH 4	0.281	1.00	0.566	3.39	1.72	-1.44	4.53×10^{-2}
C_{16}IKPEAPGE pH 8	0.500	1.17	0.861	2.71	1.51	-1.39	4.73×10^{-2}
C_{16}IKPEAPGE pH 12	1.6×10^{-3}	1.31×10^{-8}	4.59	32.16	15.15	-1.36	2.59×10^{-2}

Table 3.4. SAXS form factor parameters of IKPEAP at pH 2-8 fit to a generalized Gaussian coil form factor model[18] for which $\boldsymbol{R_g^2 = an^{2\nu}/(2\nu+1)(2\nu+2)}$ where *a* is the segment length, *n* is the chain length and *ν* is the Flory exponent) form factor model using SASfit.[17] Key: BG = background, *N*= scaling factor, R_g = radius of gyration, I_0 = forward scattering.

Sample	BG	*N* / arb. units	Rg/ nm	ν	I_0
IKPEAP pH 2 (native pH)	0.195	1.64	1.82	0.818	0.902
IKPEAP pH 4	0.605	1.33	1.02± 0.02	0.925± 0.03	1.12
IKPEAP pH 8	0.500	1.16	1.01± 0.02	0.912± 0.03	1.08
IKPEAP pH 12	1.9×10^{-3}	8.65×10^{-3}	7.75	0.248	0.276

Table 3.5. SAXS form factor parameters of IKPEAPGE at pH 2-8 fit to a generalized Gaussian coil form factor model using SASfit.[17] Parameters as for Table 3.4.

Sample	BG	*N* / arb. units	Rg/ nm	ν	I_0
IKPEAPGE pH 2 (native pH)	8.3×10^{-2}	2.19	1.70± 0.015	0.966	1.01± 0.015
IKPEAPGE pH 4	0.161	1.63	1.15	0.90	1.33
IKPEAPGE pH 8	0.275	1.57	1.10	0.903	1.21
IKPEAPGE pH 12	1.6×10^{-3}	1.2×10^{-2}	7.04	0.189	0.349

We unexpectedly noticed that drying samples for various measurements led to a profound difference in peptide conformation and self-assembled nanostructure. CD spectra measured on dried films show a β-sheet secondary structure for both peptides (Figure 3.13a). TEM images revealed the presence of short fibres with lengths of 400-500 nm (Figure 3.13b), showing that drying leads to disruption of the micelle structures present in solution, as revealed by cryo-TEM (Figure 3.9).

Fiber X-ray diffraction (XRD) was performed to directly examine secondary structure. The lipidated peptides have a β-sheet secondary structure with *d*-spacings of 4.68, 9.36, and 9.64 Å (Figure 3.13c). Results for the unlipidated fragments show a lack of secondary structure with *d*-spacing of 4.52 Å, representative of lipid chain packing (Figure 3.14).

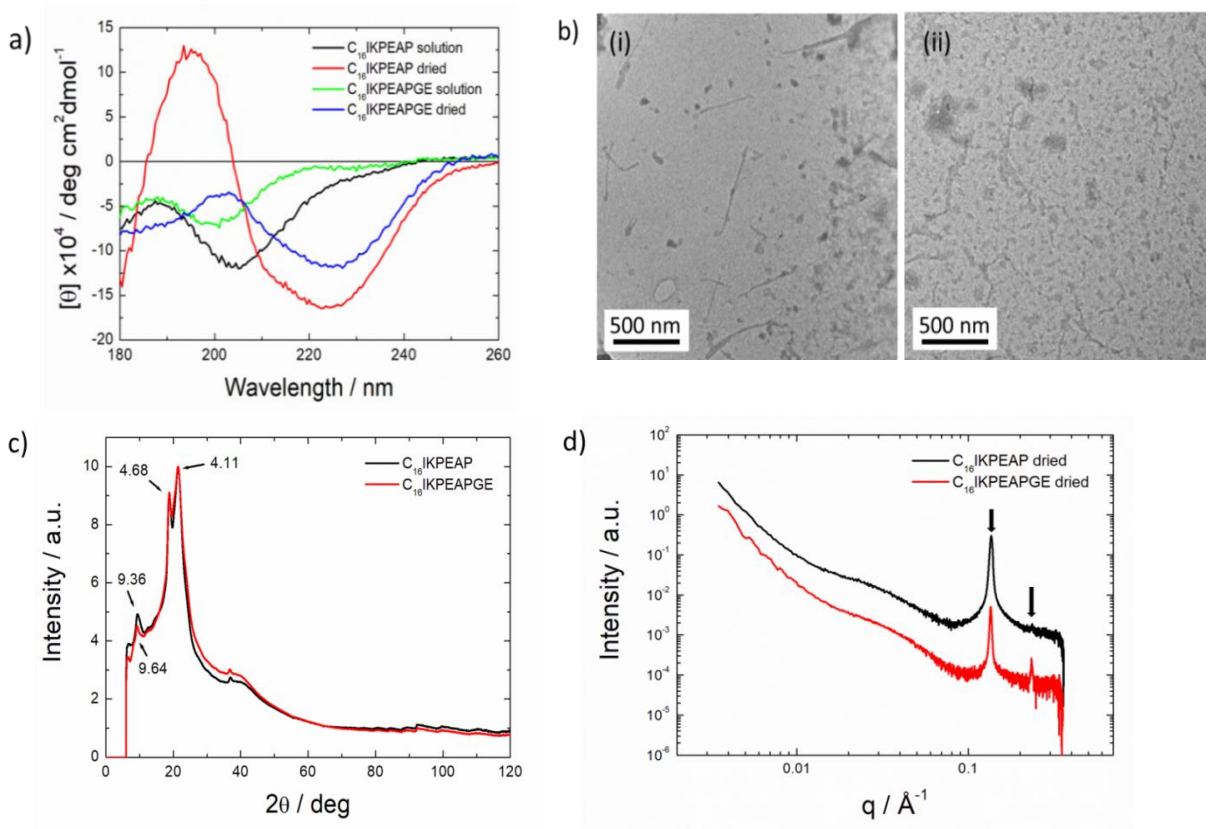

Figure 3.13. (a) CD spectra obtained from dried films. (b) TEM images of dried (i) C_{16}IKPEAP and (ii) C_{16}IKPEAPGE at native pH showing fibres and micelles.(c) Fibre X-ray diffraction intensity profile of C_{16}IKPEAP, and C_{16}IKPEAPGE at native pH. (d) SAXS intensity profiles of dried C_{16}IKPEAP, and C_{16}IKPEAPGE at native pH. Arrows shown highlight Bragg peaks.

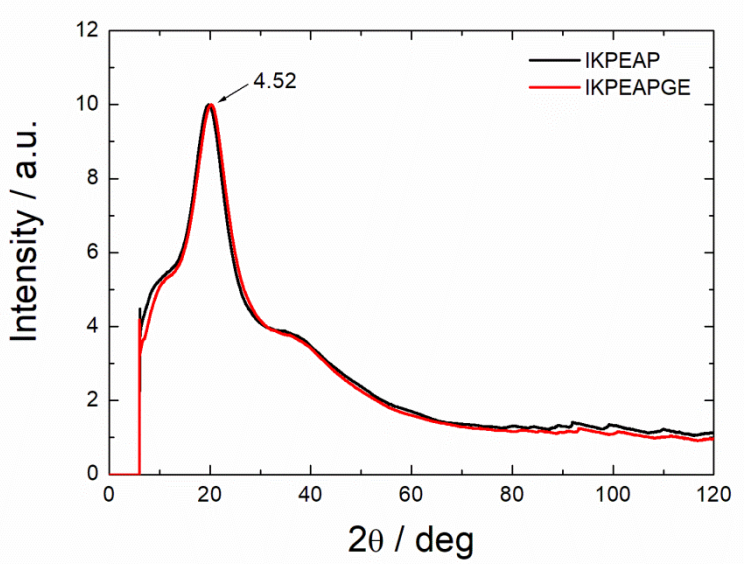

Figure 3.14. Fibre X-ray diffraction intensity profile of IKPEAP, and IKPEAPGE at native pH, showing a Bragg spacing of 4.52 Å.

3.2.2 PAEPKI-NH-$C_{16}H_{33}$

Further studies to look at the impact of lipidation at the C-terminus, by attachment of a palmitoyl amide group were investigated. This was to understand the effect of the lipidation site on self-assembly, but also to allow for the proline amino acid to be 'free', in the hope it acts as a catalyst in aldol reactions. Organocatalysts involving L-proline residues have been reported successfully as asymmetric catalysts for a wide range of synthetic reactions.[19-20] Of particular interest is L-proline derived organocatalysts containing long hydrophobic chains, as they have been found to perform aldol reactions in reaction mixtures containing both water and organic solvents.[21] Studies carried out on a lipidated peptide with a C_{16} palmitoyl chain attached at the C-terminus and a proline based head group (PRW-C_{16}), was found to be an excellent catalyst for aldol reactions performed in water, with very good stereoselectivity and conversion rates.[22] The lipidated peptide self-assembled into spherical micelles above a cmc, and the self-assembled structures were the driving force of the catalysis, since poor results were obtained in the absence of lipidated assembles. Other studies by Miravet et al. reported examples of aldol reactions catalyzed by L-proline-derived amphiphilic peptide gels based on self-assembled fibers.[23-24]

Aldol reactions combine two carbonyl compounds to form a new C-C bond, to produce a compound containing a β-hydroxy carbonyl group,[25-26] largely found in living organisms with exceptional pharmacological activities. Since the 1970s, L-proline has proven to be a very efficient organocatalyst for aldol reactions.[27] Many of the aldol reactions involving L-proline are carried out in organic solvents such as DMSO and chloroform which are harmful and environmentally unfavourable.[22] As a result, there

are current challenges to overcome this by replacing the solvents with more environmentally friendly ones, water being the most attractive one. The use of water is also attractive for promoting self-assembly by hydrophobic interactions and hydrogen bonding.

The peptide studied in this chapter is a truncated peptide fragment of PYY_{3-36}, with a palmitoyl chain (hexadecyl, C_{16}) attached to the peptide head group at the C-terminus. The peptide sequence is PAEPKI (the same sequence studied earlier in the chapter, but with the C_{16} chain attached at the C-terminus) (Figure 3.1c). Since C_{16}IKPEAP (N-terminal lipidation) was found to self-assemble into micelles and fibers depending on concentration, we first investigate the effect of the lipidation point (C-terminus versus N-terminus) on conformation and self-assembly. In collaboration with the group of W. Alves (UFABC, Brazil), the peptide's ability to serve as a catalyst for a model Aldol reaction was then studied, this being facilitated by the free N-terminal proline.

Firstly, the presence of a critical aggregation concentration (cac) to determine aggregation was carried out using ANS and pyrene as the fluorescent probes. Plots of Intensity as a function of concentration show distinct breaks at 1.73×10^{-3}, and 2.5×10^{-3} wt% at native pH (pH 3) and pH 8 respectively, suggesting that hydrophobicity decreases as the pH is increased (Figure 3.15). This is the same trend as what was seen for C_{16}IKPEAP, however the cac values of PAEPKI-NH-$C_{16}H_{33}$ are considerably lower than those found for C_{16}IKPEAP, implying that the 'free' proline residue increases the hydrophobicity of the peptide. ANS was unsuccessful when used at higher pH. It is not fully understood why, but it is thought to be due to the chemical structure of ANS

containing polar groups that become ionized with pH change, which reduces the ability of the peptide to bind to it as a result of charge repulsion.

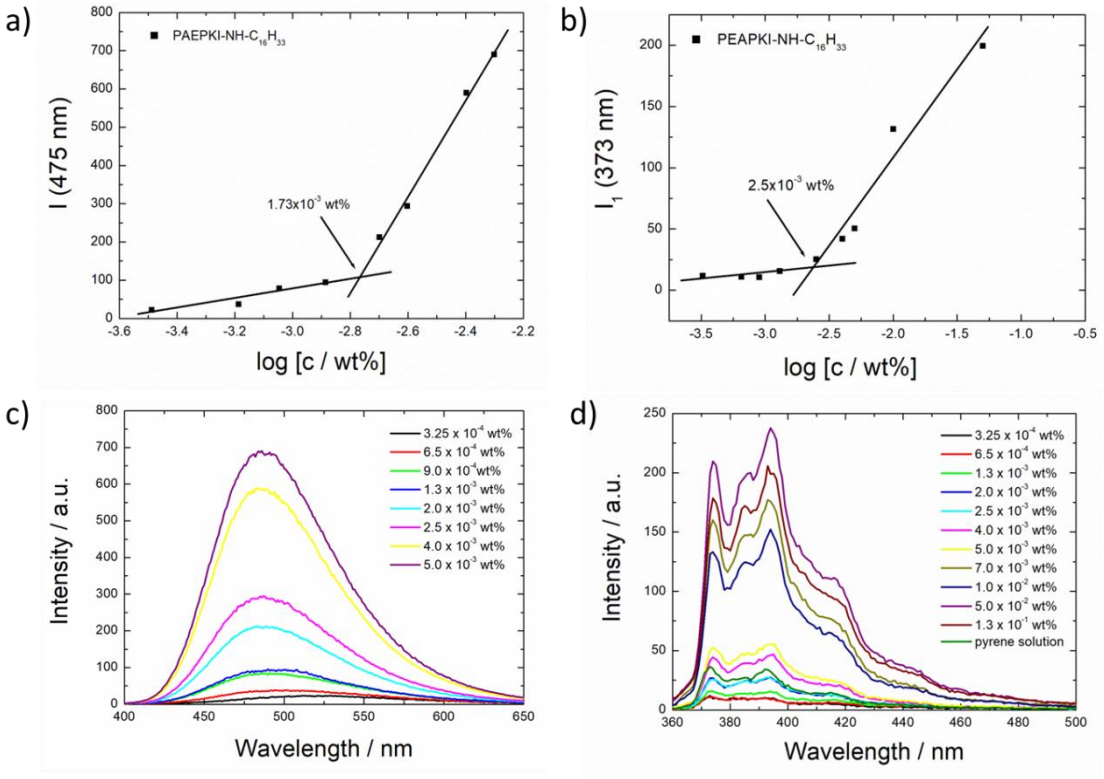

Figure 3.15. a) Concentration dependence of ANS I_{max} fluorescence to show the critical aggregation concentration (cac) of PAEPKI-NH-$C_{16}H_{33}$ at its native pH in ultrapure water (pH 3). The intersection of the lines indicates the cac. b) Concentration dependence of pyrene fluorescence I_1 (373 nm) of PAEPKI-NH-$C_{16}H_{33}$ at pH 8 to show pH dependence on the cac. c) Fluorescence emission spectra using ANS with PAEPKI-NH-$C_{16}H_{33}$ at native pH in ultrapure water. D) Fluorescence emission spectra using pyrene with PAEPKI-NH-$C_{16}H_{33}$ at pH 8.

CD experiments at native pH and pH 8 at 20 ^{o} C show a partial alpha helical content with two minima around 208 nm and 222 nm (Figure 3.16), that quickly transitions to a disordered structure with a minimum near 195 nm when the temperature is increased to 40 ^{o} C and above. This is contrast to C_{16}IKPEAP where a disordered structure is present throughout the temperature range studied. The results show that the peptide is partially thermally reversible after the first heating cycle, with molar ellipticity values becoming more negative when the temperature is cooled from 80 ^{o}C to 20 ^{o}C. This does not occur in the second cycle however, indicating peptide degradation after repeated heating. In comparison to lipidation at the N-terminus, this is a very interesting result because the N-terminal truncated peptide C_{16}IKPEAP is fully reversible after one heat cycle (Figure 3.7-3.8).

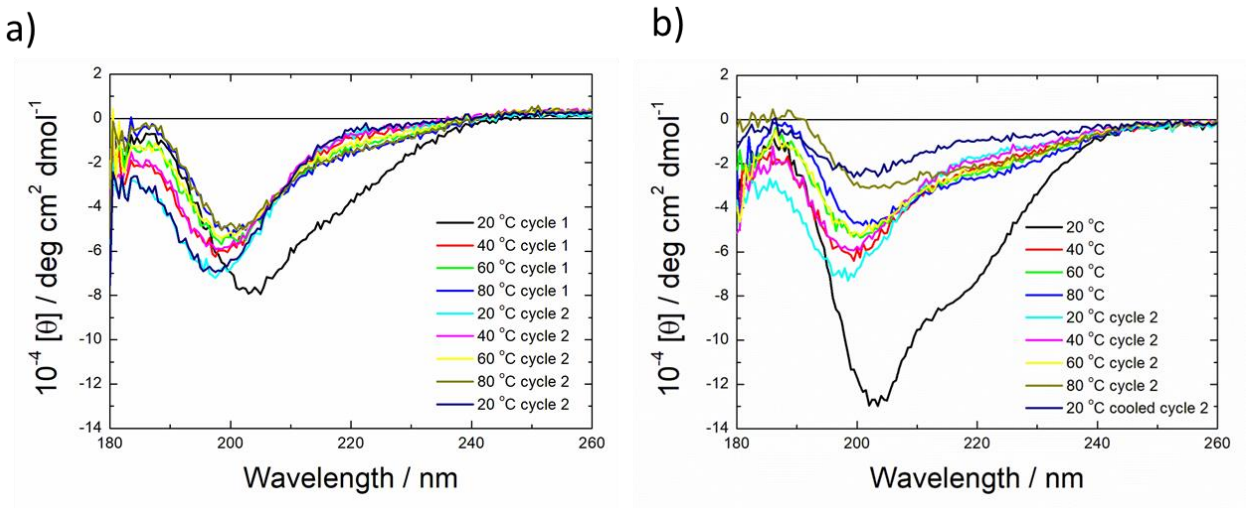

Figure 3.16. Temperature ramp CD of PAEPKI-NH-$C_{16}H_{33}$ with two temperature cycles from 20-80 ^{o} C. a) native pH, b) pH 8.

Cryo-TEM images show the presence of long inter-tangling fibers with lengths exceeding 500 nm (Figure 3.17a). Although cryo-TEM suggested a fiber morphology, the SAXS intensity profiles are more consistent with a micelle morphology, implying that the majority of the aggregates are micelles. Data was fitted to a spherical shell form factor fitting, and the fitted parameters are shown in Table 3.5. XRD was used to directly examine secondary structure, and results show a β-sheet structure with *d*-spacings of 4.67 Å (Figure 3.17c).

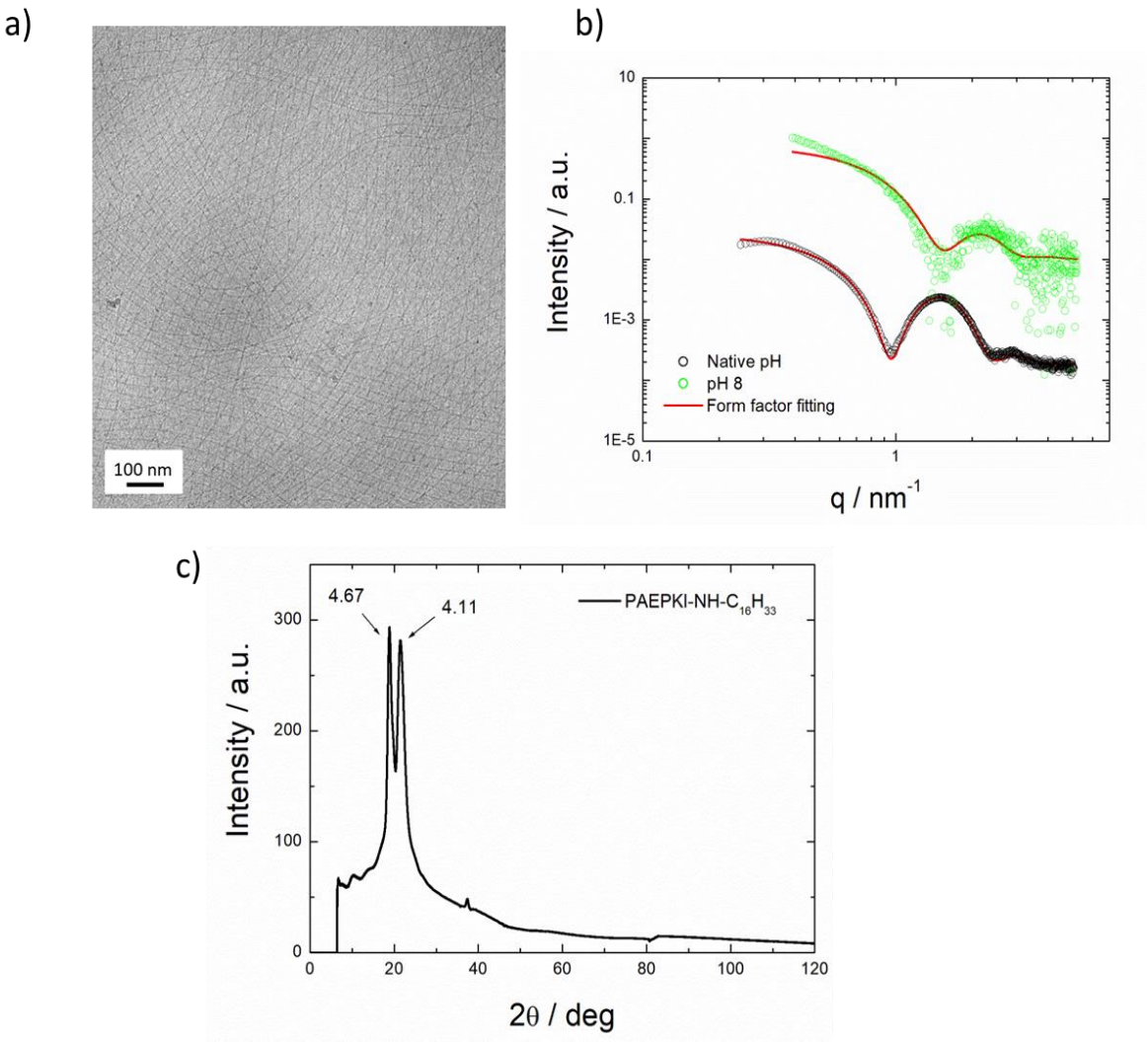

Figure 3.17. a) Cryo-TEM of C_{16}PAEPKI-NH-$C_{16}H_{33}$ at native pH (pH 3) showing a fiber morphology. b) SAXS intensity profiles of C_{16}PAEPKI-NH-$C_{16}H_{33}$ at native pH, and pH 8. Data was fitted to a spherical shell form factor to represent micelles. c) XRD of C_{16}PAEPKI-$C_{16}H_{33}$ with d-spacings of 4.67 Å representative of β-sheet secondary structure.

Table 3.5. SAXS form factor parameters of PAEPKI-NH-$C_{16}H_{33}$ at native pH (pH 3) and pH 8 fit to a spherical shell form factor model using SASfit. Key: BG = background, *N*= scaling factor, σ = polydispersity in

Sample	1 wt% PAEPKI-NH-$C_{16}H_{33}$ pH 3 (native pH)	1 wt% PAEPKI-NH-$C_{16}H_{33}$ pH 8
BG	$1.8x10^{-4}$	$1.0x10^{-3}$
N / arb. units	$2.73x10^{-4}$	$1.12x10^{-7}$
σ/ nm	0.42	5.36
R_1 / nm	3.29	34.52
R_2 / nm	1.75	20.06
μ	-1.44	-0.04
η	0.084	0.0047

3.2.3 Cytocompatibility studies using an MTT assay

Cytocompatibility studies of PAEPKI-NH-$C_{16}H_{33}$ were performed using an MTT ((3-(4,5-Dimethylthiazol-2-yl)-2,5-diphenyltetrazolium bromide) assay on human colorectal tumour cells (HCT-116 cell line), to determine cell viability (Figure 3.18-3.19). HCT-116 was chosen because it is a gastrointestinal cell line, and therefore of relevance to the peptide since it is released from the gut. MTT is a yellow tetrazole that becomes reduced by NADPH dependant oxidoreductase enzymes in living cells, to produce purple formazan crystals.[28-29] The crystals are then used to measure the number of viable cells using fluorescence spectroscopy.

The IC50 (half maximal inhibitory concentration) was found to be 2 x 10^{-3} wt% , which is very close to the cmc (Figure 3.18). Above this concentration, there is a significant decrease in cell proliferation, with only around 20 % of cells still viable. This suggests that the peptide becomes cytotoxic to the cells when it starts to aggregate. Further studies to look at a wider concentration range close to the cytotoxic concentration, would be useful in determining this is more detail. Furthermore it would be interesting to carry out work on a normal GI cell line to compare cytotoxicity.

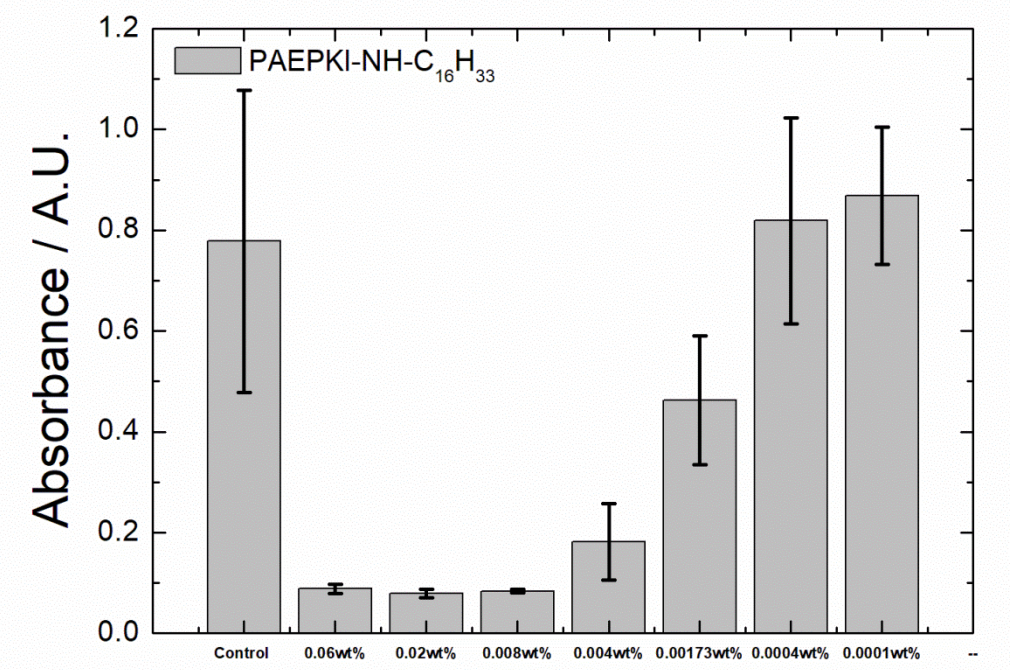

Figure 3.18. Cytocompatibility studies on PAEPKI-NH-$C_{16}H_{33}$ using an MTT assay on human colorectal tumour cells (HCT-116), using peptide concentrations above and below the cmc.

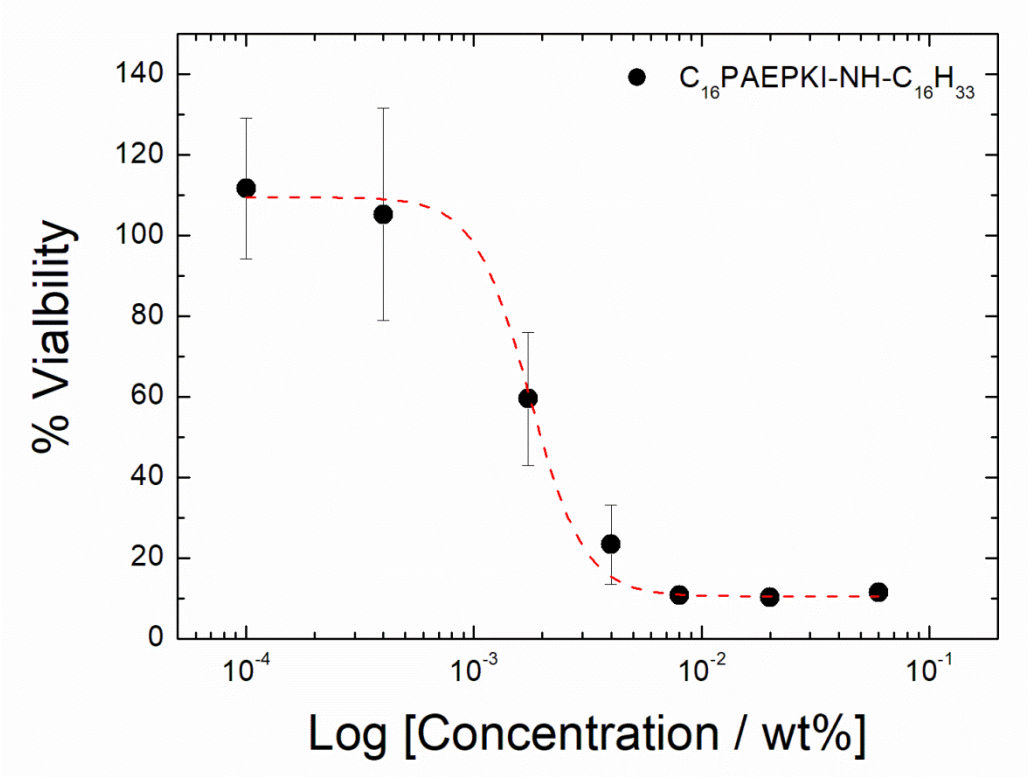

Figure 3.19. Cell viability as a function of peptide concentration of PAEPKI-NH-$C_{16}H_{33}$ on HCT-116 human colorectal tumour cells. The dashed red line is the sigmoidal fit of the data.

3.2.4 The use of PAEPKI-NH-$C_{16}H_{33}$ as an organocatalyst

The use of L-proline derived organocatalysts containing long hydrophobic chains for use in aldol reactions has shown considerable success.[21, 30-31] The high demand for more environmentally friendly processes makes L-proline derived organocatalysts somewhat favourable, since they have the ability to carry out reactions in solvent systems containing water as mentioned earlier in the chapter.

An investigation to understand the ability of PAEPKI-NH-$C_{16}H_{33}$ containing a "free" proline residue to act as a catalyst in aldol reactions between *p*-nitrobenzaldehyde and cyclohexanone were carried out by Juliane Pelin, Federal University of ABC, Brazil (scheme 3.1).

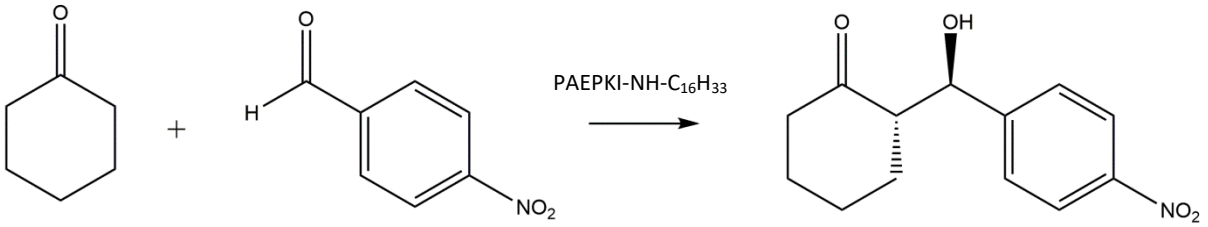

Scheme 3.1. Reaction mechanism to show the direct asymmetric aldol reaction of *p*-nitrobenzaldehyde and cyclohexanone, catalysed by an L-proline derived amphiphilic catalyst, PAEPKI-NH-$C_{16}H_{33}$, in the presence of water.

Experiments were carried out at room temperature with different excesses of water in relation to cyclohexanone. Results show that the peptide successfully acted as an organocatalyst in the reaction, but unfortunately as the excess of water was increased, the yield was reduced substantially from 56% to a mere 7.9% when there was a 2 molar equivalent of water. The reaction significantly favoured the anti-conformation as opposed to syn throughout the entire experiment, implying that steric hinderance reduced the ability of the syn-conformation (Table 3.6). Due to such low yields, the enantiomeric excess was not measured. Further studies are required in order to optimise the use of PAEPKI-NH-$C_{16}H_{33}$ as an organocatalyst in aldol reactions, with a particular focus on increasing the yield in the presence of water.

Table 3.6. Experimental results of the direct asymmetric aldol reaction of *p*-nitrobenzaldehyde and cyclohexanone using an L-proline derived amphiphilic catalyst.

Entry[a]	Conc. Cat. 1 (mol%)	Cyclohex. (eq.)	H_2O[b](eq.)	Yield[c](%)	*anti*:*syn*[c]	*ee* (%)
JP7	5	12	2.0	7.9	78:22	---
JP8	5	12	1.0	8.7	81:19	---
JP9	5	12	---	56	84:16	---

[a] The reactions were made at room temperature with vigorous stirring for 24 hours.

[b] Water excess in relation to cyclohexanone (v/v).

[c] The yield and diastereoselectivity were obtained by RMN-^{1}H analysis of the gross product.

3.3 Conclusion

In summary, adding a lipid tail to the N-terminus of the PYY_{3-36} peptide fragments drives self-assembly into micelles, above a critical micelle concentration. Fluorescence spectroscopy using ANS as the fluorescent probe revealed low cmc values. Interestingly no cmc was obtained for the unmodified peptides, suggesting that lipidation is the driving force of aggregation due to the increased amphiphilicity. Temperature-dependent measurements of the cmc show, unexpectedly, that micellization is essentially athermal showing that the process is driven by the favourable entropy change, associated with the hydrophobic effect as in protein folding. Further fluorescence studies using bovine serum albumin (BSA), showed that both lipidated peptide fragments interacted with BSA.

CD results showed the two N-terminal lipopeptides to have disordered conformations. Remarkably, C_{16}IKPEAP and C_{16}IKPEAPGE form β-sheet fibrils on drying, pointing to the formation of "amyloid-like" structures under these "denaturation" conditions. Possibly for lipopeptides as is proposed for proteins, amyloid may represent a common stable native state.[32]

SAXS and cryo-TEM showed a micelle morphology for both lipidated peptides throughout the pH range studied (pH 2-12). No aggregated structures were observed for the native peptides. SAXS data was fitted to a spherical shell form factor for the lipidated fragments, indicative of micelle morphology, and the unlipidated fragments were fitted to a generalized Gaussian coil form factor, representative of peptide monomers in solution. There are definitive differences in the outer radius values as a function of pH of the micelle structures. The micelle radius values at pH 8 were significantly smaller for both lipidated peptides than at the other pH values, and this could be related to the loss of charge on the lysine residue at pH 8, causing an increase in net negative charge in the micelle, therefore reducing the size. The dimensions obtained from SAXS form factor fits are very similar for both lipidated peptides at a given pH. Also the Gaussian coil form factor parameters for the two unlipidated peptides are similar when at the same pH. Both unlipidated peptides did not self-assemble into ordered aggregated nanostructures which suggests that the C_{16} lipid tail is the driving force behind self-assembly due to the increase in amphiphilicity in the peptide, causing hydrophobic collapse of the lipid tail to face away from the aqueous environment.

In a different direction, we investigated the utility of L-proline to act as a catalyst in the IKPEAP sequence, with lipidation at the C-terminus (PAEPKI-NH-$C_{16}H_{33}$). The peptide as

expected, self-assembled into micelles above a cmc. Fluorescence experiments using ANS and pyrene found the cmc to increase with increased pH, suggesting that the peptide becomes less hydrophobic as the pH is increased.

CD results interestingly showed a partial α-helical structure at 20 ^{o} C, which rapidly transitioned to a disordered structure when the temperature was raised above 40 ^{o} C. After two heat cycles it was found that PAEPKI-NH-$C_{16}H_{33}$ was only partially thermally reversible unlike C_{16}IKPEAP which was fully reversible, suggesting that lipidation at the C-terminus is less thermally stable than at the N-terminus. Similar to the N-terminal lipidated peptide (C_{16}IKPEAP), PAEPKI-NH-$C_{16}H_{33}$ SAXS data was fitted to a spherical shell form factor fitting, and XRD showed β-sheet structures. Unlike the N-terminal lipidated peptides, the radius values of PAEPKI-NH-$C_{16}H_{33}$ actually increase when increasing the pH to pH 8, further emphasizing the impact of lipidation position, as well as the 'free' proline residue on aggregation behaviour.

Cytocompatibility studies using MTT assays found PAEPKI-NH-$C_{16}H_{33}$ to be cytotoxic to HCT-116 colorectal tumour cells at values close to the cmc and above.

The use of PAEPKI-NH-$C_{16}H_{33}$ as an organocatalyst in aldol reactions was found to be moderately successful, with yields of 56% in the absence of water. Increasing the amount of water to the reaction vessel reduced the efficiency of the peptide catalyst significantly, with yields as low as 7.6%. Further experiments are required to optimise the use of PAEPKI-NH-$C_{16}H_{33}$ as a catalyst in the reaction.

Overall these findings are a promising starting point in understanding the self-assembly of the full PYY_{3-36} peptide sequence as a function of pH and temperature, in the development of a therapeutic agent to treat obesity and type II diabetes.

3.4 Materials and Methods

Materials. IKPEAP (TFA salt) was synthesised by Biomatik, Canada. The molecular weight by mass spectrometry was 653.8 $gmol^{-1}$ (expected: 653.37 $gmol^{-1}$) and the purity by HPLC was 99.8 %.

IKPEAPGE (TFA salt) was synthesised by Biomatik, Canada. The molecular weight by mass spectrometry was 839.98 $gmol^{-1}$ (expected: 839.44 $gmol^{-1}$) and the purity by HPLC was 99.7 %.

C_{16}IKPEAP (ammonium acetate salt) was synthesised by Peptide Synthetics, UK. The molecular weight by mass spectrometry was 892.179 $gmol^{-1}$ (expected: 891.60 $gmol^{-1}$) and the purity by HPLC was > 95.0 %.

C_{16}IKPEAPGE (ammonium acetate salt) was synthesised by Peptide Synthetics, UK. The molecular weight by mass spectrometry was 1078.346 $gmol^{-1}$ (expected: 1077.67 $gmol^{-1}$), and the purity by HPLC was > 95.0 %.

PAEPKI-NH-$C_{16}H_{33}$ (TFA) was synthesised by Peptide Synthetics, UK. The molecular weight by mass spectrometry was 877.204 $gmol^{-1}$ (expected: 876.64 $gmol^{-1}$) and the purity by HPLC was > 95.0 %.

Methods

Fluorescence Spectroscopy. Fluorescence spectra were recorded with a Varian Cary Eclipse fluorescence spectrometer (Varian IEEE-488, Australia) with samples in 4 mm inner quartz cuvettes. The ANS assays were performed using 3.25 x 10^{-4} to 0.13 wt% peptide, in 2.1 x 10^{-3} wt% 8-anilino-1-napthalenesulfonic acid (ANS) solution. The samples were excited at λ_{ex} = 356 nm, and the fluorescence emission was measured for λ = 400−670 nm. Pyrene assays were performed using 3.25 x10^{-4} to 0.13 wt% peptide, in 2.167 x 10^{-5} wt % pyrene solution. The samples were excited at λ_{ex} = 339 nm, and the fluorescence emission was measured for λ = 360−500 nm.

Temperature-dependent fluorescence assays of cmc were carried out using the same method but a temperature controlled water bath was also used and measurements were collected in the temperature range 20-70 ^{o}C.

Circular Dichroism (CD). CD spectra were recorded using a Chirascan spectropolarimeter (Applied Photophysics, UK). Spectra are presented with absorbance A < 2 at any measured point with a 0.5 nm step, 1 nm bandwidth, and a 1 s collection time per step. The CD signal from the background was subtracted from the CD signal of the sample solution. Ellipticity is reported as the mean residue ellipticity ([ϑ], in deg cm^2 dmol^{-1}) and calculated as:

$$[\vartheta] = [\vartheta]_{obs}\, MRW/10cl$$

Where $[\vartheta]_{obs}$ is the ellipticity measured in millidegrees, MRW is the mean residue molecular weight of the peptide (molecular weight divided by the number of amino acid

residues), *c* is the concentration of the sample in mg/mL, and *l* is the optical path length of the cell in centimeters.

CD spectra were measured in the temperature range 20-70 ^{o}C, using a 10 ^{o}C temperature step. Samples were equilibrated at each temperature for 2 minutes before measurements were recorded. Quartz plaques (0.1 and 0.01 mm thick) were used for the experiments and a pH range of 2-12 was measured. 0.1-1 wt% samples were used. Experiments were carried out in D_2O. CD spectra were also measured on dried peptides using quartz plates (0.01 mm).

Small-Angle X-ray Scattering (SAXS). Solution and dried SAXS experiments were performed on the bioSAXS beamline BM29 at the ESRF, Grenoble, France, and the bioSAXS beamline B21 at Diamond light source, U.K. Solutions containing 0.162-1 wt% C_{16}IKPEAPGE and IKPEPAGE, and 0.134-1 wt% of C_{16}IKPEAP and IKPEAP were loaded in PCR tubes in an automated sample changer. SAXS data were collected using a Pilatus 1 M detector. The sample−detector distance was 2.84 m. The X-ray wavelength was 0.99 Å. The wavenumber $q = 4\pi \sin\theta / \lambda$ scale was calibrated using silver behenate, where λ is the x-ray wavelength and 2θ is the scattering angle. Dried SAXS measurements were performed by drying the peptides onto Kapton tape, and inserting them into a gel cell. Data was collected using a Pilatus 2M detector at a fixed camera length of 3.9 m with a wavelength λ= 1 Å. The wavenumber $q = 4\pi \sin\theta / \lambda$ scale was calibrated using silver behenate, where λ is the x-ray wavelength and 2θ is the scattering angle.

Fiber X-ray Diffraction (XRD). XRD was performed on peptide stalks prepared by drawing a fibre of peptide solution between the ends of wax-coated capillaries. 3 wt% peptide solutions were used for IKPEAP and IKPEAPGE, and 5 wt% peptide solutions for

C_{16}IKPEAP and C_{16}IKPEAPGE. After drying, the capillaries were separated and a stalk was left on the end of one of the capillaries. Stalks were vertically mounted onto the goniometer of an Oxford Diffraction Gemini Ultra instrument, equipped with a Sapphire CCD detector. The sample to detector distance was 44 mm. The X-ray wavelength was λ = 1.54 Å. The wavenumber scale ($q = 4\pi \sin\theta/\lambda$ where 2θ is the scattering angle) was geometrically calculated. The software CLEARER[33] was used to reduce the 2D data to a one dimensional intensity profile.

Dynamic Light Scattering (DLS). Experiments were performed using an ALV CGS-3 system with a 5003 multidigital correlator. The light source was a 20 mW HeNe laser, linearly polarized, with λ = 633 nm. Samples were filtered through 0.20 μm Anotop organic membrane filters from Whatman into standard 0.5 cm diameter cylindrical glass cells.

Cryogenic Transmission Electron Microscopy (Cryo-TEM). Imaging was carried out using a field emission cryo-electron microscope (JEOL JEM-3200FSC) operating at 200 kV. Images were taken using bright-field mode and zero loss energy filtering (omega type) with a slit width of 20 eV. Micrographs were recorded using a CCD camera (Gatan Ultrascan 4000, USA). The specimen temperature was maintained at -187 ^{o}C during the imaging. Vitrified specimens were prepared using an automated FEI Vitrobot device using Quantifoil 3.5/1 holey carbon copper grids, with a 3.5 μm hole sizes. Grids were cleaned using a Gatan Solarus 9500 plasma cleaner just prior to use and then transferred into the environmental chamber of a FEI Vitrobot at room temperature and 100% humidity. Following this, 3 μL of sample solution at 1 wt % concentration was applied on the grid, blotted once for 1 s, and then vitrified in a 1/1 mixture of liquid ethane and

propane at −180 °C. Grids with vitrified sample solutions were maintained in a liquid nitrogen atmosphere and then cryo-transferred into the microscope.

Transmission Electron Microscopy (TEM). Imaging of dried films was performed using a 2100 plus TEM instrument. A thin film of peptide was added (0.134 wt% of C_{16}IKPEAP and 0.162 wt% C_{16}IKPEAPGE) to the surface of a carbon film coated TEM grid and stained with 1 wt% uranyl acetate solution for 1 minute, followed by washing with distilled water by, applying enough water to cover the grid and leaving it for 1 minute. The grids were then taken and placed in the TEM Instrument and images were taken, using a 4.0 megapixel CMOS camera, at various magnifications.

Cytocompatibility studies using an MTT assay. The cytotoxicity of PAEPKI-NH-$C_{16}H_{33}$ was examined. In vitro cell culture was carried out using the HCT-116 human colorectal tumour cell line. Cells were cultured in MCcoys 5A modified medium with with 10% fetal bovine serum (FBS), and 1% antibiotic-antimycotic (Thermoscientific, 100×). Cells were maintained in a humidified atmosphere of 5% CO_2 at 37 °C. Cell viability effects were examined using the MTT 3-(4,5- dimethylthiazol-2-yl)-2,5-diphenyltetrazolium bromide) assay. The peptide was dissolved in complete medium. Cells were seeded into a 96-well plate at a seeding density of 4×10^4 cells/mL, and allowed to adhere for 24 h in 100 µL complete medium. After 24 h, a total volume of 100 µL of either complete medium and/or peptide solution was added, to give final peptide concentrations of 0.06, 0.02, 0.008, 0.00173, 0.004, 0.0008 or 0.0004wt % peptide. Negative controls of peptide in complete medium with no cells were included. After 67 h of incubation, 20 µL of MTT (0.5 wt % in PBS) was added to each well plate and allowed to incubate for 5 h (total of 72 h incubation). After this, the solutions were removed from the wells and replaced

with 100 µL DMSO per well in order to dissolve the formazan crystals. Plates were incubated for 30 min, and then analyzed using a UV microplate reader (λ = 570 nm). Results are reported [(treated cells − negative control)/(untreated cells)] × 100.

Aldol reactions in water. Cyclohexanone (0.9 mmol, 90 µL) was added to the peptide catalyst (3.6 µmol, 3.2 mg), varying the amount of water (170 µL, 85 µL, and 0 µL). *p*-nitrobenzaldehyde (72.7 µmol, 10.3 mg) was added the reaction mixture was stirred at room temperature for 24 hours, before being extracted with ethyl acetate four times. For the experiment containing no water, 0.5 mL of water was added to the system before extracting, to help in the phase separation. NMR measurements in (^{1}H) Bruker Ultrashield 300 was performed in 300 MHz, using the deuterated chloroform solvent. The yield and diastereomers *anti:syn* ratio were calculated using the NMR spectrum obtained, where tetramethylsilane (TMS) was used as a reference.

^{1}H NMR (300 MHz, $CDCl_3$): δ 8.22-8.18 (m, 2H, ArH); 7.51-7.47 (m, 2H, ArH); 5.47 (br s, 1H, C*H*OH-*syn*); 4.89 (dd, *J* = 7.5 Hz, 3.0 Hz, 1H, C*H*OH-*anti*); 4.08 (d, *J* = 3.0 Hz, 1H, CHO*H*-*anti*); 2.66-2.30 (m, 1H, C*H*CHOH); 2.66-2.30 (m, 2H, $CH_2C(O)$); 2.16-1.24 (m, 6H, chex-H).

3.5 References

1. Ehrlich, G. K.; Michel, H.; Truitt, T.; Riboulet, W.; Pop-Damkov, P.; Goelzer, P.; Hainzl, D.; Qureshi, F.; Lueckel, B.; Danho, W.; Conde-Knape, K.; Konkar, A., Preparation and Characterization of Albumin Conjugates of a Truncated Peptide YY Analogue for Half-Life Extension. Bioconjugate Chem **2013,** 24 (12), 2015-2024.
2. Hutchinson, J. A.; Burholt, S.; Hamley, I. W., Peptide Hormones and Lipopeptides: From Self-Assembly to Therapeutic Applications. J. Pept. Sci. **2017,** 23, 82-94.
3. Li, Y.; Shao, M. X.; Zheng, X. M.; Kong, W. L.; Zhang, J. N.; Gong, M., Self-Assembling Peptides Improve the Stability of Glucagon-like Peptide-1 by Forming a Stable and Sustained Complex. Mol. Pharm. **2013,** 10 (9), 3356-3365.
4. Gao, Z. H.; Bai, G.; Chen, J. Q.; Zhang, Q.; Pan, P. W.; Bai, F.; Geng, P., Development, Characterization, and Evaluation of a Fusion Protein of a Novel Glucagon-Like Peptide-1 (GLP-1) Analog and Human Serum Albumin in Pichia pastoris. Biosci Biotech Bioch **2009,** 73 (3), 688-694.
5. Wang, Y.; Lomakin, A.; Kanai, S.; Alex, R.; Benedek, G. B., Transformation of Oligomers of Lipidated Peptide Induced by Change in pH. Mol. Pharm. **2015,** 12 (2), 411-419.
6. Lerch, M.; Mayrhofer, M.; Zerbe, O., Structural similarities of micelle-bound peptide YY (PYY) and neuropeptide Y (NPY) are related to their affinity profiles at the Y receptors. J Mol Biol **2004,** 339 (5), 1153-1168.
7. T. E. Creighton, W. H. F., Proteins: Structures and Molecular Properties Federation of European Biochemical Societies **1993,** 323 (3), 294-301.
8. Brunsveld, L.; Waldmann, H.; Huster, D., Membrane binding of lipidated Ras peptides and proteins - The structural point of view. Bba-Biomembranes **2009,** 1788 (1), 273-288.
9. Hawe, A.; Sutter, M.; Jiskoot, W., Extrinsic Fluorescent Dyes as Tools for Protein Characterization. Pharmaceutical Research **2008,** 25 (7), 1487-99.
10. Kalyanasundaram, K.; Thomas, J. K., Environmental Effects on Vibronic Band Intensities in Pyrene Monomer Fluorescence and their Application in Studies of Micellar Systems. J. Am. Chem. Soc. **1977,** 99 (7), 2039-2044.
11. Togashi, D. M.; Ryder, A. G., A Fluorescence Analysis of ANS Bound to Bovine Serum Albumin: Binding Properties Revisited by Using Energy Transfer. J Fluoresc **2008,** 18 (2), 519-526.
12. Niyangoda, C.; Miti, T.; Breydo, L.; Uversky, V.; Muschol, M., Carbonyl-based blue autofluorescence of proteins and amino acids. Plos One **2017,** 12 (5), e0176983.
13. Yang, G.-D.; Li, C.; Zeng, A.-G.; Zhao, Y.; Yang, R.; Bian, X.-L., Fluorescence spectroscopy of osthole binding to human serum albumin. Journal of Pharmaceutical Analysis **2013,** 3 (3), 200-204.
14. Castelletto, V.; Hamley, I. W.; Cenker, C.; Olsson, U.; Adamcik, J.; Mezzenga, R.; Miravet, J. F.; Escuder, B.; Rodriguez-Llansola, F., Influence of End-Capping on the Self-Assembly of Model Amyloid Peptide Fragments. J Phys Chem B **2011,** 115 (9), 2107-2116.
15. Paramonov, S. E.; Jun, H. W.; Hartgerink, J. D., Self-assembly of peptide-amphiphile nanofibers: The roles of hydrogen bonding and amphiphilic packing. J. Am. Chem. Soc. **2006,** 128 (22), 7291-7298.

16. Innovagen Peptide property calculator. http://pepcalc.com/.Accessed 05.01.19.
17. Bressler, I.; Kohlbrecher, J.; Thünemann, A. F., SASfit: A Tool for Small-Angle Scattering Data Analysis using a Library of Analytical Expressions. J. Appl. Crystallogr. **2015,** 48, 1587-1598.
18. Hammouda, B., Form Factors for Branched Polymers with Excluded Volume. J. Res. Natl. Inst. Stand. Technol. **2016,** 121, 139-164.
19. Hernandez, J. G.; Juaristi, E., Recent efforts directed to the development of more sustainable asymmetric organocatalysis. Chem Commun **2012,** 48 (44), 5396-5409.
20. Mukherjee, S.; Yang, J. W.; Hoffmann, S.; List, B., Asymmetric Enamine Catalysis. Chem Rev **2007,** 107 (12), 5471-5569.
21. Zhong, L.; Gao, Q.; Gao, J. B.; Xiao, J. L.; Li, C., Direct catalytic asymmetric aldol reactions on chiral catalysts assembled in the interface of emulsion droplets. J Catal **2007,** 250 (2), 360-364.
22. Soares, B. M.; Aguilar, A. M.; Silva, E. R.; Coutinho-Neto, M. D.; Hamley, I. W.; Reza, M.; Ruokolainen, J.; Alves, W. A., Chiral organocatalysts based on lipopeptide micelles for aldol reactions in water. Phys Chem Chem Phys **2017,** 19 (2), 1181-1189.
23. Rodríguez-Llansola, F.; Miravet, J. F.; Escuder, B., Supramolecular Catalysis with Extended Aggregates and Gels: Inversion of Stereoselectivity Caused by Self-Assembly. Chemistry – A European Journal **2010,** 16 (28), 8480-8486.
24. Berdugo, C.; Escuder, B.; Miravet, J. F., Structural insight into the aggregation of l-prolyl dipeptides and its effect on organocatalytic performance. Organic & Biomolecular Chemistry **2015,** 13 (2), 592-600.
25. Hiersemann, M., Modern Aldol Reactions. Synthesis **2007,** 2007 (03), 483-483.
26. List, B.; Lerner, R. A.; Barbas, C. F., Proline-catalyzed direct asymmetric aldol reactions. J. Am. Chem. Soc. **2000,** 122 (10), 2395-2396.
27. Pidathala, C.; Hoang, L.; Vignola, N.; List, B., Direct catalytic asymmetric enolexo aldolizations. Angew Chem Int Edit **2003,** 42 (24), 2785-2788.
28. Stockert, J. C.; Horobin, R. W.; Colombo, L. L.; Blazquez-Castro, A., Tetrazolium salts and formazan products in Cell Biology: Viability assessment, fluorescence imaging, and labeling perspectives. Acta Histochem **2018,** 120 (3), 159-167.
29. Berridge, M. V.; Herst, P. M.; Tan, A. S., Tetrazolium dyes as tools in cell biology: new insights into their cellular reduction. Biotechnology annual review **2005,** 11, 127-52.
30. Zhao, Q.; Lam, Y.-h.; Kheirabadi, M.; Xu, C.; Houk, K. N.; Schafmeister, C. E., Hydrophobic substituent effects on proline catalysis of aldol reactions in water. The Journal of organic chemistry **2012,** 77 (10), 4784-4792.
31. Mase, N.; Nakai, Y.; Ohara, N.; Yoda, H.; Takabe, K.; Tanaka, F.; Barbas, C. F., Organocatalytic Direct Asymmetric Aldol Reactions in Water. J. Am. Chem. Soc. **2006,** 128 (3), 734-735.
32. Baldwin, A. J.; Knowles, T. P. J.; Tartaglia, G. G.; Fitzpatrick, A. W.; Devlin, G. L.; Shammas, S. L.; Waudby, C. A.; Mossuto, M. F.; Meehan, S.; Gras, S. L.; Christodoulou, J.; Anthony-Cahill, S. J.; Barker, P. D.; Vendruscolo, M.; Dobson, C. M., Metastability of Native Proteins and the Phenomenon of Amyloid Formation. J. Am. Chem. Soc. **2011,** 133 (36), 14160-14163.

33. Makin, O. S.; Sikorski, P.; Serpell, L. C., CLEARER: a new tool for the analysis of X-ray fibre diffraction patterns and diffraction simulation from atomic structural models. J. Appl. Crystallogr. **2007,** 40, 966-972.

Chapter 4 - The Effect of Lipidation on the Self-Assembly of a Truncated Peptide Fragment Derived from the Gut Hormone PYY_{3-36}

4.1 Introduction

The use of short peptides in the treatment of disease is very attractive due to relative ease of synthesis and cost in comparison to larger peptide therapeutics.[1] Truncated peptide fragments provide a cost effective way of investigating peptide behaviour, and to study isolated sections in more detail, to fully understand important aspects such as self-assembly, binding affinity, and bioactivity. In one example, Kumar et al. found that a truncated pentapeptide had a higher affinity for a Casitas B-Lineage Lymphoma (Cbl) tyrosine kinase binding domain than the parent peptide.[2] Another study by Swedberg et al. discovered that a C-terminal truncation of exendin-4, with removal of the nine C-terminal residues, had little effect on cAMP signalling when compared to the native peptide.[3] Exendin-4 is an exogenous GLP-1R agonist with a similar pharmacological profile to GLP-1, and therefore of relevance here since it is a gut hormone, similar to PYY_{3-36}.

In this chapter the self-assembly of another truncated fragment derived from PYY_{3-36} is investigated. PYY_{3-36} is known to have a predominant alpha-helical secondary structure in solution, and aggregates into long inter-tangling fibres at its native pH in water.[4] The peptide sequence studied here lies within the β-turn and α-helical section, making it

very interesting in terms of its self-assembly and aggregation behaviour. The full peptide sequence of PYY_{3-36} is shown in Figure 4.1a, with the peptide to be studied, EELNRYY, highlighted in red. The effect of palmitoyl lipidation at the N-terminus is also examined in order to determine the impact of increased amphiphilicity on self-assembly and stability. Furthermore, gelation properties are investigated, and cytocompatibility studies are carried out using the HCT-116 cancer cell line. The amino acid sequence of the lipidated and native peptide fragments, along with their chemical structures, are shown in Figure 4.1.

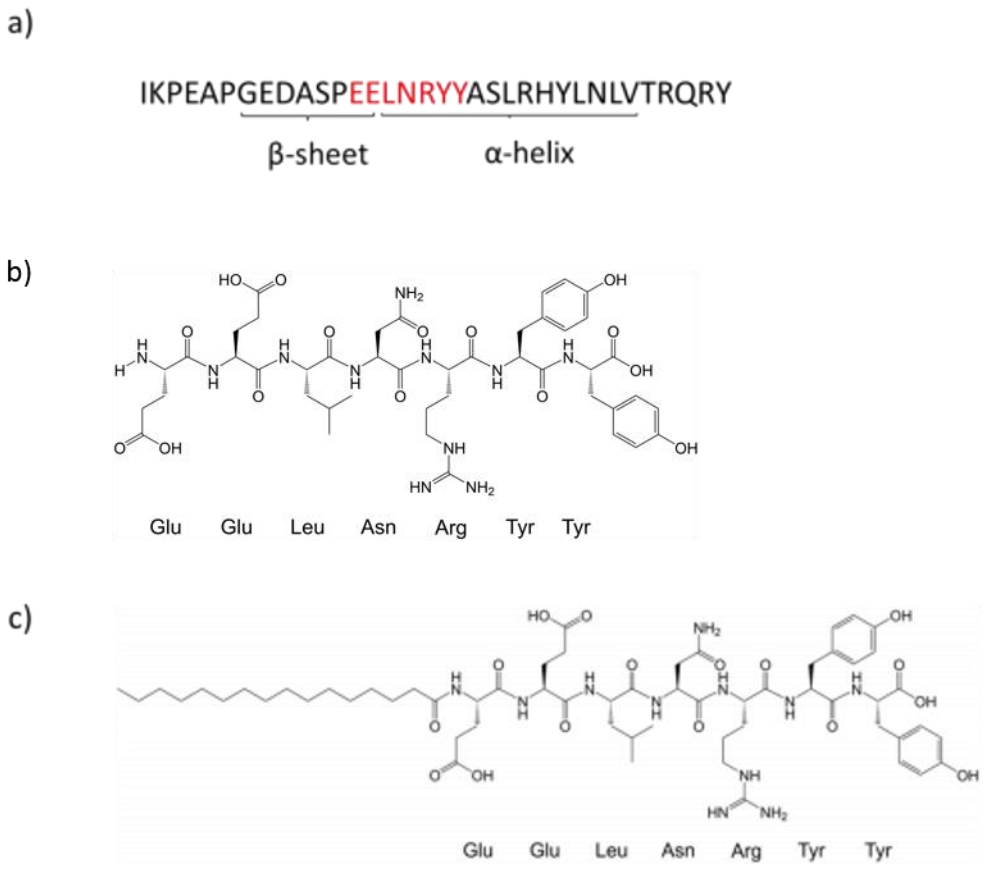

Figure 4.1. a) Amino acid sequence and chemical structure of PYY_{3-36}, showing the different domains, and highlighting EELNRYY. b) Amino acid sequence and chemical structure of EELNRYY. c) Amino acid sequence and chemical structure of C_{16}EELNRYY.

4.2 Results and Discussion

The presence of a critical aggregation concentration (cac) was firstly investigated using pyrene as a fluorescent probe. As previously mentioned, pyrene has been used a number of times to detect the cac of peptides and amphiphilic molecules.[5-6] A plot of the I_1 (373 nm) intensity versus concentration was used to assign the cac, with the I_1 peak corresponding to the first vibronic band of pyrene. Results indicate an increase in cac with increased pH, with values of 0.0034 wt%, 0.046 wt% and 0.15 wt% at pH 7, 10, and 12 respectively for C_{16}EELNRYY (Figure 4.2). The increase in cac with pH indicates reduced hydrophobicity at pH 12 due to tyrosinate ions being present at high pH. No cac was observed for the unlipidated peptide fragment itself, demonstrating a lack of aggregation. It is believed that the increased amphiphilicity caused by the alkyl chain helps to drive the aggregation due to the hydrophobic effect.[7-8] A summary of cac values is shown in Table 4.1.

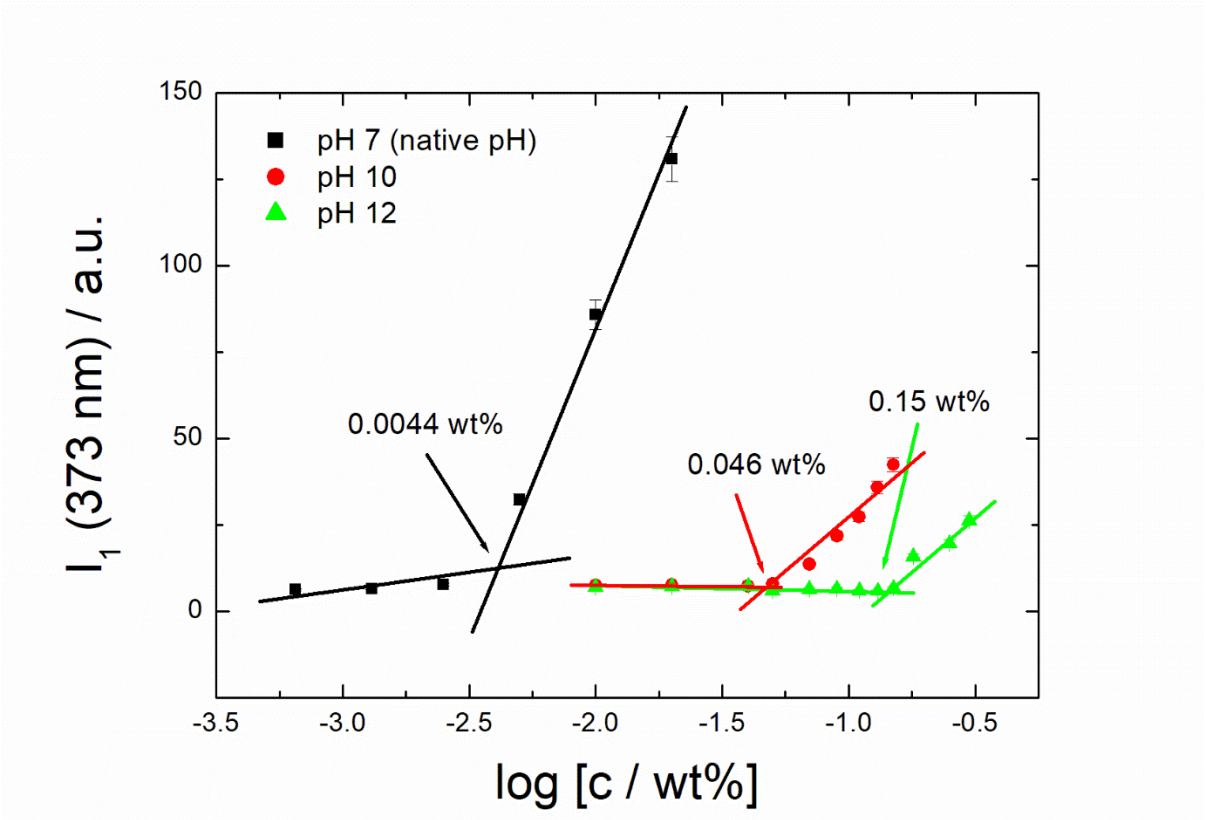

Figure 4.2. Fluorescence using pyrene to determine the critical aggregation concentration (cac) of C_{16}EELNRYY in the pH range 7-12. The point of intersection defines the cac. I_1= the intensity value at 373 nm.

Table 4.1. Summary of cac values (wt %) of C_{16}EELNRYY in the pH range 7-12.

	pH7 (wt%)	**pH10 (native pH) (wt%)**	**pH12 (wt%)**
C_{16}EELNRYY	0.0034	0.046	0.15

Circular dichroism spectroscopy was used to examine the secondary structure of the native and lipidated peptides at pH 9 and 20 °C. At pH 9 and above, both peptides were clear in solution, but below this pH, the lipidated peptide formed a precipitate. The native peptide appeared to have a disordered secondary structure with a minimum at

195 nm, whilst the lipidated truncated fragment exhibited a spectrum characteristic of a β-sheet structure with a minimum at around 218 nm, and positive ellipticity at 195nm (Figure 4.3). Temperature ramp experiments were also carried out for C_{16}EELNRYY from 20-70 ^{o}C, and the results show that the β-sheet structure is retained throughout this temperature range (Figure 4.4). A further CD experiment was performed to study the pH stability of the lipidated peptide in the pH range 7 (native pH) to pH 12. At high pH, tyrosine becomes charged tyrosinate, the conjugate phenolate base of tyrosine,[9] and the resulting CD spectra shows a significantly reduced molar ellipticity, that is only partially reversible upon returning the pH back to 7. This indicates that the peptide undergoes some degradation in highly alkaline conditions.

At pH 12, the peptide carries a highly negative charge of -6, calculated using innovagen software; [10] therefore charge repulsion was expected to interrupt secondary structure. The results in Figure 4.5 confirm this, and upon pH change from pH 7 to pH 12, there is a transition in secondary structure from β-sheet to disordered. Lowering the pH back down to 7 indicates only partial reversibility back to β-sheet, with molar ellipticity values at the 216 nm minimum, much less negative than before the pH change.

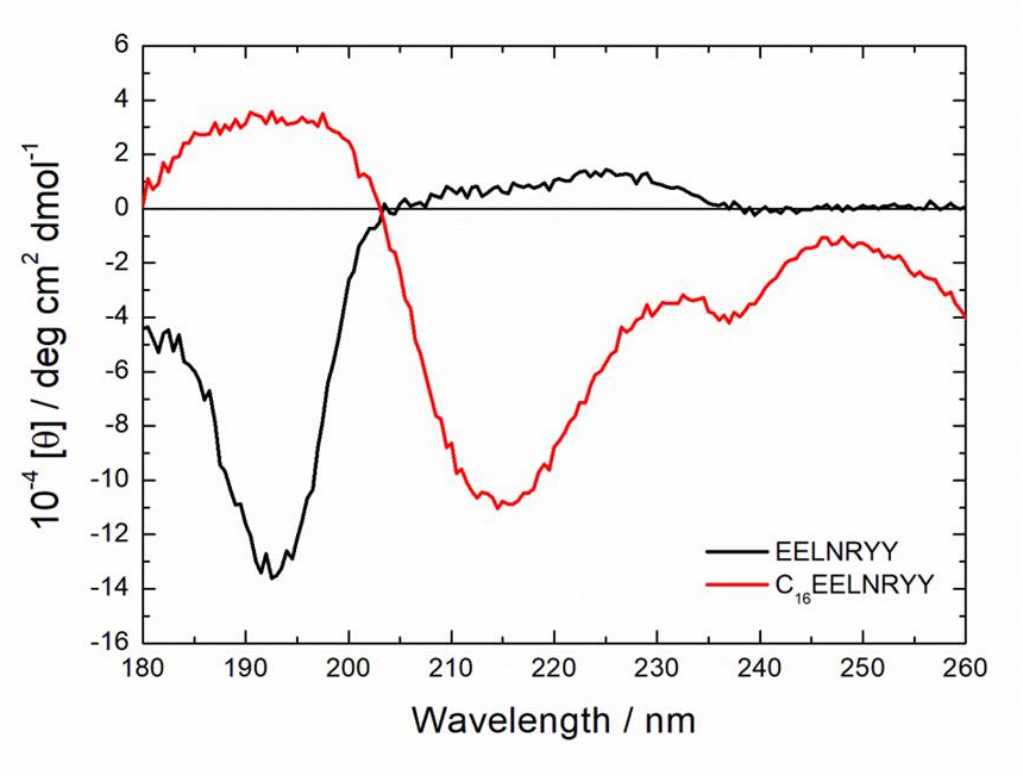

Figure 4.3. CD spectra of C_{16}EELNRYY and EELNRYY at 1 wt%, 20 °C and pH 9.

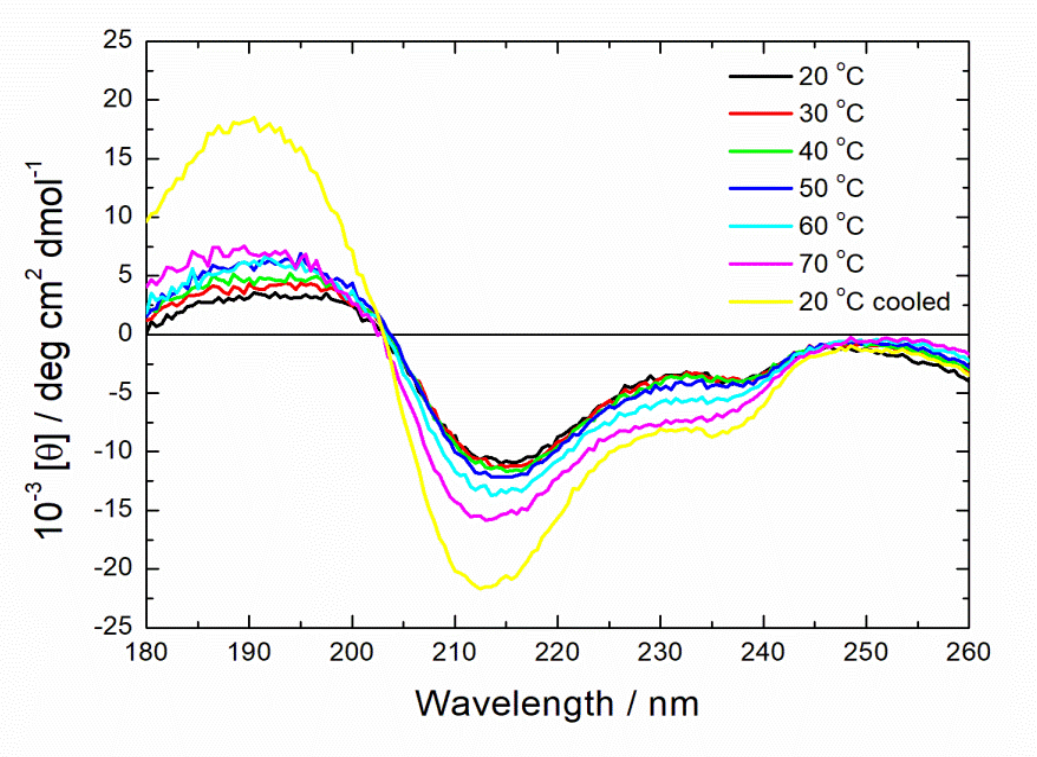

Figure 4.4. CD spectra of C_{16}EELNRYY at 1 wt%, from 20 -70 °C at pH 9.

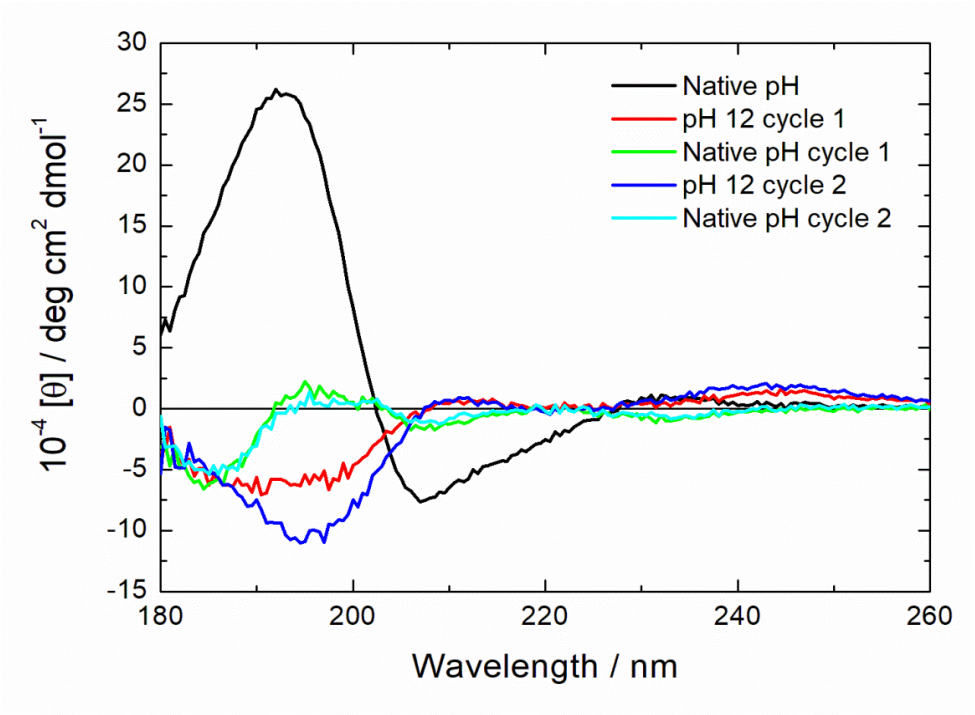

Figure 4.5. CD spectra of C_{16}EELNRYY to show secondary structure reversibility after two pH switch cycles from native pH to pH 12 at 20 °C.

Cryo-TEM and SAXS were used to further explore the self-assembly of the truncated peptide fragments. Cryo-TEM images of C_{16}EELNRYY revealed fibers at native pH (pH 7), clusters of micelles at pH 10, and nanosheets at pH 12 (Figure 4.6). As expected, no defined structures were observed for EELNRYY since it does not have a cac, and representative images are shown in Figure 4.7. SAXS was used to compliment cryo- TEM and scattering profiles of both peptides are shown in Figure 4.8. C $_{16}$EELNRYY data was fitted to a long cylindrical shell form factor at pH 7 (native pH), and a spherical shell form factor at pH 10, representative of fibers and micelles respectively. Data at pH 12 was fitted to a combination of a bilayer Gaussian and generalized Gaussian coil form factor (10:90 % ratio respectively). This was due to cryo-TEM images revealing the presence of

nanosheets, but the SAXS intensity profile indicating a mixture of monomers and nanosheets from the scattering shape at low q being similar to that of a monomer. The native peptide, EELNRYY was fitted to a generalized Gaussian coil form factor, to show monomers. There is a significant structure factor peak at q = 0.05 $Å^{-1}$ for C_{16}EELNRYY at pH 10, showing interactions between the micelles, consistent with cluster formation. Fitted parameters are shown in Tables 4.2-4.6.

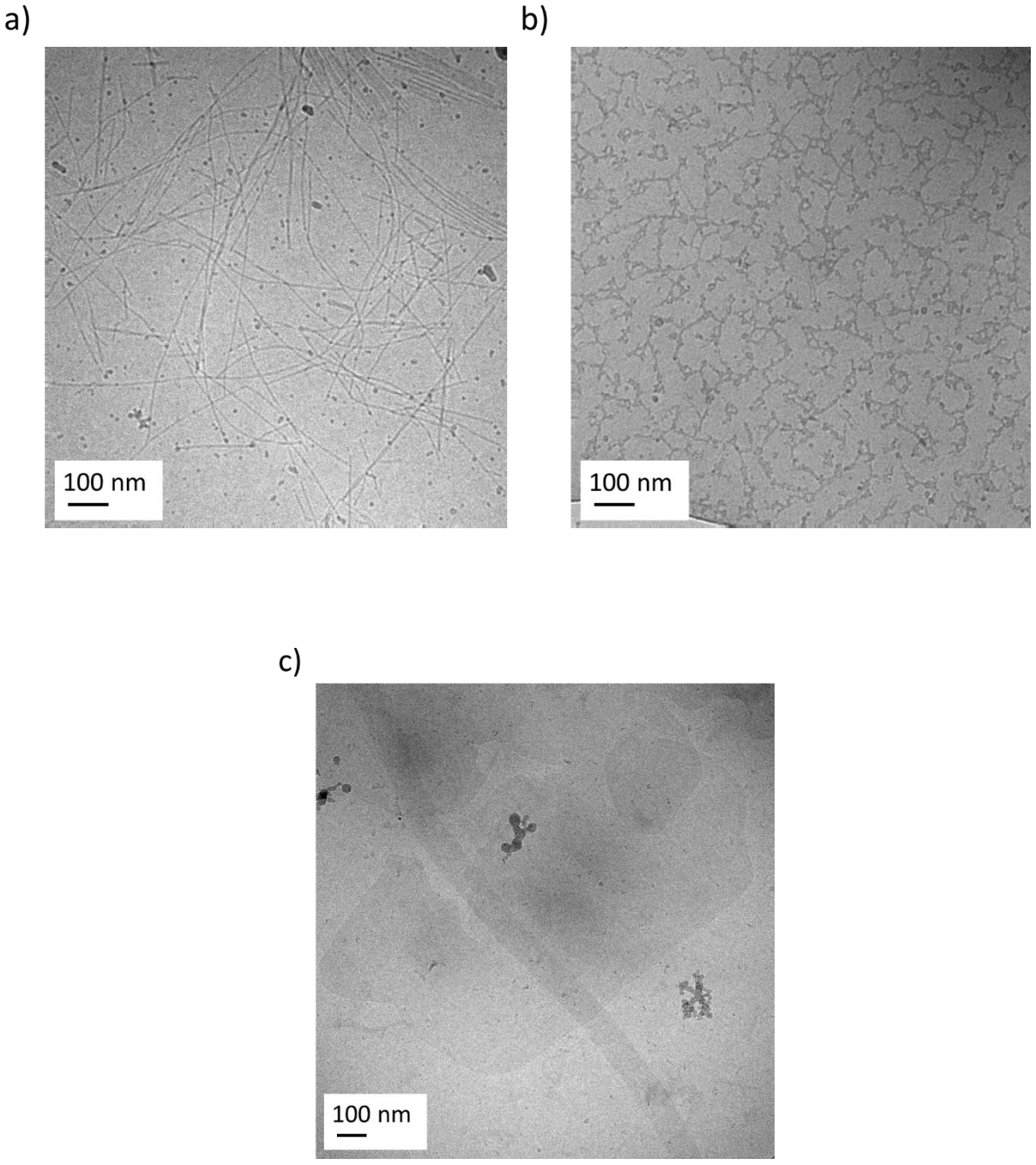

Figure 4.6. cryo-TEM images of C_{16}EELNRYY at 1 wt% in H_2O. a) native pH (pH 7) showing fibers, b) pH 10 showing clusters of micelles, c) pH 12 showing nanosheets.

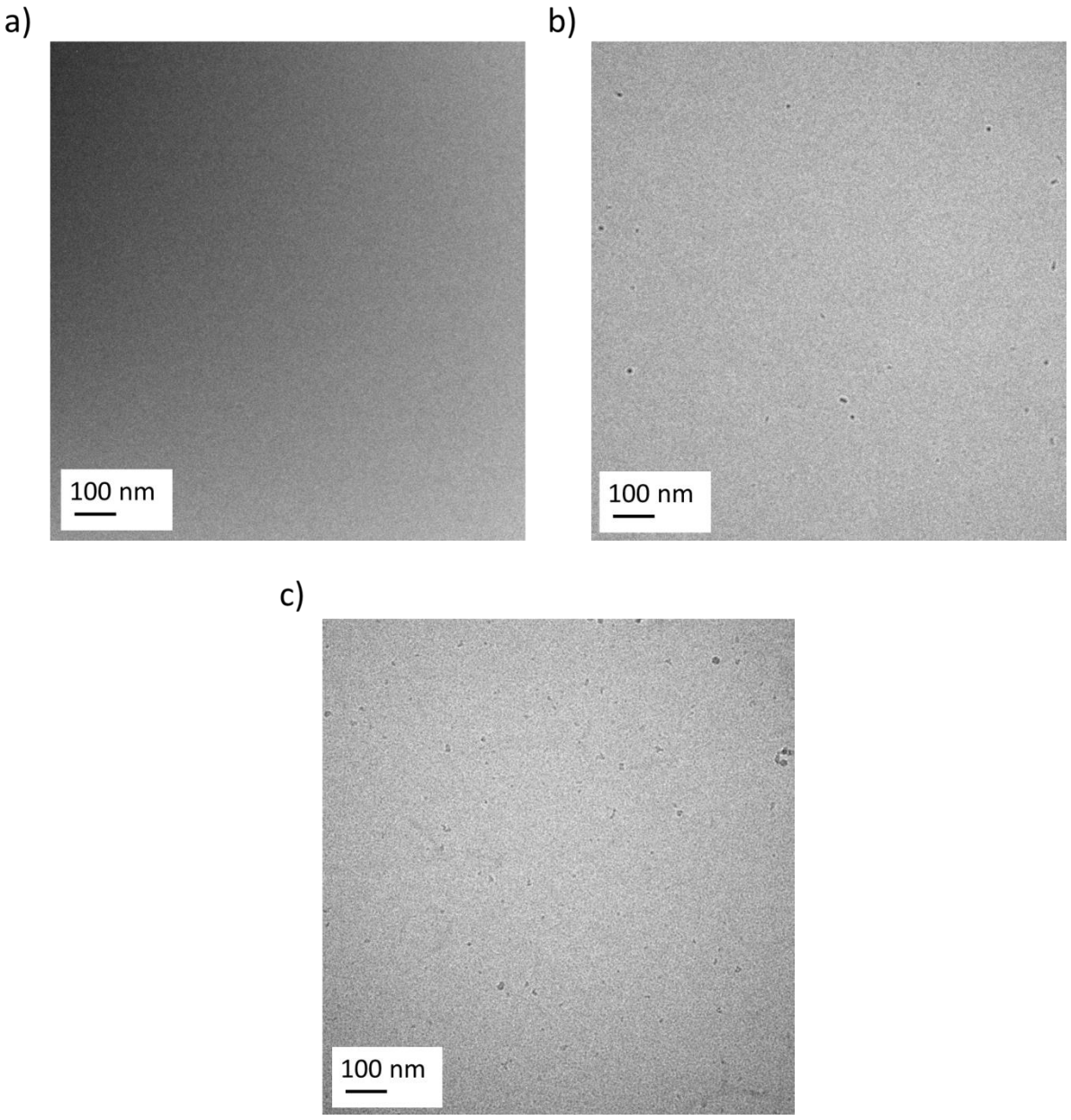

Figure 4.7. Cryo-TEM images of EELNRYY at 1 wt% in H_2O. a) native pH (pH 3), b) pH 10, c) pH 12. There is a lack of aggregation throughout the pH range studied.

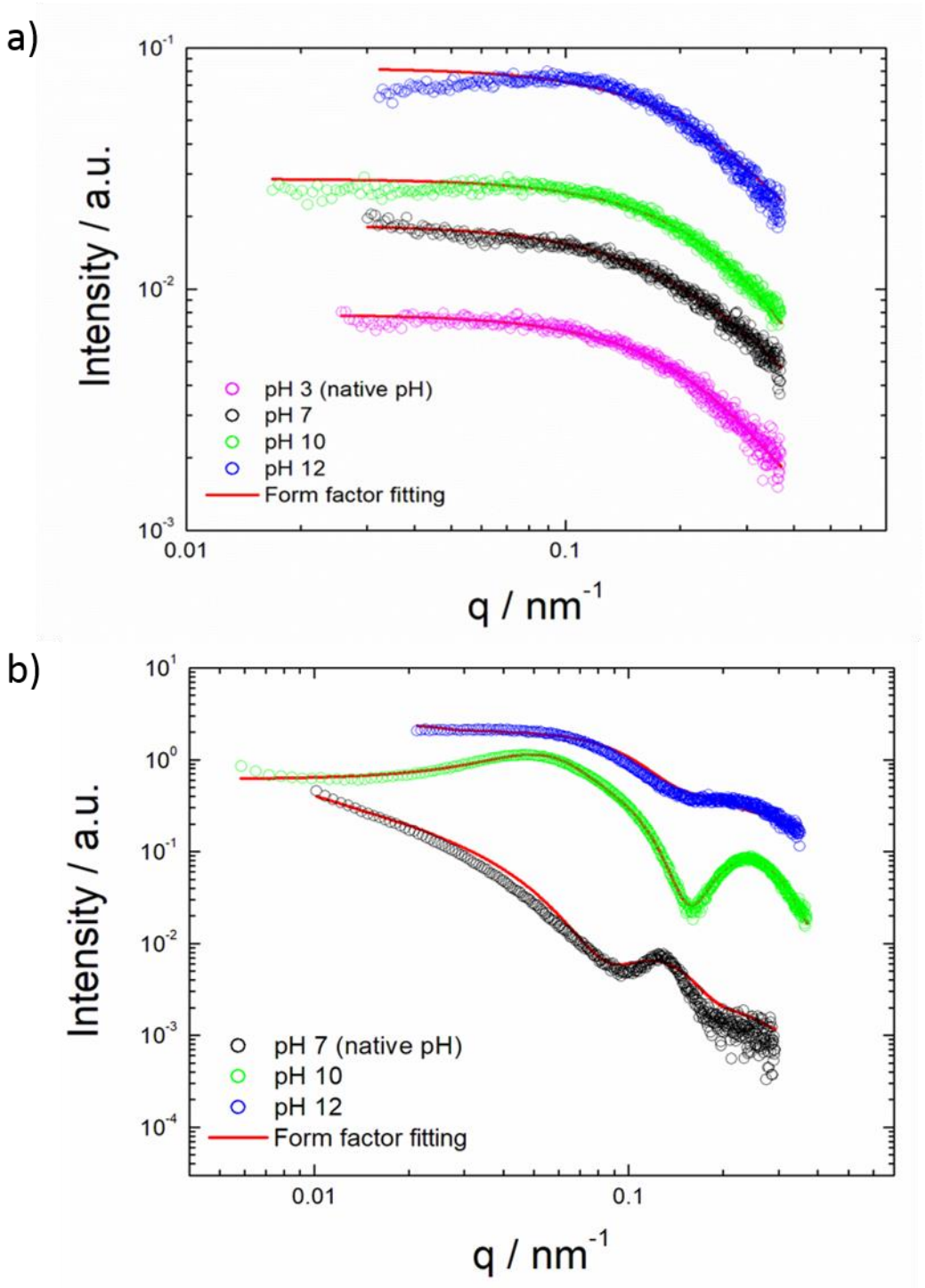

Figure 4.8. SAXS intensity profiles and form factor fittings of a) EELNRYY in the pH range 3-12. Data was fitted to a generalized Gaussian coil form factor fitting representative of monomers. b) C_{16}EELNRYY in the pH range 7-12. Data was fitted to a long cylindrical shell form factor at pH 7, a spherical shell at pH 10, and a combination of generalized Gaussian coil and bilayer Gaussian at pH 12.

Table 4.2. SAXS form factor parameters of EELNRYY (1 wt%) in the pH range 3-12 fit to a generalized Gaussian coil form factor model using SASfit. Key: BG = background, N= scaling factor, Rg = radius of gyration, v = Flory exponent, I0 = forward scattering.

Sample	BG	N/arb. units	Rg / nm	v	I0
EELNRYY pH3 (native pH)	$5x10^{-4}$	0.988	7.17	0.316	$7.4x10^{-3}$
EELNRYY pH7	$-1.8x10^{-3}$	1.27	6.98	0.877	$8.6x10^{-3}$
EELNRYY pH10	$1x10^{-4}$	0.643	6.32	0.327	$8.8x10^{-3}$
EELNRYY pH12	$1.4x10^{-3}$	1.54	7.00	0.181	$4.5x10^{-3}$

Table 4.3. SAXS form factor parameters of C_{16}EELNRYY (1 wt%) at pH 7 fit to a long cylindrical shell model using SASfit. Key: BG = background, N = scaling factor, σ = Gaussian width, R = inner radius, DR =shell thickness, L = length of cylinder, η_{core} = scattering contrast of core, η_{shell}= scattering contrast of shell, η_{solv}= scattering contrast of solvent.

Sample	BG	N/arb. units	σ/ nm	R/ nm	DR/ nm	L/ nm	η_{core}	η_{shell}	η_{solv}
C_{16}EELNRYY pH 7	$2.22x10^{-4}$	$2.11x10^{-8}$	5.46	24.8	0.65	500	$1.50x10^{-2}$	0.15	$1.60x10^{-2}$

Table 4.4. SAXS form factor parameters of C_{16}EELNRYY (1 wt%) at pH 10 fit to a spherical shell form factor model using SASfit. Key: BG = background, N= scaling factor, σ = Gaussian width, R_1= inner radius, R_2= outer radius, μ = scattering contrast of inner core, η = scattering contrast of shell.

Sample	BG	N/arb. units	σ/nm	R_1 / nm	R_2 / nm	μ	η core
C_{16}EELNRYY pH10	2.75×10^{-4}	1.00	5.22	16.77	9.83	-1.53	1.05×10^{-5}

Table 4.5. SAXS fitting parameters of C_{16}EELNRYY (1 wt%) at pH 12 fit to a bilayer Gaussian form factor (10%). BG = background, N = scaling factor, σ = Gaussian width, t = bilayer thickness, σ_{out} = Scattering density of outer Gaussians, b_{out} = width of outer Gaussians, σ_{core}= scattering density of inner Gaussian, b_{core}= width of inner Gaussians D = diameter of disc (fixed parameter).

Sample	BG	N / arb. units	σ / nm	t / nm	σ_{out}	b_{out}	σ_{core}	b_{core}	D / nm
C_{16}EELNRYY pH12	9.34×10^{-4}	1.19×10^{-8}	6.84	62.7	0.59	1.36×10^{-2}	13.63	-1.5×10^{-3}	500

Table 4.6. SAXS form factor parameters of C $_{16}$EELNRYY (1 wt%) at pH 12 fit to a generalized Gaussian coil form factor model using SASfit (90 %). Key: BG = background, N= scaling factor, Rg = radius of gyration, v = Flory exponent, I0= forward scattering.

Sample	**BG**	**N / arb. units**	**Rg / nm**	**v**	**I0**
C_{16}EELNRYY pH12	9.34×10^{-4}	4.83×10^{-2}	19.28	0.68	0.342

The possibility of dityrosine formation in alkaline conditions was investigated using fluorescence spectroscopy, at pH 12. Dityrosine is easily recognised by an intense fluorescence peak at 400 nm, representative of its singly ionized form, by excitation at 315 nm in alkaline conditions.[11-12] The emission and excitation spectra of C_{16}EELNRYY are shown in Figure 4.9. At pH 12, the emission spectrum shows a peak close to 400 nm, suggesting dityrosine formation, and this is not as prominent at native pH. This is because at high pH, the phenol hydroxyl group becomes deprotonated to form phenolate ions. The excitation spectrum also agrees with dityrosine formation due to a red shift from around 300 nm, to 320 nm.[13] Results for the unlipidated peptide also show dityrosine formation (Figure 4.10).

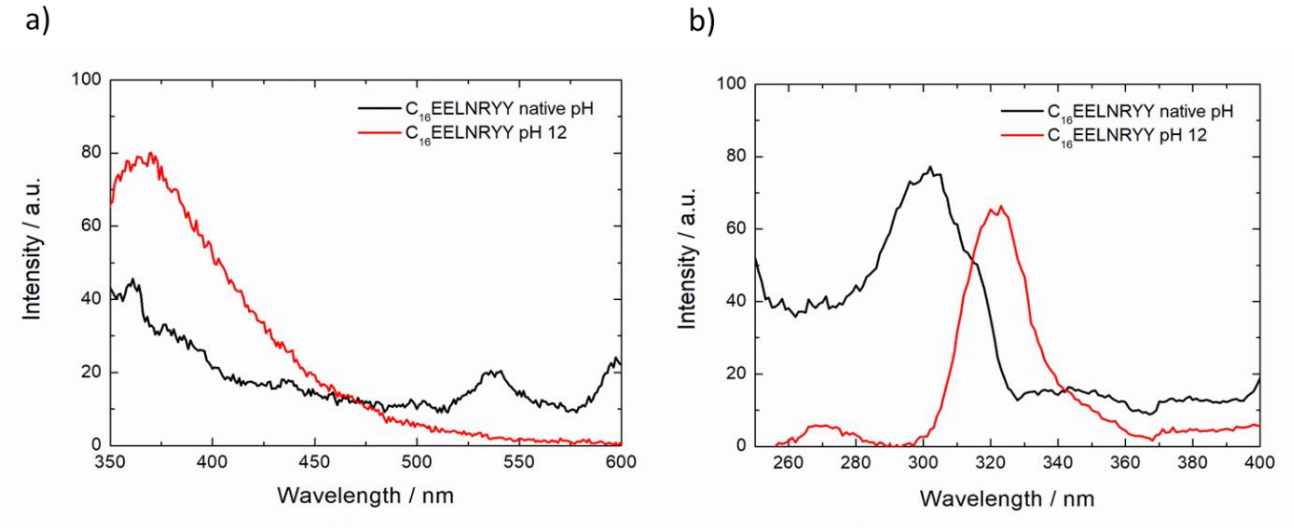

Figure 4.9. Fluorescence of C_{16}EELNRYY at pH 7 (native pH in water) and pH 12 to study dityrosine formation. a) Emission spectrum at λ_{ex}= 315 nm. b) Excitation spectrum at λ_{em}= 410 nm.

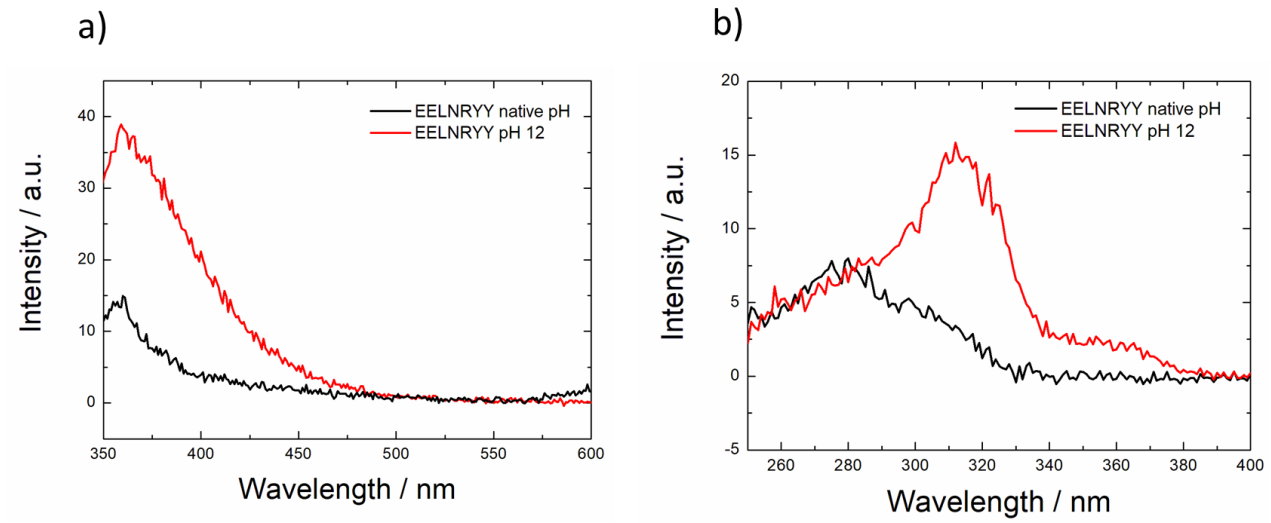

Figure 4.10. Fluorescence of EELNRYY at pH 2 (native pH in water) and pH 12 to study dityrosine formation. a) Emission spectrum at λ_{ex} = 315 nm. b) Excitation spectrum at λ_{em} = 410 nm.

4.2.1 Hydrogel Studies

Peptide hydrogels may be useful for many applications such as slow drug release delivery systems, regenerative medicine, the topical application of therapeutic peptides, or encapsulated drugs.[14-17] The use of short peptide sequences provides this, in addition to lowering cost as previously mentioned. Hydrogel formation by lapidated peptides is rather uncommon, and few studies have been reported so far. As mentioned in chapter 2, those that have been reported have been based on β-sheet nanofiber forming lipidated peptides that gelated via non-covalent intermolecular cross-linking.[18-20]

Since C_{16}EELNRYY was found to adopt a β-sheet structure, and contained two aromatic tyrosine residues, it was of interest to investigate its gelation properties. Increasing the concentration to 1 wt% and above allowed for the formation of a hydrogel for the lipidated peptide, with the gel forming at the peptides native pH in ultrapure water (pH 7) (Figure 4.11). The theoretical isoelectric point calculated using Innovagen software, was 4.15, with the net charge being -1 at pH 7.[10] At pH 7, the electrostatic charges are easily overcome, allowing the hydrophobic interactions, and π-π stacking of the tyrosine residues to drive gelation. It is however important to remember that the pKa values in peptides can shift upon aggregation, meaning that the exact charge on amino acid residues is very hard to quantify fully.[21-22] Gelation was not observed for the native peptide. It was thought that the incorporation of a hydrophobic alkyl chain to the peptide influenced the β-sheet structure and enhanced fibril formation, by allowing minimal contact between the water and the hydrophobic alkyl chain.[23] Therefore a combination of increased hydrophobicity, and π-π stacking of the tyrosine motifs was suggested to be the mechanism behind gelation.

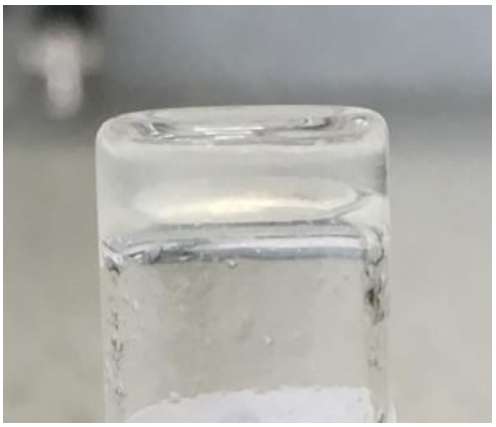

Figure 4.11. Gel of C_{16}EELNRYY at 1 wt% shown by the inverted vial method.

CD and fiber X-ray diffraction (XRD) were used to study conformation, along with SAXS and TEM to probe the morphology. Rheology was then used to determine the viscoelastic properties of the gel (Figure 4.12). The strain sweep shows linear viscoelastic behaviour up to around 1 % oscillation strain, and the frequency sweep at a fixed strain of 0.6 % shows that the moduli exhibit only a weak dependence on frequency. Furthermore, G' > G", and the magnitude of G' is significantly high compared to a fluid, consistent with a solid like structure (Figure 4.12b). Temperature ramp experiments were also measured and results showed that the gel was stable throughout the temperature range studied (20-40 ^{o} C) with both moduli not significantly changing (Figure 4.13). Further stability studies were carried out on the lipidated peptide hydrogel to investigate its reversibility. Firstly, the pH was decreased to pH 2.95 to break up the gel into insoluble peptide clumps and water. The pH was then raised to a value close to the peptide's native pH (pH 6.95). Results found that the gel re-formed within a few hours. Next, the gel was heated to 55 ^{o}C, where the gel transitioned into a viscous liquid.

Upon cooling the gel re-formed. These results indicate full reversibility of the hydrogel to changes in pH and temperature.

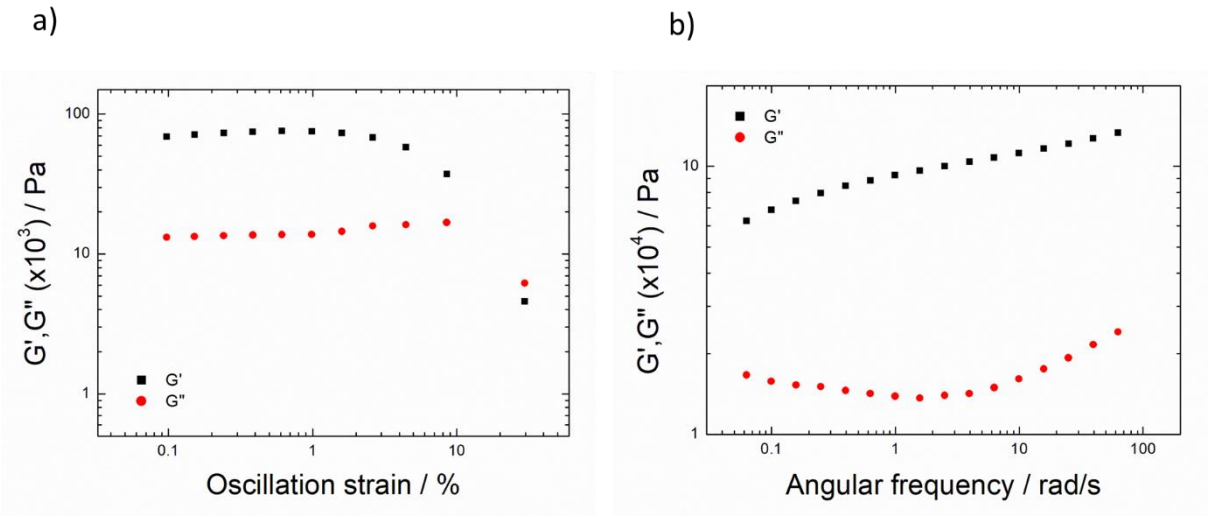

Figure 4.12. Dependence of G' and G" at 20 °C and 1 wt% on the: a) oscillatory strain, and b) angular frequency, with the oscillation strain fixed to 0.6 % which lies within the linear regime.

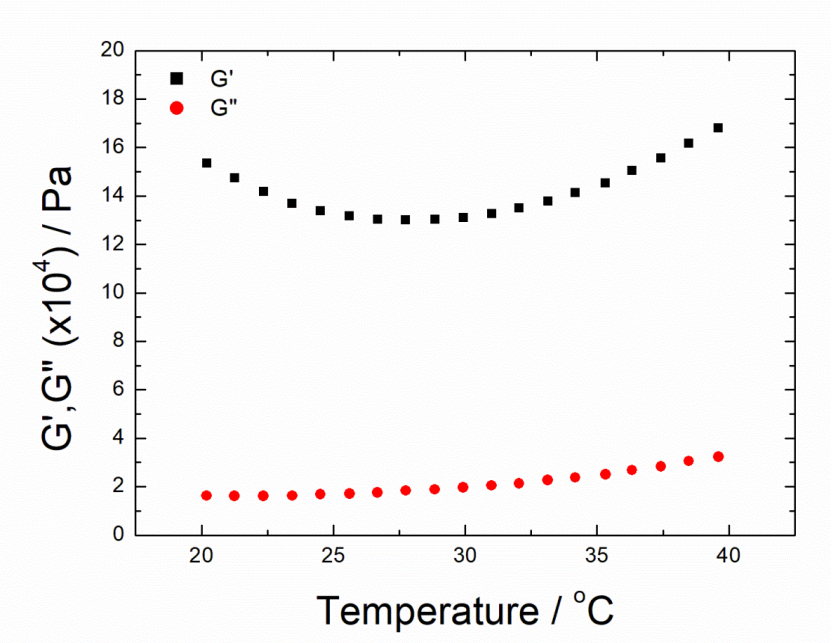

Figure 4.13. Temperature ramp of the dynamic shear moduli of C_{16}EELNRYY from 20-40 °C, showing stability of G' with temperature.

CD spectra from gels of the lipidated peptide fragment at pH 7, from 20-70 ^{o}C are shown in Figure 4.14a, and the data shows a β-sheet like spectrum with a minimum close to 210 nm over the whole temperature range. Fiber XRD intensity profiles are shown in Figure 4.14b and the results indicate a β-sheet structure for the lipidated peptide, with the d-spacings of 4.68 Å being associated with the spacing between two β-strands in the same β-sheet.[25] XRD data of the native peptide also has d-spacings of 4.68 Å, suggesting a change in conformation from disordered to a β-sheet structure upon drying. TEM images of the peptide gel show a network of entangled fibers (Figure 4.14c). This compares to the cryo-TEM images at native pH, where fibers were also observed. However, there was a substantial amount of time between when the sample was prepared, and when cryo-TEM was carried out, and it was thought that the peptide had already gelled by the time the images were produced. As a result it is believed that both cryo-TEM and TEM images are of the lipidated hydrogel. The SAXS intensity profile of the gel is shown in Figure 4.14d and data was fitted to a long cylindrical shell form factor, typically used for fibrils (Table 4.6).

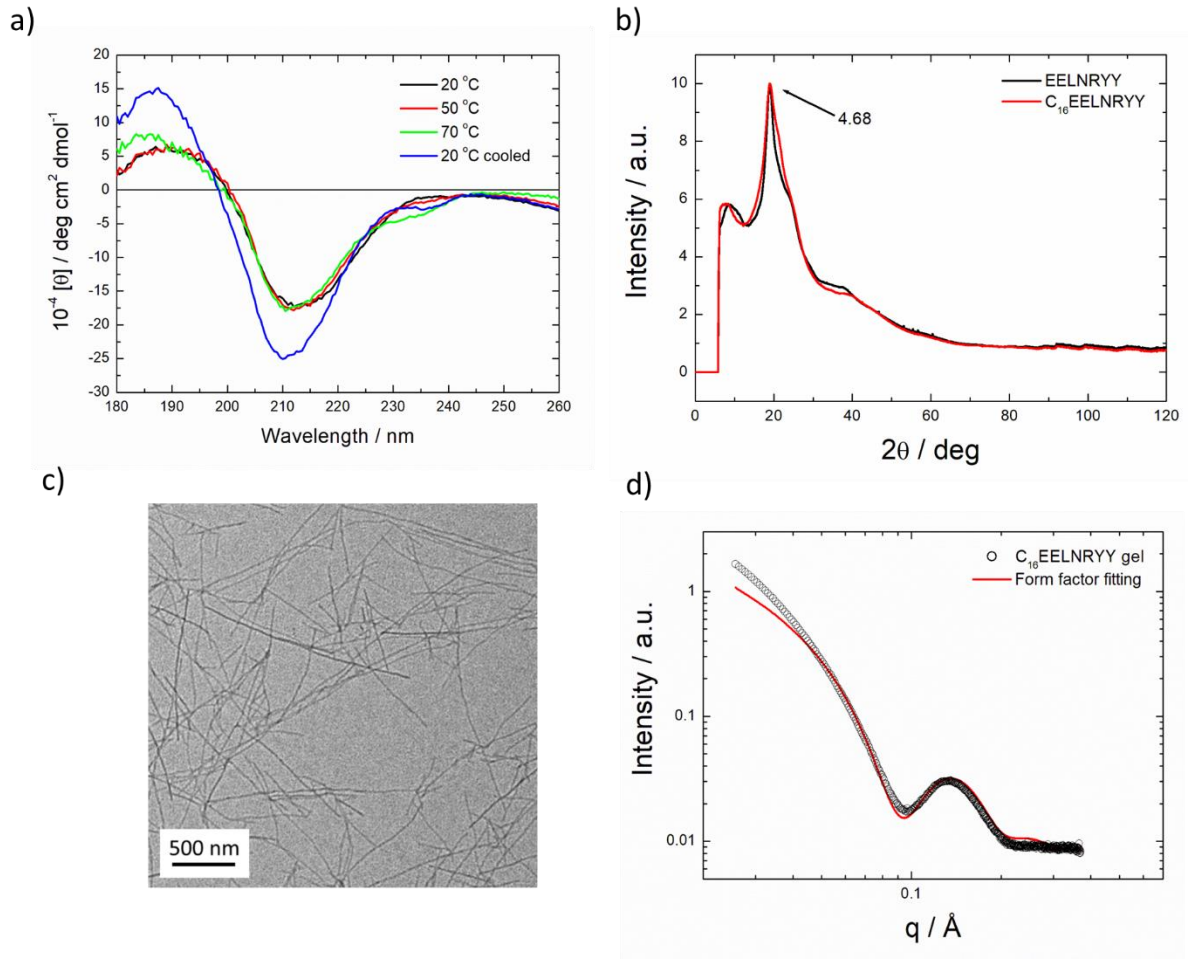

Figure 4.14. a) Gel CD of C_{16}EELNRYY at 1 wt% at pH 7 from 20-70 ^{o}C. b) Fibre X-ray diffraction intensity profile of EELNRYY and C_{16}EELNRYY at native pH, with Bragg spacing of 4.68 Å. c) TEM images of C_{16}EELNRYY gel at 1 wt% showing a network of fibers at native pH. d) SAXS data of C_{16}EELNRYY gel at 1 wt% fit to a long cylindrical shell form factor.

Table 4.6. SAXS form factor parameters of C_{16}EELNRYY gel (1 wt% and pH 7) fit to a long cylindrical shell form factor model using SASfit. Key: BG = background, N = scaling factor, σ = Gaussian width, R = inner radius, DR =shell thickness, L = length of cylinder, η_{core} = scattering contrast of core, η_{shell}= scattering contrast of shell, η_{solv}= scattering contrast of solvent.

Sample	BG	N / arb. units	σ/ nm	R/ nm	DR/ nm	L/ nm	η_{core}	η_{shell}	η_{solv}
C_{16}EELNRYY gel pH7	8.4×10^{-3}	2.72×10^{-9}	3.25	17.43	14.8	500	1.23×10^{-3}	1.27×10^{-3}	1.23×10^{-3}

4.2.2 Cytocompatibility Studies

4.2.3 Assay Development

Cells have four distinct growth phases: lag phase, exponential phase, stationary phase, and death phase. During the lag phase cells adjust to their environment and start to increase in size, before entering the exponential phase where they continue to grow and divide but at a constant pace. Following this, the cells enter the stationary phase where their growth plateaus and cell death and proliferation become equal. Finally, the death phase occurs where the rate of cell death is higher than cell proliferation and cell viability declines at an exponential rate.

A growth curve experiment was carried out prior to the cell studies using peptide concentrations ranging from 5×10^3 to 8×10^4 cells per mL, to ensure that cells were within the exponential growth phase in the experiment, and thus determine a suitable cell density value. The density chosen was 4×10^4 cells per mL since the cells were still

in the growth phase at this concentration, making it a viable value (Figure 4.15). However due to the aggressive nature of the cell line, when MTT (3-(4,5-dimethylthiazol-2-yl)-2,5-diphenyltetrazolium bromide) was added, it metabolized to formazan crystals of an extremely high density, giving rise to crystal de-attachment from the bottom of the 96-well plate. This resulted in underestimation of viable cell numbers. As a result, the experiments were repeated with a lower cell density of 1 x 10^4 (still in the growth phase) by C.J.C Edwards-Gayle, University of Reading. Results followed a similar trend, and the lipidated peptide was significantly more cytotoxic than the native peptide. Cytocompatibility studies on the full PYY_{3-36} sequence using Caco-2 cells (another colon cancer cell line) have been reported, and PYY_{3-36} was not found to exert any cytotoxic effects.[26] As a result, the studies presented here of the truncated PYY_{3-36} fragment, provide a good judgment of how lipidated analogues of the full peptide sequence would behave under the same conditions.

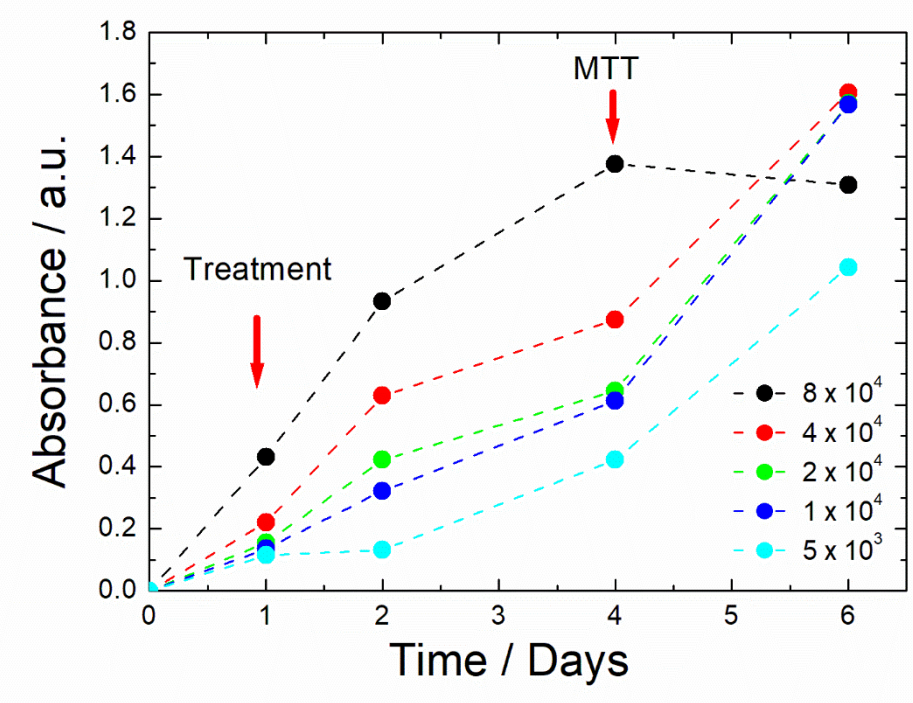

Figure 4.15. Growth curve data using HCT-116 cells over a 6-day period, to calculate a suitable cell density for cytocompatibility studies.

4.2.4 MTT Assay on a HCT-116 Cell Line

Cytocompatibility studies of C_{16}EELNRYY, and EELNRYY, were performed using an MTT ((3-(4,5-Dimethylthiazol-2-yl)-2,5-diphenyltetrazolium bromide) assay on human colorectal tumour cells (HCT-116 cell line), to determine cell viability (Figure 4.16-4.17). This cell line was used with it being a gut cell line, and therefore of interest to EELNRYY and C_{16}EELNRYY since they are gut derived peptide fragments. The IC_{50} (half maximal inhibitory concentration) was found to be 0.061 wt% for C_{16}EELNRYY. Above this concentration there is a significant decrease in cell proliferation, with only around 20 % of cells still viable. An IC_{50} value was not obtained for native EELNRYY due to more than 50 % of the cells being viable throughout the concentration range studied. These results are interesting and indicate that the lipidated peptide is significantly more cytotoxic than the native peptide at concentrations above the cac, suggesting that peptide aggregation is causing the peptide to become cytotoxic. Further studies to investigate this further are required to gain a more in-depth knowledge. It would also be useful to carry out work on a non-cancer based gut cell line to compare cytotoxicity between the two.

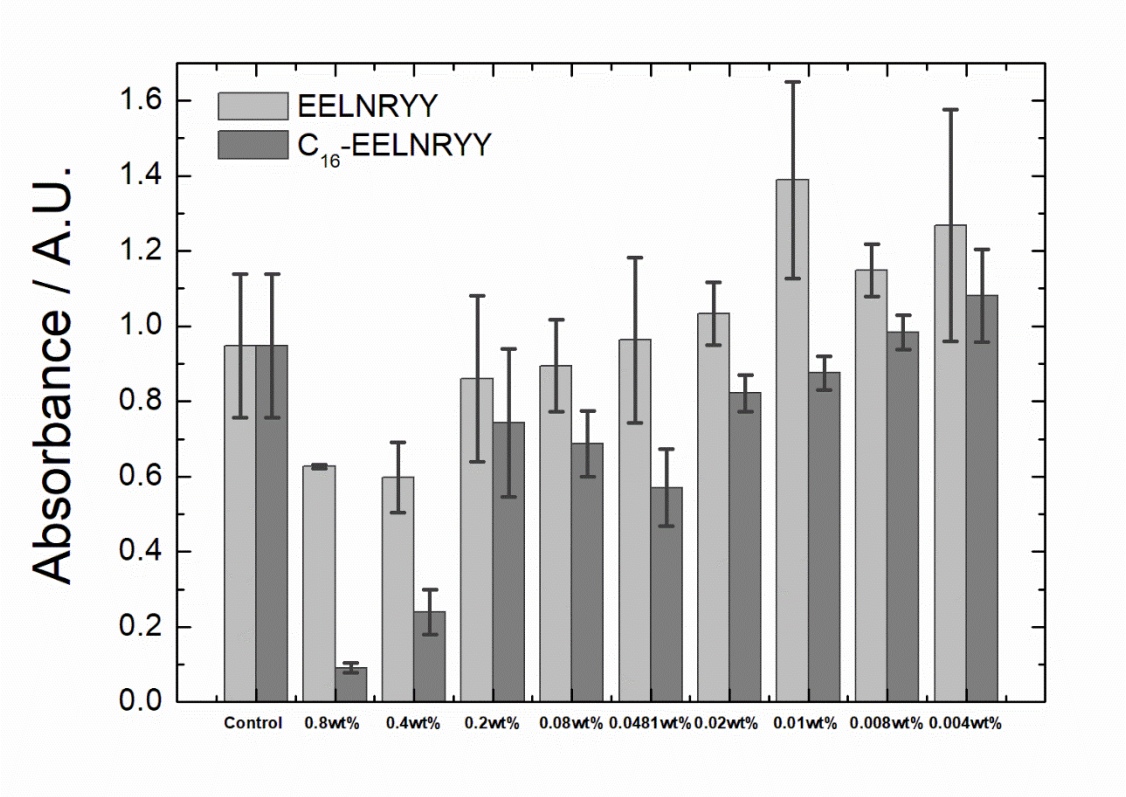

Figure 4.16. Absorbance as a function of peptide concentration of EELNRYY and C_{16}EELNRYY to show cell viability.

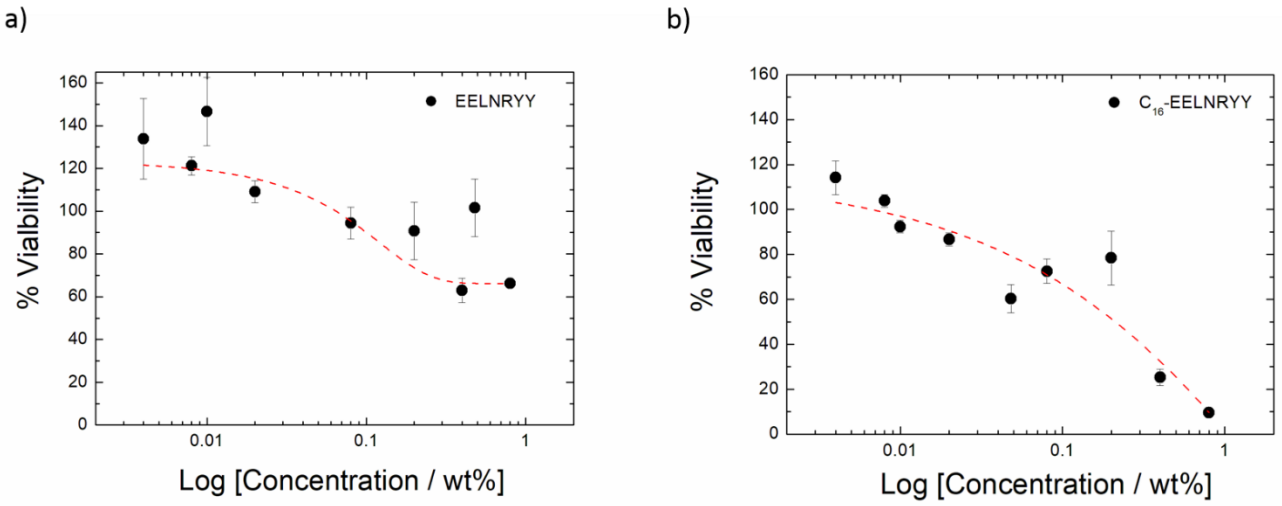

Figure 4.17. % cell viability of HCT-116 cells after treatment with a) EELNRYY, b) C_{16}EELNRYY.

4.3 Conclusion

In this chapter the self-assembly and cytotoxicity of an N-terminal lipidated peptide fragment of the gastrointestinal peptide hormone PYY_{3-36} has been examined, and compared to the unlipidated fragment. Fluorescence studies using pyrene successfully determined the cac of C_{16}EELNRYY, however no cac was obtained for EELNRYY, suggesting that the increased amphiphilic nature of the lipidated peptide favoured aggregation. Circular dichroism spectroscopy showed distinct differences between the lipidated peptide and the native peptide, with the lipidated peptide having a β-sheet secondary structure and the native peptide having a disordered structure. SAXS and cryo-TEM further enhanced the differences between the two peptides, with cryo-TEM and SAXS of the lipidated peptide showing a range of aggregated structures from micelle clusters, to fibrils, to nanosheets depending on pH. No distinct aggregated structures were observed for the native peptide. Unexpectedly, the lipidated peptide was found to form a hydrogel at native pH (pH 7) and at 1 wt %. The charge on the peptide at this pH was calculated to be -1 using web based software.[10] The mechanism behind gelation was attributed to π- π stacking of the tyrosine residues, along with the lipid chain favouring a β-sheet structure, allowing for the formation of cross-linked fibrils, leading to gelation. Rheological studies found G' to be substantially higher than a typical fluid, suggesting a hard gel structure.

Cytotocompatibility studies using the HCT-116 cell line found the lipidated peptide to be cytotoxic at concentrations above the cac. The native peptide was not found to be significantly toxic, with more than 50 % of the cells still viable throughout the

concentration range studied. As a result, it is thought that aggregation leads to cytotoxicity.

4.4 Materials and Methods

Materials. Palmitoyl-EELNRYY (ammonium acetate salt) was synthesised by Peptide Synthetics, Fareham. UK. The molecular mass by API-ES was 1224.451 g mol^{-1} (expected 1223.68 g mol^{-1}), with a purity of 96.4 % determined by HPLC.

EELNRYY (TFA salt) was synthesised by Peptide Synthetics, Fareham. UK. The molecular mass by API-ES was 986.031 g mol-1(expected 985.45g mol^{-1}), with a purity of 95.3 % determined by HPLC.

Fluorescence Spectroscopy. The critical aggregation concentration experiments were determined using a Varian Cary Eclipse fluorescence spectrometer (Varian IEEE-488, Australia) with samples in 4 mm inner quartz cuvettes. Pyrene was used as the fluorescent probe, and assays were performed using 1.0 x 10^{-2} to 0.3 wt% peptide, in 2.167 x 10^{-5} wt% pyrene solution. The samples were excited at λ_{ex} = 339 nm, and the fluorescence emission was measured for λ = 360−500 nm. Dityrosine formation was investigated at native pH (pH 7) and pH 12. Fluorescence experiments were measured for water and 0.1 wt% peptide solutions. Samples were measured in a 1.0 cm path-length quartz cuvette, and the slit width was 5 nm. Emission spectra were recorded at λ_{ex} = 315 nm from 340 to 600 nm, and excitation spectra were recorded at λ_{em} = 410 nm, from 250-410 nm. Five measurements were taken for each, and the background was subtracted.

Circular Dichroism (CD). CD spectra were recorded using a Chirascan spectropolarimeter (Applied Photophysics, UK). Spectra are presented with absorbance A < 2, with a 0.5 nm step, 1 nm bandwidth, 1 s collection time per step, and 3 repeats. The CD signal from the background (water) was subtracted from the CD signal of the sample solution. Ellipticity is reported as the mean residue ellipticity ([θ], in deg cm^2 / dmol) and calculated as:

$[\theta] = [\theta]_{obs} MRW/10cl$

Where [θ] obs is the ellipticity measured in millidegrees, MRW is the mean residue molecular weight of the peptide (molecular weight divided by the number of amino acid residues), c is the concentration of the sample in mg/mL, and l is the optical path length of the cell in centimeters.

Samples were measured using quartz plaques (0.1 mm spacing) with 1 wt% solution concentration in the pH range 9-10. CD spectra were measured using a temperature range of 20-70 ^{o} C with 10 ^{o} C increments. The sample was equilibrated at each temperature for 2 minutes before measurements were recorded.

Cryogenic Transmission Electron Microscopy (cryo-TEM). Imaging was carried out using a field emission cryo-electron microscope (JEOL JEM-3200FSC) operating at 200 kV. Images were taken using bright-field mode and zero loss energy filtering (omega type) with a slit width of 20 eV. Micrographs were recorded using a CCD camera (Gatan Ultrascan 4000, USA). The specimen temperature was maintained at -187 ^{o}C during the imaging. Vitrified specimens were prepared using an automated FEI Vitrobot device using Quantifoil 3.5/1 holey carbon copper grids, with a 3.5 µm hole size. Grids were cleaned using a Gatan Solarus 9500 plasma cleaner just prior to use and then transferred

into the environmental chamber of a FEI Vitrobot at room temperature and 100 % humidity. Following this, 3 µL of sample solution at 1 wt % concentration was applied on the grid, blotted once for 1 s, and then vitrified in a 1:1 mixture of liquid ethane and propane at −180°C. Grids with vitrified sample solutions were maintained in a liquid nitrogen atmosphere and then cryo-transferred into the microscope. 1 wt% samples in the pH range 7-12 were imaged.

Small Angle X-ray Scattering (SAXS). Solution SAXS measurements were carried out on the bioSAXS beamline B21 at Diamond, Harwell, UK. Peptide solutions (1 wt% in the pH range of 9-10) in water were loaded into PCR tubes in an automated sample changer. Data was collected using a 2 M detector and at a fixed camera length of 3.9 m with a wavelength λ = 1 Å. The wavenumber $q = 4\pi \sin\theta / \lambda$ scale was calibrated using silver behenate, where λ is the x-ray wavelength and 2θ is the scattering angle.

Rheology. Gel properties were investigated using an AR-2000 rheometer. Experiments were performed using a plate-and-plate geometry (plate radius = 20 cm; gap = 400 µm). The linear regime of the sample was first identified from the dependence of the storage (G') and loss (G") moduli on the oscillation strain at a fixed frequency of 1 Hz. The dependence of G' and G" on the angular frequency was then determined at a fixed oscillatory strain of 0.6 % within the linear regime.

Cytocompatibility studies using MTT assays. The cytotoxicity of C_{16}EELNRYY and ELELNRYY was examined. In vitro cell culture was carried out using the HCT-116 human colorectal tumour cell line. Cells were cultured in McCoys 5A modified medium with 10% fetal bovine serum (FBS), and 1% antibiotic-antimycotic (Thermoscientific, 100×). Cells were maintained in a humidified atmosphere of 5 % CO_2 at 37 ° C. Cell viability effects

were examined using the MTT 3-(4,5- dimethylthiazol-2-yl)-2,5- diphenyltetrazolium bromide) assay. The peptide was dissolved in complete medium. Cells were seeded into a 96-well plate at a seeding density of 4×10^4 cells/mL, and allowed to adhere for 24 h in 100 µL complete medium. After 24 h, a total volume of 100 µL of either complete medium and/or peptide solution was added, to give final peptide concentrations of 0.08, 0.04, 0.02, 0.008, 0.00481, 0.002, 0.001, 0.0008 or 0.0004 wt% peptide. Negative controls of peptide in complete medium with no cells were included. After 67 h of incubation, 20 µL of MTT (0.5 wt% in PBS) was added to each well plate and allowed to incubate for 5 h (total of 72 h incubation). After this, the solutions were removed from the wells and replaced with 100 µL DMSO per well in order to dissolve the formazan crystals. Plates were incubated for 30 min, and then analyzed using a UV microplate reader (λ = 570 nm). Results are reported [(treated cells − negative control)/(untreated cells)] × 100.38−40.